Transition-Metal Doped Bi_2Se_3 and Bi_2Te_3 Topological Insulator Thin Films

Liam J. Collins-McIntyre

Lincoln College

University of Oxford

A thesis submitted for the degree of

Doctor of Philosophy

Hilary 2015

For Emily

‘Great are the works of the Lord; They are studied by all who delight in them.’ - *Psalm 111:2*

Acknowledgements

There are many who have helped this work come to completion and to whom I am immensely grateful. First thanks must, of course, go to my supervisor Prof. Thorsten Hesjedal, who has steered this work through to its end point and whose input on this scientific work and the writing of this thesis are greatly appreciated. This work could also not have been completed without the help of my proof readers: my mother Peta, and wife Emily. All of science is a collaborative field and I have had the great pleasure over the course of my studies to work with many wonderful fellow students and researchers. I would like to thank Prof. Gerrit van der Laan and Dr. Adriana Figueroa for all their work supporting the XMCD and EXAFS measurements as part of this thesis. Without their contribution it would not have been possible to resolve so many of the questions surrounding the nature of magnetism in these materials. For their assistance with running and understanding the PNR data acquired, thanks go to the team from ISIS Neutron and Muon Source: Prof. Sean Langridge, Dr. Tim Charlton, Dr. Nina-Juliana Steinke, Dr. Christy Kinane and Dr. Diego Alba-Venero. Thanks go to the many beamline teams that have made it possible to acquire the synchrotron measurements presented in this thesis: from I10, Diamond: Dr. Paul Steadman, Dr. Alexey Dobrynin, Dr. Peter Bencock and Mr. Mark Sussmuth; from I06, Diamond: Prof. Sarnjeet Dhesi, Dr. Francesco Maccerozzi and Dr. Stuart Cavill; from I07, Diamond: Prof. Chris Nicklin, Dr. Jonathan Rawle, Dr. Pilar Ferrer and Dr. Matthew Forster; from ALS: Dr. Bo Zhou, Dr. Elke Arenholz and Dr. Padraic Shafer. Thanks to Prof. Yulin Chen for his constructive comments regarding the theory of TIs as well as input regarding the measurement and understanding of ARPES in these materials. The work on bulk Mn-doped crystals was performed in collaboration with Mr. Matt Watson and his supervisor Dr. Amalia Coldea and I am very grateful for their input to these experiments. Thanks go to Katie Charlesworth and Hiten Patel for their assistance in obtaining AFM and XRD data respectively.

Finally I must thank my esteemed colleagues in the Oxford MBE group: Alex Baker, Piet Schönherr and Shilei Zhang, as well as our adopted American, Sara Harrison of Stanford University. You've all always been there in support and provided all the banter one could ever hope for. Thanks for making my graduate studies as great as they have been!

Abstract

Topological insulators (TIs) are recently predicted, and much studied, new quantum materials. These materials are characterised by their unique surface electronic properties; namely, behaving as band insulators within their bulk, but with spin-momentum locked surface or edge states at their interface. These surface/edge crossing states are protected by the underlying time-reversal symmetry (TRS) of the bulk band structure, leading to a robust topological surface state (TSS) that is resistant to scattering from impurities which do not break TRS. Their surface band dispersion has a characteristic crossing at time reversal invariant momenta (TRIM) called a Dirac cone. It has been predicted that the introduction of a TRS breaking effect, through ferromagnetic order for instance, will open a band-gap in this Dirac cone. It can be seen that magnetic fields are not time reversal invariant by considering a solenoid. If time is reversed, the current will also reverse in the solenoid and so the magnetic field will also be reversed. So it can be seen that magnetic fields transform as odd under time reversal, the same will be true of internal magnetisation. By manipulating this gapped surface state a wide range of new physical phenomena are predicted, or in some cases, already experimentally observed. Of particular interest is the recently observed quantum anomalous Hall effect (QAHE) as well as, e.g., topological magneto-electric effect, surface Majorana Fermions and image magnetic monopoles. Building on these novel physical effects, it is hoped to open new pathways and device applications within the emerging fields of spintronics and quantum computation.

This thesis presents an investigation of the nature of magnetic doping of the chalcogenide TIs Bi_2Se_3 and Bi_2Te_3 using $3d$ transition-metal dopants (Mn and Cr). Samples were grown by molecular beam epitaxy (MBE), an ideal growth method for the creation of high-quality thin film TI samples with very low defect densities. The grown films were investigated using a range of complementary lab-based and synchrotron-based techniques to fully resolve their physical structure, as well as their magnetic and electronic properties. The ultimate aim being to form a ferromagnetic ground state in the insulating material, which may be expanded into device applications.

Samples of bulk Mn-doped Bi_2Te_3 are presented and it is shown that a ferromagnetic ground state is formed below a measured T_C of 9-13 K as determined by a range of experimental methodologies. These samples are found to have significant inhomogeneities within the crystal, a problem that is reduced in MBE-grown crystals. Mn-doped Bi_2Se_3 thin films were grown by MBE and their magnetic properties investigated by superconducting quantum interference device (SQUID) magnetometry and x-ray magnetic circular dichroism (XMCD). These reveal a saturation magnetisation of 5.1 μ_B/Mn and show the formation of short-range magnetic order at 2.5 K (from XMCD) with indication of a ferromagnetic ground state forming below 1.5 K.

Thin films of Cr-doped Bi_2Se_3 were grown by MBE, driven by the recent observation of the QAHE in Cr-doped $(Bi_{1-x}Sb_x)_2Te_3$. Investigation by SQUID shows a ferromagnetic ground state below 8.5 K with a saturation magnetisation of 2.1 μ_B/Cr. Polarised neutron reflectometry shows a uniform magnetisation profile with no indication of surface enhancement or of a magnetic dead layer. Further studies by extended x-ray absorption fine structure (EXAFS) and XMCD elucidate the electronic nature of the magnetic ground state of these materials. It is found that hybridisation between the Cr d and Se p orbitals leads to the Cr being divalent when doping on the Bi^{3+} site. This covalent character to the electronic structure runs counter to the previously held belief that divalent Cr would originate from Cr clusters within the van der Waals gap of this material.

The work overall demonstrates the formation of a ferromagnetic ground state for both Cr and Mn doped material. The transition temperature, below which ferromagnetic order is achieved, is currently too low for usable device applications. However, these materials provide a promising test bed for new physics and prototype devices.

Publications

The following publications have arisen in full, or in part, as a result of the work presented in this thesis.

L. J. Collins-McIntyre, W. Wang, B. Zhou, S. C. Speller, Y. L. Chen, and T. Hesjedal, 'Growth of Bi_2Se_3 and Bi_2Te_3 on amorphous fused silica by MBE' *Phys. Stat. Sol. (b)* **252** 1334 (2015).

A. I. Figueroa, G. van der Laan, L. J. Collins-McIntyre, G. Cibin, A. J. Dent and T. Hesjedal, 'Local structure and bonding of transition metal dopants in Bi_2Se_3 topological insulator thin films' *J. Phys. Chem C* **Submitted** (2015).

A. A. Baker, A. I. Figueroa, L. J. Collins-McIntyre, G. van der Laan, and T. Hesjedal, 'Spin pumping in ferromagnet-topological insulator-ferromagnet heterostructures' *Scientific Reports* **5** 7907 (2015).

L. J. Collins-McIntyre, S. E. Harrison, P. Schönherr, N. -J. Steinke, C. J. Kinane, T. R. Charlton, D. Alba-Venero, A. Pushp, A. J. Kellock, S. S. P Parkin, J. S. Harris, S. Langridge, G. van der Laan, and T. Hesjedal, 'Magnetic ordering in Cr-doped Bi_2Se_3 thin films' *Euro. Phys. Lett.* **107** 57009 (2014).

P. Schönherr, L. J. Collins-McIntyre, S. Zhang, P. Kusch, S. Reich, T. Giles, D. Daisenberger, D. Prabhakaran, and T. Hesjedal, Vapour-liquid-solid growth of ternary Bi_2Se_2Te nanowires' *Nanoscale Res. Lett.* **9** 127 (2014).

K. Virwani, S. E. Harrison, A. Pushp, T. Topuria, E. Delenia, P. Rice, A. J. Kellock, L. J. Collins-McIntyre, J. Harris, T. Hesjedal, and S. S. P. Parkin, 'Controlled removal of amorphous Se capping layer from a topological insulator' *Appl. Phys. Lett.* **105** 241605 (2014).

S. E. Harrison, L. J. Collins-McIntyre, S. Li, A. A. Baker, L. R. Shelford, Y. Huo, A. Pushp, S. S. P Parkin, J. S. Harris, E. Arenholz, G. van der Laan, and T. Hesjedal, 'Study of Gd-doped Bi_2Te_3 thin films: Molecular beam epitaxy growth and magnetic properties' *J. Appl. Phys.* **115** 2 (2014).

A. I. Figueroa, G. van der Laan, L. J. Collins-McIntyre, S. -L. Zhang, A. A. Baker, S. E. Harrison, P. Schönherr, G. Cibin, and T. Hesjedal, 'Magnetic Cr doping of Bi_2Se_3: Evidence for divalent Cr from x-ray spectroscopy' *Phys. Rev. B* **90** 134402 (2014).

L. J. Collins-McIntyre, M. D. Watson, A. A. Baker, S. -L. Zhang, A. I. Coldea, S. E. Harrison, A. Pushp, A. J. Kellock, S. S. P. Parkin, G. van der Laan, and T. Hesjedal, 'X-ray magnetic spectroscopy of MBE-grown Mn-doped Bi_2Se_3 thin films' *AIP Adv.* **4** 127136 (2014).

M. D. Watson, L. J. Collins-McIntyre, L. R. Shelford, A. I. Coldea, D. Prabhakaran, S. C. Speller, T. Mousavi, C. R. M. Grovenor, Z. Salman, S. R. Giblin, G. van der Laan, and T. Hesjedal, 'Study of the structural, electric and magnetic properties of Mn-doped Bi_2Te_3 single crystals' *New J. Phys.* **15** 10 (2013).

S. -L. Zhang, Y. Liu, L. J. Collins-McIntyre, T. Hesjedal, J. Y. Zhang, S. G. Wang, and G. H. Yu, 'Extraordinary hall balance' *Scientific Reports* **3** 2087 (2013).

S. -L. Zhang, L. J. Collins-McIntyre, J. Y. Zhang, S. G. Wang, G. H. Yu, and T. Hesjedal, 'Nonvolatile full adder based on a single multivalued Hall junction' *SPIN* **3** 1350008 (2013).

L. R. Shelford, T. Hesjedal, L. J. Collins-McIntyre, S. S. Dhesi, F. MacCherozzi, and G. van der Laan, 'Electronic structure of Fe and Co magnetic adatoms on Bi_2Te_3 surfaces' *Phys. Rev. B* **86** 081304(R) (2012).

Contents

1 Introduction **1**

1.1 Outline of Thesis 2

2 Theoretical Discussion **5**

2.1 The Hall Effects 5

2.1.1 The Hall Effect 6

2.1.2 Quantum Hall Effect 7

2.1.3 Spin Hall Effect and Anomalous Hall Effect 10

2.1.4 Quantum Spin Hall Effect 11

2.2 3D Topological Insulators 15

2.3 Broken Time Reversal Symmetry 19

2.4 Quantum Anomalous Hall Effect 21

3 Experimental Methods **23**

3.1 Molecular Beam Epitaxy 23

3.1.1 MBE: Theoretical Overview 24

3.1.2 Design of MBE System 27

3.1.3 Calibration of Elemental Sources 30

3.1.4 Substrate Preparation Methods 32

3.1.5 In-Situ Probes 32

3.2 Structural Characterisation 36

3.2.1 X-Ray Studies 38

3.2.2 Atomic Force Microscopy 41

3.2.3 Doping Concentration Determination 42

3.3 Magnetic Properties 46

3.3.1 SQUID Magnetometry 46

3.3.2 X-ray Magnetic Circular Dichroism 48

3.3.3 Polarised Neutron Reflectometry 51

4 MBE Growth of Bi_2Se_3, Bi_2Te_3 and Sb_2Te_3 **53**
4.1 Growth on Sapphire . . . 54
4.1.1 Bi_2Se_3 Growth on Sapphire . . . 56
4.1.2 Bi_2Te_3 Growth on Sapphire . . . 59
4.1.3 Sb_2Te_3 Growth on Sapphire . . . 62
4.2 Growth on Amorphous Fused Silica . . . 64
4.2.1 Motivation . . . 64
4.2.2 Experiment and Results . . . 66
4.2.3 Conclusions . . . 69
4.3 Growth of Bi_2Te_3 on Ge (111) . . . 71
4.4 Summary and Conclusions . . . 76

5 Mn-Doped Bi_2Te_3 and Bi_2Se_3 **77**
5.1 Mn-Doped Bi_2Te_3 Single Crystals . . . 77
5.1.1 Motivation . . . 78
5.1.2 Crystal Growth and Structure . . . 79
5.1.3 Magnetic Properties . . . 82
5.1.4 Muon Spin Rotation . . . 86
5.1.5 XMCD Measurements . . . 89
5.2 Mn-doped Bi_2Se_3 Thin Films . . . 98
5.2.1 Motivation . . . 98
5.2.2 MBE Growth of Mn-Doped Bi_2Se_3 . . . 99
5.2.3 Structural Characterisation . . . 100
5.2.4 SQUID Magnetometry . . . 105
5.2.5 XAS and XMCD . . . 107
5.2.6 Discussion . . . 111
5.3 Summary and Conclusions . . . 117

6 Cr-Doped Bi_2Se_3 **119**
6.1 Motivation . . . 119
6.2 Sample Preparation and Characterisation . . . 120
6.2.1 Thin Film Growth . . . 120
6.2.2 Structural Characterisation . . . 121
6.2.3 Magnetometry . . . 125
6.3 Polarised Neutron Results . . . 126
6.4 Synchrotron Studies: Evidence for Divalent Cr . . . 130
6.4.1 XAS and XMCD Studies . . . 132

6.4.2 XANES and EXAFS Studies 137
6.5 Summary and Conclusions 143

7 Summary and Outlook **145**

A Calibration of Effusion Cells **149**
A.1 Cell Pressures vs. Temperatures 149
A.2 Tuning of Eurotherm Controllers 154

B Solvent Preparation of Substrates **157**

Bibliography **158**

List of Figures

2.1 Hall bar geometry. 6
2.2 Quantum Hall Effect. 8
2.3 QHE: Electron localisation. 10
2.4 QSHE: Divided Highway. 12
2.5 QSHE: Destructive interference. 13
2.6 CdTe/HdTe Quantum Wells. 14
2.7 Diagram of band inversion. 15
2.8 Diagram of spin splitting. 17
2.9 Proposed 'flipper bridge' to Hong Kong. 18
2.10 Band structure and ARPES of Bi_2Se_3 and Bi_2Te_3. 20
2.11 ARPES of Fe-doped Bi_2Se_3. 21
2.12 QAHE observed in Cr-doped $BiSbTe_3$. 22

3.1 Effusion cell diagram. 25
3.2 Thin film growth modes. 27
3.3 Photographs of MBE system. 28
3.4 Sample holders for MBE growth. 29
3.5 Calibration of effusion cells. 31
3.6 Schematic of RHEED geometry and Ewald sphere. 33
3.7 Explanation of observed RHEED patterns. 34
3.8 RHEED Oscillations. 35
3.9 RGA Scans. 37
3.10 X-ray diffraction sets used. 39
3.11 Bragg-Brentano geometry for x-ray diffraction. 39
3.12 Explanation of features in XRR. 40
3.13 Veeco Multimode V AFM. 42
3.14 Example spectrum of EDS data. 43
3.15 Schematic 2-step model of XMCD. 49

4.1 Crystal structure of $(Bi/Sb)_2(Te/Se)_3$. 54
4.2 Sapphire RHEED pattern. 56
4.3 RHEED pattern and AFM scan of Bi_2Se_3 film on sapphire. 57
4.4 X-ray studies of Bi_2Se_3 film on sapphire. 58
4.5 RHEED studies of Bi_2Te_3 film on sapphire. 59
4.6 AFM studies of Bi_2Te_3 film on sapphire. 61
4.7 X-ray studies of Bi_2Te_3 film on sapphire. 62
4.8 RHEED studies of Sb_2Te_3 film on sapphire. 63
4.9 X-ray studies of Sb_2Te_3 film on sapphire. 64
4.10 AFM studies of Bi_2Se_3 and Bi_2Te_3 films on fused silica. 66
4.11 X-ray studies of Bi_2Se_3 and Bi_2Te_3 on fused silica substrates. 68
4.12 ARPES spectra of Bi_2Te_3 film on fused silica. 70
4.13 RHEED studies of Ge (111) substrate. 72
4.14 RHEED studies of Bi_2Te_3 thin film on a Ge (111) substrate. 72
4.15 AFM studies of Bi_2Te_3 film on Ge (111). 74
4.16 X-ray studies of Bi_2Te_3 film on Ge (111). 75

5.1 Crystal structure and XRD of Mn-doped Bi_2Te_3 bulk samples. 80
5.2 EDX measurements showing of Mn-doped Bi_2Te_3 bulk samples. . . . 81
5.3 TEM images of Mn-doped Bi_2Te_3 bulk samples. 82
5.4 SQUID measurements of Mn-doped Bi_2Te_3 bulk samples. 84
5.5 Muon spin rotation of Mn-doped Bi_2Te_3. 88
5.6 XAS and XMCD of Mn-doped Bi_2Te_3 bulk samples. 90
5.7 XMCD measurements as a function of temperature and field. 93
5.8 AFM measurements of Mn-doped Bi_2Se_3 thin film. 100
5.9 XRD and XRR of Mn-doped Bi_2Se_3 thin film. 101
5.10 XRD of high Mn dopings of a Bi_2Se_3 thin film. 102
5.11 RBS data compared with beam flux monitor. 104
5.12 SQuID magnetometry of 7.5 at.% Mn-doped Bi_2Se_3 thin film. 106
5.13 XAS and XMCD of Mn-doped Bi_2Se_3 thin film. 109
5.14 Mn magnetic moment as a function of dopant concentration from XMCD. 110
5.15 XMCD measurements of 7.5 at.% Mn-doped Bi_2Se_3 thin film. 112
5.16 XMCD hysteresis at the Mn L_3 edge for a 12 at.% Mn-doped Bi_2Se_3. 113

6.1 RHEED and AFM of Cr-doped Bi_2Se_3 thin film. 122
6.2 XRD of Cr-doped Bi_2Se_3 thin film. 123
6.3 XRD of highly Cr-doped Bi_2Se_3 thin film with parasitic peaks. 124

6.4 SQUID magnetisation studies of a Cr-doped Bi_2Se_3 thin film. 127
6.5 PNR studies of Cr-doped Bi_2Se_3 thin film. 128
6.6 Measured XMCD of Cr-doped Bi_2Se_3 thin film compared with a Cr_2O_3 reference sample. 133
6.7 XMCD spectra of Cr-doped Bi_2Se_3 thin film highlighting the bulk and surface contributions. 136
6.8 XMCD hysteresis loops of a Cr-doped Bi_2Se_3 thin film. 138
6.9 EXAFS and XANES data for a Cr-doped Bi_2Se_3 thin film. 140
6.10 Diagram of bonding scenarious between Cr/Bi and Se. 142

A.1 Calibrations of main cells. 150
A.2 Calibrations of dopant cells. 151

Chapter 1

Introduction

Topological insulators (TIs) are a recently discovered, novel state of matter exhibiting a wide variety of novel physical properties and underpinned by newly developed topological band theory [1, 2, 3, 4], based on earlier work by Haldane [5]. Normal band insulators have been a mainstay of condensed matter physics research for decades and a great deal of progress has been made in electronics and computation through the manipulation of, for example, semiconductors. Conventionally phases of materials are classified according to broken symmetries, e.g. water freezing into ice breaking translational and rotational symmetry. Topological insulators are classified in an entirely new manner, based on topological invariants defined within existing band theory. Such a material classification predicts a wider range of possibilities than previously thought to exist within a number of material classes. The prototypical 3D TIs Bi_2Se_3 and Bi_2Te_3, for example, have been well known as promising thermoelectric materials [6, 7] long before any detailed investigation was made of their band structure [8] within the context of newly predicted TIs. Such materials now promise the discovery and investigation of a wide range of novel physical phenomena such as: quantum spin Hall effect [1, 4] - predicted in graphene [2], HgTe quantum wells [9] and 3D TIs [10], quantum anomalous Hall effect [11] - observed in Cr-doped

$Bi_xSb_{2-x}Te_3$ [12], topological magneto-electric effect [13] leading to image magnetic monopoles [14], and Majorana Fermions [15, 16]. It is further hoped that exploitation of these physical effects may lead to significant breakthroughs in emerging fields such as spintronics [17] and quantum computation [18, 19].

A promising avenue of research for the development of functional TI devices has involved the doping of thin film and bulk samples with transition metal [20, 21, 22, 23] and rare earth elements [24, 25]. This approach aims to locally break the intrinsic time-reversal symmetry of the TIs and open a surface band gap in the topological surface state. It is anticipated that such a band structure could be useful for spintronics and quantum computation by manipulating the surface Majorana Fermion as an 'emergent particle' [26].

1.1 Outline of Thesis

This thesis will focus on the formation of magnetic order in TI thin films (Bi_2Te_3 and Bi_2Se_3) through doping with transition metal elements. The structural, magnetic and electronic properties of the grown films are presented alongside detailed information regarding the optimum growth conditions for these samples. A variety of synchrotron and neutron-based techniques are employed to investigate the magnetic ground state of grown films. This work comprises a series of sub-projects each focussing on different approaches (e.g. various dopant elements) within the same theme of TI thin films. In general, chapters are built around existing reviewed publications arising from this work and relevant papers are highlighted at the beginning of each chapter. Chapter 2 provides an overview of the relevant theory of TIs and a general background of the field so far. Chapter 3 describes the theory and practical aspects of the experimental techniques applied during this thesis. Chapter 4 provides an insight into the growth of basic undoped binaries of Bi_2Se_3, Bi_2Te_3 and Sb_2Te_3 by MBE on various substrate

materials. Chapters 5 and 6 present the core insights from this work, doping TIs with Mn and Cr respectively. Finally, chapter 7 summarises the main findings of this work and presents an outlook on the field as it stands.

Chapter 2

Theoretical Discussion

The theory of TIs has been recently developed and is still emerging as an ongoing narrative in theoretical as well as experimental communities. This chapter is intended to present a qualitative overview of the relevant theory sufficient to understand the nature of these novel materials and the experimental direction taken in further chapters. This chapter also serves to highlight the relevant literature which may be consulted for the full derivation of the relevant theory.

2.1 The Hall Effects

To properly understand the underpinning physics that drives topological insulators it is first necessary to examine the Hall effect and its many (quantised) siblings. These effects have a been a mainstay of condensed matter physics research for more than 100 years and remain an interesting and developing avenue of research. An overview of the 'Hall effects' are shown in Tab. 2.1 and it is worth giving an overview of each, with particular focus on the quantum spin Hall effect (QSHE) and quantum anomalous Hall effect (QAHE).

Hall Effect (1879)	Spin Hall Effect (1889)	Anomalous Hall Effect (2004)
Quantum Hall Effect (1980)	Quantum Spin Hall Effect (2006)	Quantum Anomalous Hall Effect (2013)

Table 2.1: Summary of the Hall effects and year of discovery for each.

2.1.1 The Hall Effect

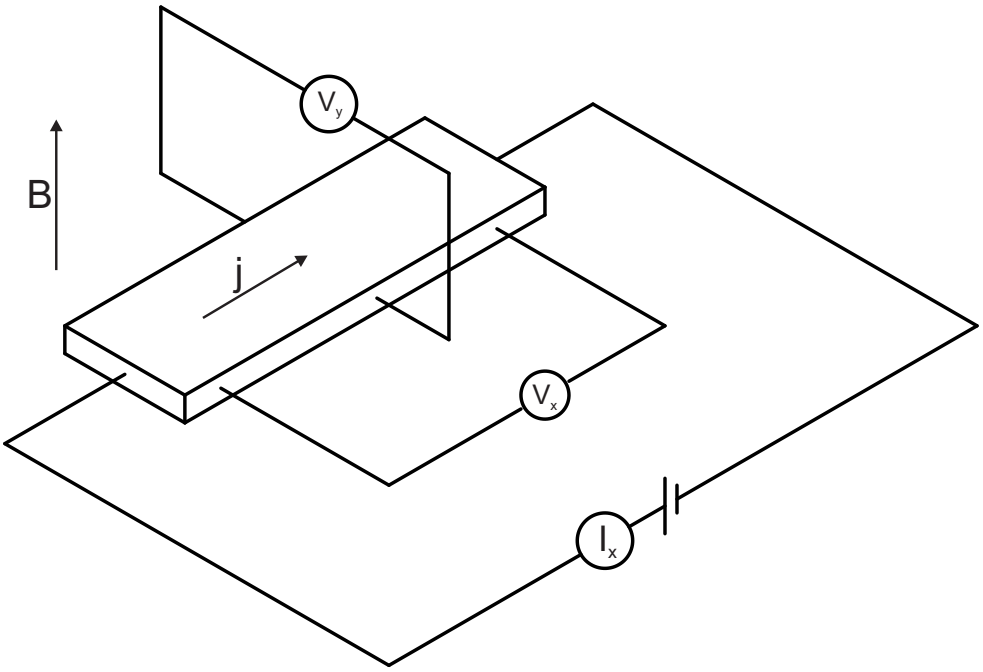

Figure 2.1: Typical geometry of the Hall effect. Current (I_x) flows in-plane, perpendicular to an applied field B inducing a mutually orthogonal potential V_x by action of the Lorentz force.

The Hall effect may occur for a given sample with electrons travelling with respect to an applied magnetic field, with at least some velocity component being orthogonal to the field. For simplicity we may consider the system as shown in Fig. 2.1, where the electron velocity is perpendicular to the applied field. In this case the Lorentz force will act on the electrons as described in Eq. 2.1, where $\vec{v}$ is the electron velocity and $\vec{B}$ the externally applied magnetic field.

$$\vec{F} = -e\vec{v} \times \vec{B}. \tag{2.1}$$

This Lorentz force will obviously act in the third direction, orthogonal to both applied field and electron velocity, causing the flowing electrons to travel a curved path through the sample. This in turn sets up an electric field (E_H) defined by Eq. 2.2, where R_H is the Hall resistance and $\vec{j}$ the current density.

$$\vec{E_H} = R_H \vec{B} \times \vec{j}. \tag{2.2}$$

In short, a measurable potential is invoked across the sample by means of interaction of an external magnetic field and the charge carriers of the material. From this one may determine the Hall resistance R_H. It is worthy of note that the Hall resistance allows a direct extraction of the electron density by the relation $R_H = -1/ne$, where e is the electron charge and n the carrier density. This argument is made for electrons, though the same physics holds true for holes in p-type materials.

2.1.2 Quantum Hall Effect

The Quantum Hall Effect (QHE), first observed by von Klitzing and well discussed in Ref. [27] is an effect observed in certain semiconducting materials under the influence of an applied external magnetic field. It can be considered in a similar way to the Hall effect and we shall use the same sample geometry as previously depicted.

A two dimensional electron gas (2DEG) may be considered a sea of free electrons in 2 dimensions that are confined by an 'infinite' potential in the third. Under the application of low temperatures and high external magnetic fields the electronic states in such a material (GaAs/AlGaAs quantum wells for instance) will be confined to discrete Landau levels described by the Hamiltonian in Eq. 2.3.

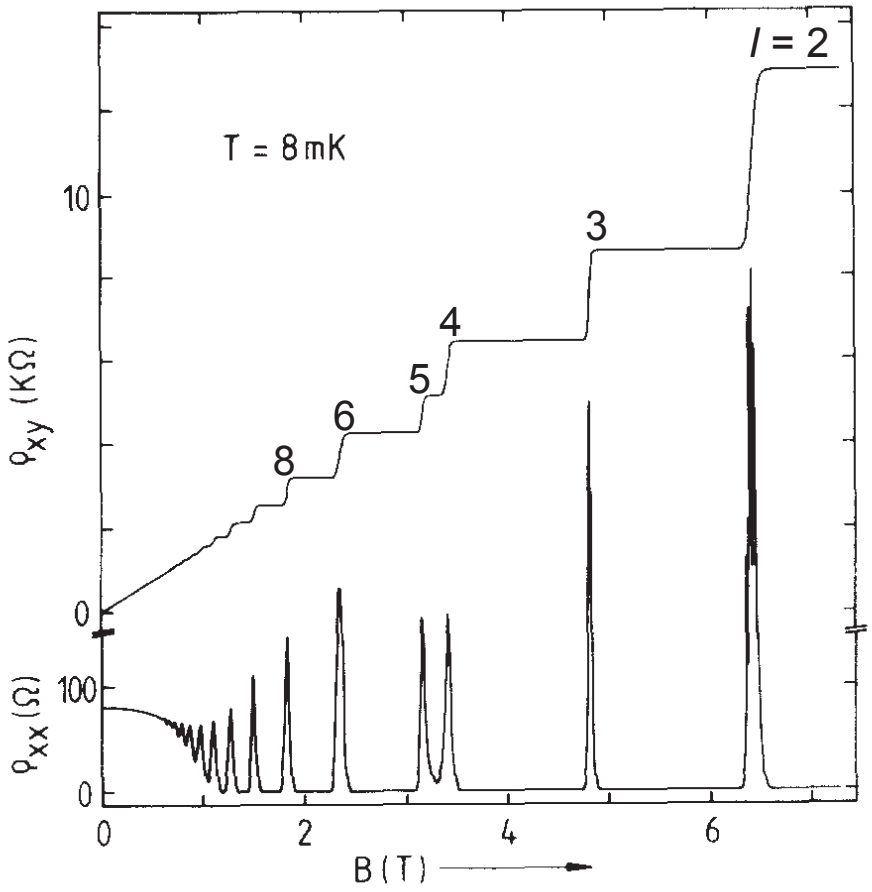

Figure 2.2: Transverse and longitudinal components or resistivity showing the quantum Hall effect for a GaAs-$Ga_{0.71}$Al0.29As heterostructure. ρ_{xy} shows quantisation in units of $-h/ie^2$ where i is an integer. Figure from Ref. [27].

$$\hat{H} = \frac{\hat{p_x^2}}{2m} + \frac{1}{2}m\omega_c^2 \left(\hat{x} - \frac{\hbar k_y}{m\omega_c} \right)^2 , \tag{2.3}$$

where $\hat{H}$ is the Hamiltonian operator, $\hat{p_x^2}$ the momentum operator (in x), m the mass (or effective mass), ω_c is the electron cyclotron frequency, $\hat{x}$ is the x position operator and k_y is the momentum in the y direction. From this it is easy to see by analogy with the harmonic oscillator that the electrons described by this Hamiltonian will form quantised energy levels with eigenvalues, where $n \geq 0$:

$$E_n = \hbar\omega_c \left(n + \frac{1}{2} \right). \tag{2.4}$$

The electron energies are now quantised in units of ω_c, their cyclotron frequency, which is itself a function of the externally applied magnetic field, electron charge and mass ($\omega_c = eB/m$).

Deriving from this basic principle there are two main observable effects (as in Fig. 2.2): the vanishing of longitudinal resistivity and the quantisation of transverse resistivity as ($\rho_T = -h/ie^2$) where i is an integer. A full and detailed derivation is beyond the scope of this thesis and the reader is instead directed to Ref. [27]. In short, in an increasing magnetic field the energy of the Landau levels increases and electrons will occupy only the lowest energy levels up to the chemical potential. As the field increases the occupation of the higher energy levels decreases as more are accommodated in the lower Landau levels. The discrete changes in the quantisation of resistivity occur when an exact integer (n) Landau levels are filled, a state that occurs for each $B_i = \frac{n_A h}{ie}$, where n_A is the electron density.

This discussion has so far omitted to mention edge states, which can be understood semi-classically by consideration of the Lorentz force. An externally applied magnetic field of sufficient strength will cause the bulk electrons to become localised within their cyclotron orbits and therefore effectively bulk insulating. At the edge of the

material, however, there will be some electrons for whom their localised path brings them to the edge of the material. These edge electrons will 'skip' along the interface creating a 1D channel of spin-polarised electrons at this edge. This state is illustrated diagrammatically in Fig. 2.3. This is the first example here of a topologically non-trivial bulk band structure driving a defined edge or surface state.

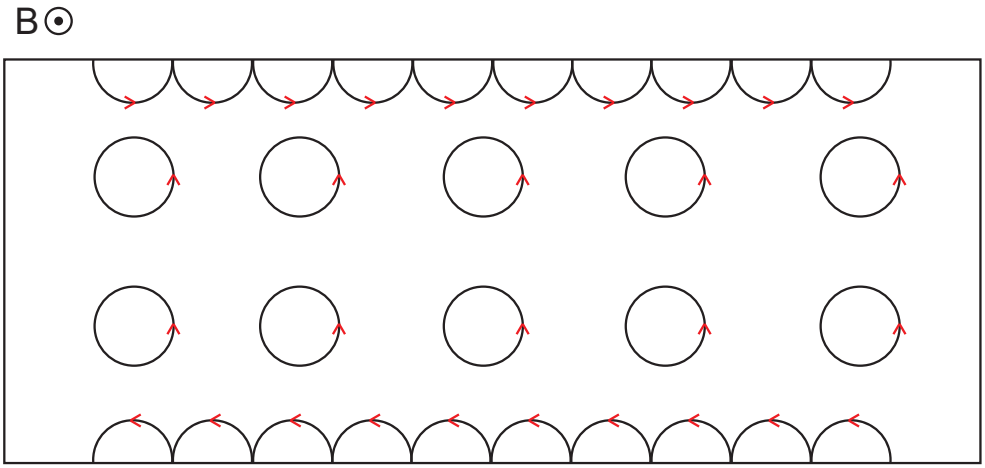

Figure 2.3: Diagrammatic picture of the electron localisation into cyclotron orbitals leading to edge states.

This simplification is, of course, flawed as it considers only single electrons rather than bands. A fuller discussion must concentrate on the bending of the Landau level bands towards the edges of the sample, creating a confinement potential for the edge electrons.

2.1.3 Spin Hall Effect and Anomalous Hall Effect

Both the spin Hall effect (SHE) and anomalous Hall effect (AHE) occur in materials with strong spin-orbit interaction and in the absence of an applied magnetic field. The SHE (see Ref. [28]) describes an accumulation of electrons of differing spin towards the edges of a current carrying sample, in a similar manner to the Hall effect causing an accumulation of differing charge. This effect is often described by analogy to a

spinning tennis ball, which deviates from its straight path, left or right, depending on its spin causing a torque by interaction with the air. Similarly here the electron spin exerts a torque through the spin-orbit interaction.

The anomalous Hall effect essentially replaces the externally applied field of the Hall effect with an internal magnetisation, i.e., in a ferromagnetic material. It is detectable as an additional term to the Hall effect, which is often much larger than the 'ordinary' Hall effect. The end result will be a reversal in the sign of the measured Hall resistance (R_H) for an equivalent reversal of the sample's net magnetisation. This effect originates again from the spin-orbit interaction and can be considered as originating from intrinsic (Berry-phase curvature) and extrinsic processes. Examples of extrinsic processes are skew-scattering from impurities or side-jump scattering from impurities or electron-phonon interactions. An in-depth discussion of this effect is given by Ref. [29].

2.1.4 Quantum Spin Hall Effect

The quantum spin Hall effect (QSHE) is the firm foundation of the 2D topological insulators. A model for this effect was first proposed by Kane & Mele [1] and it can be understood in brief as a doubling of the previous model proposed by Haldane [5], incorporating the electron spin as up and down channels. Given its relevance to the remainder of this thesis, this effect will be discussed purely within the context of topological insulators.

This discussion should begin by analysis of the similarities and differences between this and the QHE. The most notable difference being the absence of an applied field and by extension that this state now conserves time-reversal symmetry (TRS).

As in the QHE, we have a 'divided highway' across the sample. In the quantum Hall (QH) state electron channels for $+k_x$ and $-k_x$ are separated across the width of

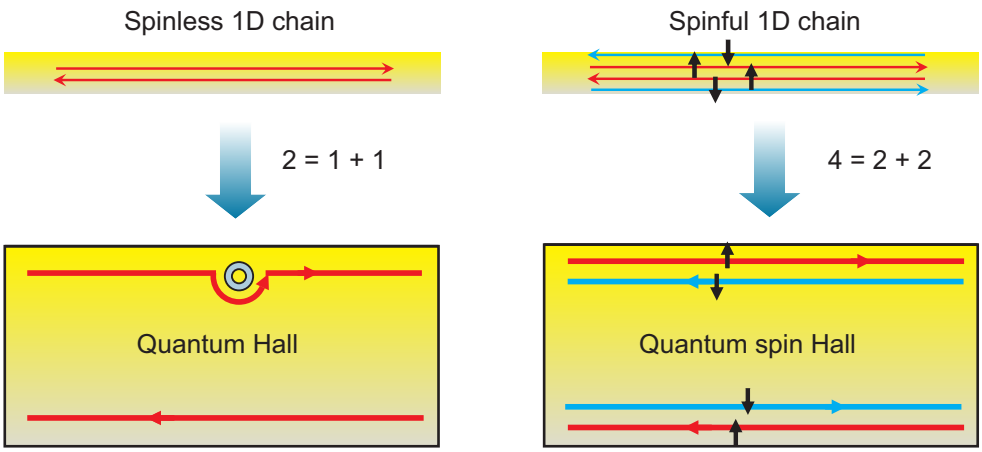

Figure 2.4: Left: QHE with both right-moving and left-moving edge states. These states are robust to scattering by impurities. Right QSHE with upper state right-moving spin up and left-moving spin down. The lower state is inverted by comparison. Back-scattering is suppressed from non-magnetic impurities. Figure from Ref. [30].

the sample (Fig. 2.4 [left]) and so scattering is suppressed by this spatial separation. Note that in 1D, electrons may move in one of only two possible directions, this process would not suppress scattering in 2D. Figure 2.5 illustrates the dissipationless transport in this state since, on encountering an impurity, a given electron will detour around rather than back-scatter. In the quantum spin Hall state (QSH) we additionally consider the spin degree of freedom for the electron. This time-reversal invariant splitting of states does not require the application of an external field. Figure 2.4 [right] demonstrates the new setup with the 4-channel 'divided highway'.

This state prohibits back-scattering from non-magnetic impurities by virtue of some interference properties. Figure 2.5 illustrates the case for a spin up electron encountering an impurity and back-scattering through two possible mechanisms, each involving a continuous rotation about the impurity. The clockwise path rotates the electron spin by π and the anti-clockwise path by $-\pi$ leading to a path difference of 2π. Please note that the TRS of the state is essential as it gives equal probability to each scattering path. Since spin-1/2 wavefunctions (Fermions) invert sign under a 2π rotation these paths will destructively interfere, allowing for dissipationless transport

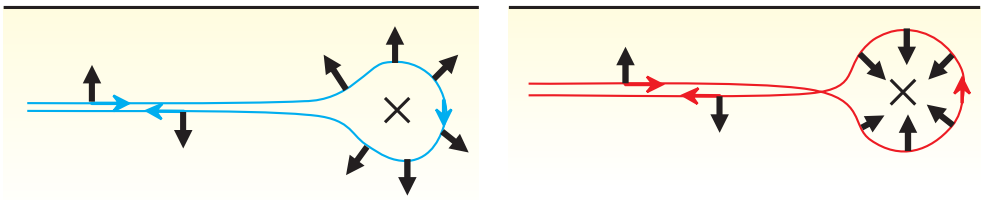

Figure 2.5: Diagrammatic depiction of the two different scattering paths around an impurity for the quantum spin Hall state. The total path difference between them is 2π, leading to total suppression of the back-scattering for Fermions. Figure from Ref. [30].

of the electrons. This is essentially the same mechanism by which anti-reflective coatings operate, exploiting destructive interference to suppress a scattering channel. If TRS is broken (by an applied field or magnetic impurity) this is no longer the case and back-scattering may occur. Control of such a scattering process is the main mechanism on which it is hoped TI-based devices may be built.

This requirement is a core principle of topological insulators and is characterised by the $\mathbb{Z}_2$ topological invariant (see Eq. 2.5), defined to be 0 for topologically trivial materials and 1 for topologically non-trivial materials. The manner in which such spin-momentum locked states may occur in a topologically non-trivial way is via the strong spin-orbit coupling present in heavy-element materials. The spin-orbit interaction leads to an 'inverted' band structure, like that of Fig. 2.6. A more in-depth discussion of the role of spin-orbit coupling will be given later in the context of 3D TIs.

The first experimentally observed example of the QSH state was in CdTe/HgTe quantum wells [31]. In these structures, above a certain critical thickness, there is a band inversion of the E1 and H1 sub-bands that gives rise to a non-trivial band topology. This non-trivial bulk band topology leads to two 1D spin-polarised conducting channels at the edge, each carrying one quantum of conductance (e^2/h). The

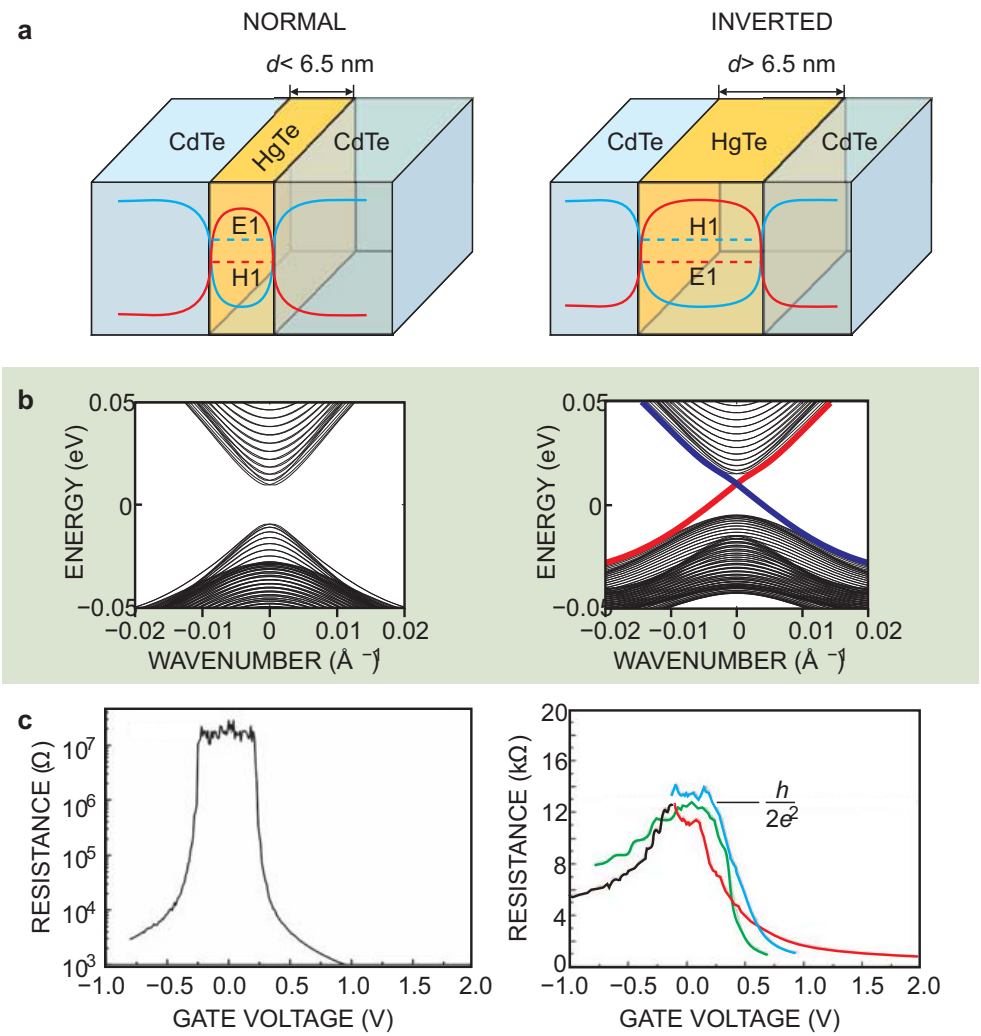

Figure 2.6: (a) The CdTe/HgTe quantum well structure has a transition from topologically trivial to non-trivial band structure above a critical thickness d. (b) Above this critical thickness the band structure evolves to possess spin-polarised edge states within the bulk band-gap. (c) QSHE in CdTe/HgTe quantum wells, demonstrating quantised conduction through the edge channels. The quantisation of conduction ($h/2e^2$) is observed for devices of varying widths (indicated by varying colours) and demonstrates this to be purely an edge effect. Figure from Ref. [30].

crossing point at the 0-momentum (Γ-point) is protected by TRS and is the characteristic signature of a QSH state or topological insulator. The requirement for at least a doubly degenerate state at this point is described by Kramers' theorem [32].

2.2 3D Topological Insulators

Although it is significantly easier to visualise the theory of these materials in 2D with 1D edge states, the majority of applicable materials are in fact 3D with 2D surface states. For this discussion, I will broadly follow the excellent overview of these materials given in Ref. [33].

This discussion will seek to provide an overview of the 3D topological insulators, which are characterised as bulk band insulators with a surface spin-polarised metallic state. It is worth noting that for the particular materials discussed in this thesis (Bi_2Te_3 and Bi_2Se_3), they are not true bulk insulators, but are perhaps better described as narrow band-gap semiconductors, with $E_g \approx 300$ meV. This narrow bulk band-gap is an issue for the detailed investigation of the electronic properties of such materials as it becomes challenging to deconvolve the bulk and surface electronic properties.

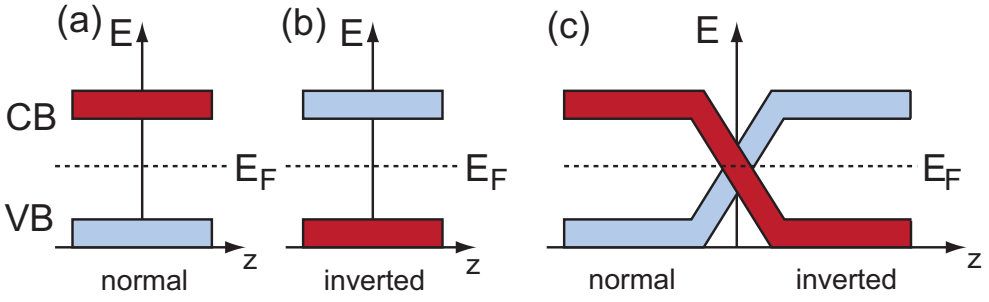

Figure 2.7: Toy model band diagram of the interface between a topologically trivial and non-trivial band structure. (a) Negative parity (blue) and positive parity (red) bands in normal configuration for a semiconductor. (b) Inverted parity band structure due to strong spin-orbit coupling. (c) Joining these structures continuously leads to an enforced crossing point at the surface, a metallic state. Figure from Ref. [33].

To consider how these metallic surface states may occur we shall start with a toy model of a typical gapped semiconductor as shown in Fig. 2.7(a). Here there is the typical direct band-gap E_g separating the valence and conduction bands with the Fermi level E_F situated inside the band-gap. For this discussion it is expected that all valence states are full and the conduction states are empty. For this (and most) semiconductors the maximum of the valence band will typically have a negative parity (p character) and the minimum of the conductance band to have positive parity (s character). Under the effect of spin-orbit coupling it is possible to lift the degeneracy of the p-state, splitting into two states of $j = 3/2$ and $j = 1/2$ (see Fig. 2.8). This effect happens to a degree in all materials, but with very strong spin-orbit coupling the $j = 3/2$ state can be driven above the energy of the s-state, effectively leading to an inversion of the parity of the bands. One must generally consider the full parity of the band structure to determine the topological character. The change between topological states may be driven by the change in parity of only one band, usually the top-most band. It is the interface between parity-inverted and non parity-inverted bands that gives rise to the surface topological state. This situation is shown diagrammatically in Fig. 2.7(c).

It is worthwhile emphasising that this metallic surface state is entirely arising from the bulk band structure and not some unique property of the surface. This is critical as it means real experimental effects, such as surface oxidation or diffuse interfaces, should not disrupt the surface state. These effects may make it harder to detect the topological surface state with many commonly employed tools, but the symmetry of the bulk band structure necessitates this crossing point at the interface.

A frequently used example to illustrate this point is the proposed 'flipper bridge' connecting mainland China (driving on the right) with Hong Kong (driving on the left), as shown in Fig. 2.9. Here the 'bulk bands' are represented by the left- and right-hand (positive and negative parity) road structure in each of the regions. In

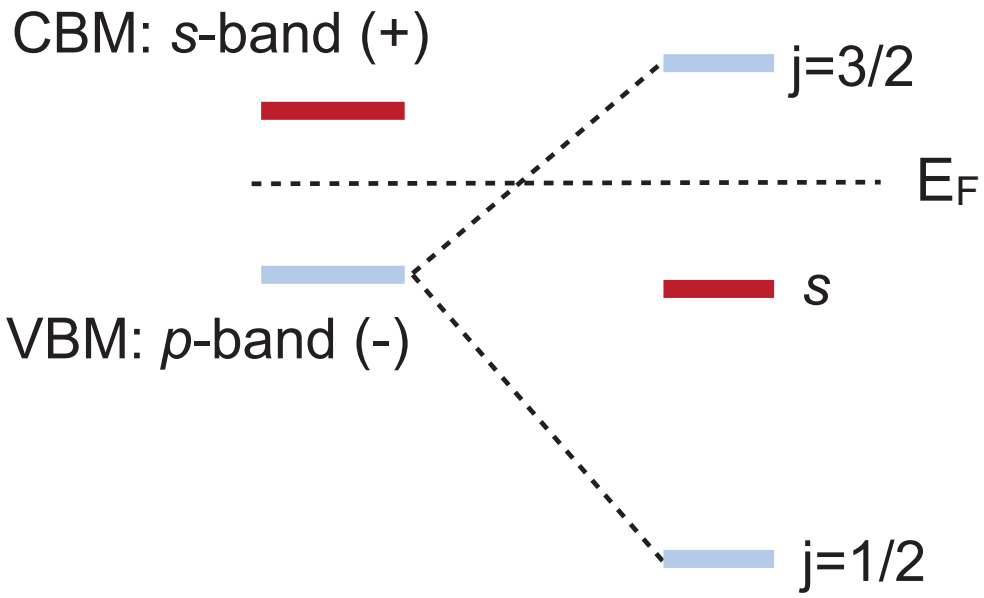

Figure 2.8: Diagrammatic representation of strong spin-orbit coupling on the symmetry of the band structure. For strongly spin-orbit split states the degeneracy of the p level is lifted such that the $j = 3/2$ is above the s level, leading to a parity inverted bulk band-gap. Figure from Ref. [33].

order to connect one to another continuously there must be some 'surface' crossover point. This example is useful to point out a few key features:

- A single crossing point is not the unique solution, but it is the simplest. The topological problem is soluble for any odd number of crossings.
- The nature of the surface (river) is irrelevant to this consideration and has no impact on the crossing point.
- Any smooth change (maintaining parity) to the main roads (bulk bands) will have no impact on the crossing point. It is therefore robust.

This description is, naturally, a simplification from the true theoretical approach, but well illustrates the origin of the novel surface properties of these materials. As mentioned within the context of QSHE, time reversal symmetry plays a critical role in the protection of this surface state. TRS mandates that for a certain wavefunction

Figure 2.9: 'Flipper bridge' connecting Hong Kong to mainland China requires a crossover point due to the different road 'parity' in each country. Figure from Nl Architects - www.nlarchitects.nl.

defined with wavevector and spin as $(\vec{k}, \uparrow)$ then, by symmetry, there must also exist $(\vec{k}, \downarrow)$. So for $\vec{k} = 0$ it must be therefore true that the two spin states are degenerate (Kramers' theorem). Conventionally this point in the Brillouin zone is labelled the Γ-point and the crossing states at this point are protected against any band-gap opening by TRS. Such a point is, in general, called a time-reversal invariant momenta (TRIM) and though we will focus on states at the Γ-point in this work it should be noted that TRIM points also exist at other high-symmetry points in reciprocal space.

The important parameter to note between topologically trivial and non-trivial insulators is the number of Fermi level crossings between two surface TRIM points. In general, an even number of crossings is trivial and such crossing points may be removed by a smooth deformation of the bands. An odd number of crossings (1 in our case) is non-trivial and no smooth change to the band structure may remove the crossing point. This criteria is predicted fully by the nature of the bulk band

structure. This is parameterised in the $\mathbb{Z}_2$ topological invariant (ν_0), which may be fully calculated by consideration of the bulk band structure according to Eq. 2.5.

$$(-1)^{\nu_0} = \prod_{i=1}^{n} \delta\left(\Gamma_i\right), \tag{2.5}$$

where n, the number of bulk TRIM points, is 8. $\delta\left(\Gamma_i\right)$ is the parity invariant for each occupied band for the relevant TRIM - Γ_i. This is defined as $\delta\left(\Gamma_i\right) = \prod_n \xi_{2n}\left(\Gamma_i\right)$, where $\xi_{2n}\left(\Gamma_i\right) = \pm 1$ are the parity eigenvalues of the $2n$ occupied band at the TRIM. This relation gives us, in general, $\nu_0 = -1$ for a topologically non-trivial band structure and $\nu_0 = 1$ for a trivial one. In the case of Bi_2Se_3 and Bi_2Te_3 the topological invariant is 1 for all TRIM other than that Γ-point (where it is -1) and so the total product is -1, a topological insulator.

The existence of the topological surface state in these materials was predicted by band structure calculations [34] [Fig. 2.10 (a),(b)] and later confirmed by angle-resolved photoemission spectroscopy (ARPES) [35, 36] [Fig. 2.10 (c),(d)].

2.3 Broken Time Reversal Symmetry

It should be clear by now that TRS is a core part of the what makes a topological insulator the interesting material that it is. It is of interest, therefore, to consider what happens in the case that this symmetry is broken and also what processes break it.

Broken symmetry is a much studied area of physics in general and within condensed matter has been utilised widely as a tool for the classification of materials, particularly that of crystals. A perfect example of such is the phase transition between water and ice. Water possesses full translational and rotational symmetry, undergoing a transition to ice breaks this symmetry as it is now only rotationally

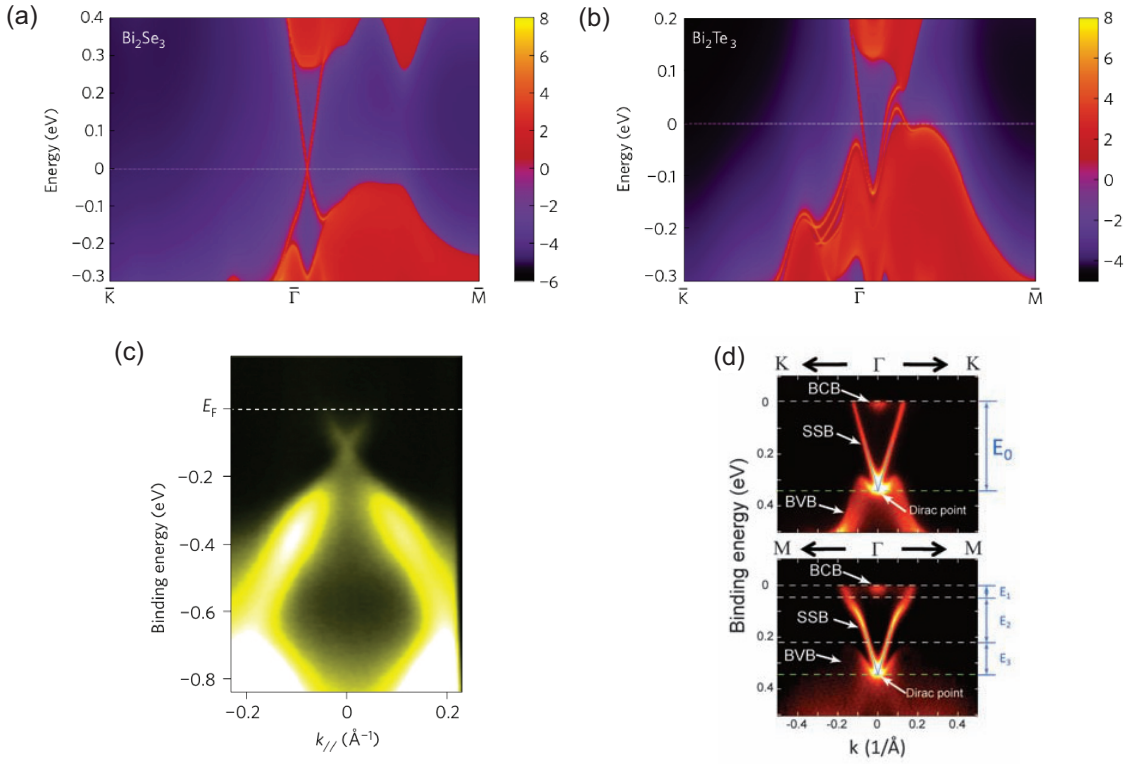

Figure 2.10: (a), (b) Band structure calculations of Bi_2Se_3 and Bi_2Te_3 respectively, showing the Dirac point crossing at 0 momentum. From Ref. [34]. (c) ARPES of Bi_2Se_3 showing Dirac point in the band dispersion. From Ref. [35]. (d) ARPES of Bi_2Te_3 similarly showing the Dirac band dispersion. From Ref. [36].

and translationally invariant along defined directions within the crystal. Thus, the breaking of symmetry provides a definable way of identifying phases of matter and accompanying phase transitions.

It is predicted that, under the application of a TRS-breaking action, e.g., out of plane magnetic fields or ferromagnetic order, a gap will open in the topological surface state [13]. This transition is then between the band structure of a massless to a massive Dirac Fermion. A Dirac Fermion is a Fermion that is not its own anti-particle, with a dispersion relation described by a Dirac cone, like in the TSS. The mass described here is an effective mass, related to the direct band gap, similar to the standard formulation for semiconductors. This effect has been first noted in Bi_2Se_3

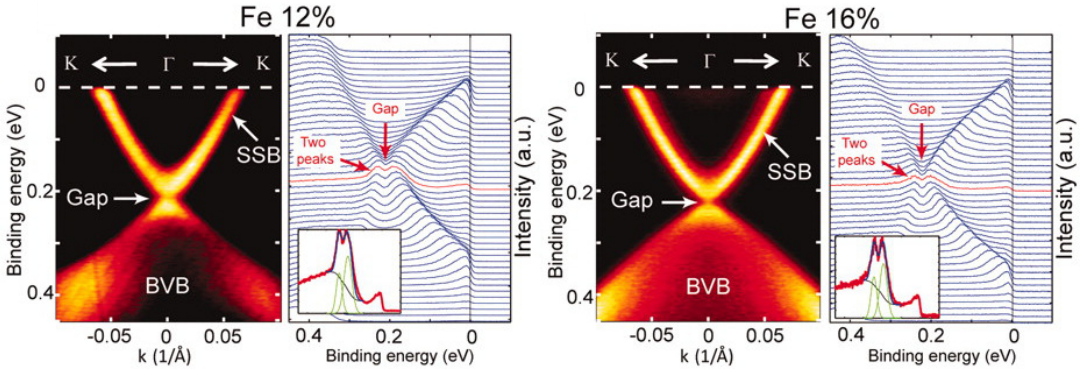

Figure 2.11: Bi_2Se_3 doped with varying levels of Fe in the bulk of the film. A gap opening at the Γ-point is seen as a function of doping. From Ref. [37].

doped with magnetic elements, which introduce an opening of the surface bands (Fig. 2.11) [37]. This doping will break TRS for either bulk ferromagnetism achieved through homogeneous doping or for purely surface ferromagnetism mediated through the RKKY interaction.

It is hoped that control of these massive Dirac Fermion states may lead to the discovery of new physical effects and accompanying breakthroughs in spintronics and quantum computation. For example, with a massive Dirac Fermion with E_F tuned into the surface band gap, one may see the image magnetic monopole [38].

2.4 Quantum Anomalous Hall Effect

Building on the idea of broken TRS, the quantum anomalous Hall effect (QAHE) is a predicted and recently observed effect in such TRS-broken systems. This quantised version of the AHE has been predicted to occur in topological insulators with a massive Dirac Fermion arising from broken TRS and with the Fermi level tuned into the induced band-gap [39]. This effect exhibits the same quantised plateaus in conductance as does the QHE, but without the application of an applied external magnetic field. This fact makes this a highly promising effect to exploit in the future

development of logical applications which may use the quantised state to encode a given logical state.

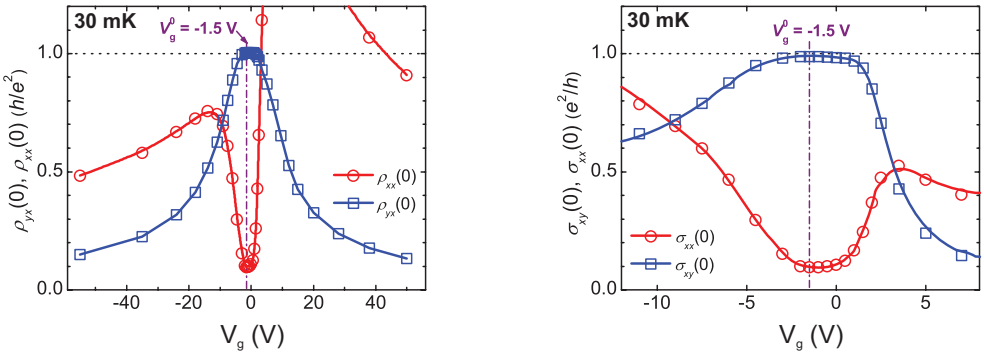

Figure 2.12: Quantised resistivity (left) and conductance (right) observed in $Cr_{0.15}(Bi_{0.1}Sb_{0.9})_{1.85}Te_3$ thin films in the absence of applied magnetic field. From ref. [12].

The QAHE was recently observed in $Cr_{0.15}(Bi_{0.1}Sb_{0.9})_{1.85}Te_3$ thin films with the Fermi level tuned into the band-gap [12]. Their results clearly demonstrate the anticipated quantisation of resistivity in the absence of an applied field (Fig. 2.12), at very low temperatures ($\sim$ 30 mK). This discovery brings forward the possibility of observing the QAHE in other transition metal doped chalcogenide TIs, a clear driving force behind further study of the magnetic properties of these materials under doping.

Chapter 3

Experimental Methods

A variety of techniques have been used during the course of the research presented in this thesis. The focus of the work centres on thin film samples fabricated by molecular beam epitaxy (MBE). These samples are then characterised by a variety of lab based analysis tools: x-ray diffraction (XRD), atomic force microscopy (AFM) and SQUID magnetometry as well as experiments at large scale facilities: Diamond Light Source (UK), ISIS Neutron and Muon Source (UK) and Advanced Light Source (USA). In this chapter an overview of the relevant theory as well as practical details of the experimental methods employed will be given.

3.1 Molecular Beam Epitaxy

MBE has been the dominant growth technique for high quality III-V semiconductor thin films since the 1970s. This method of thin film deposition distinguishes itself from other vacuum-based evaporation techniques by its very fine control over elemental source temperatures, and therefore beam fluxes, as well as the precise control of the substrate conditions, affecting deposition [40]. It is a non-equilibrium growth method, allowing the fabrication of single crystal thin films at low substrate temperatures in a manner that is not possible with standard solid-state crystal fabrication methods.

The co-evaporated molecular beams may be considered non-interacting in the gas phase and so the thin film growth takes place purely as a surface reaction. This allows fine control over the deposition conditions and surface reaction by means of the substrate temperature. This non-equilibrium growth can also be exploited to permit the incorporation of dopants at higher concentrations, without the formation of secondary phases, than is typically possible by solid state methods. This fact forms the main justification for the usage of MBE as a tool for the investigation of magnetically doped TIs.

3.1.1 MBE: Theoretical Overview

MBE is an ultra-high vacuum (UHV) technique; there is no exact pressure at which it may be said the UHV conditions have been achieved, though it is generally accepted that pressure in the range of 10^{-9} Torr and below are within UHV conditions. From thermodynamical considerations it can be demonstrated that the mean free path (λ) of a single molecule in an ideal gas is given by:

$$\lambda = \frac{RT}{\sqrt{2}\pi d^2 N_A P}, \tag{3.1}$$

where R is the Rydberg gas constant, T the temperature, d the diameter of the gas molecules, N_A is Avagadro's number and P the gas pressure. Our MBE system has a base pressure of $\sim 2 \times 10^{-10}$ Torr, which for diatomic nitrogen molecules at room temperature, gives a mean free path of $\lambda \approx 1450$ km, clearly many orders of magnitude greater than our vacuum chamber size. So it is reasonable, therefore, to assume that any given molecule of gas may travel within the chamber as if it were a perfect vacuum. It is worth noting that even for typical beam pressures of $\sim 1 \times 10^{-6}$ Torr the mean free path is still around $100 - 300$ m, so even the molecular beams themselves are broadly non-interacting.

The reason for this exceptionally pure vacuum environment is to permit the epitaxial deposition of atomic layers without a significant incorporation of unwanted dopants. Thin films grown by MBE may have a typical deposition rate of $\sim$1 nm/min, so UHV conditions are required to ensure each layer has as few incorporated impurities as is possible. The methods by which this pure vacuum is achieved are discussed later.

In this thesis, thin films were deposited from elementally pure sources using effusion (Knudsen) cells, a diagram of which is shown in Fig. 3.1. The effusion cells consist of the source material held within a suitably non-reactive crucible (usually pyrolytic boron nitride or alumina) with a wound filament of refractory metal (usually W or Ta). A thermocouple is placed in thermal equilibrium with the crucible material and is used in connection with a suitable temperature controller (Eurotherm here) to regulate the power applied to the cell. Refractory metal (usually Ta) heat shields surround the cell to prevent heat losses and unwanted heating of surrounding cells. Some effusion cells also employ water cooling for thermal stability, though ours do not as this effect is achieved through contact with a cryo-shroud (discussed later).

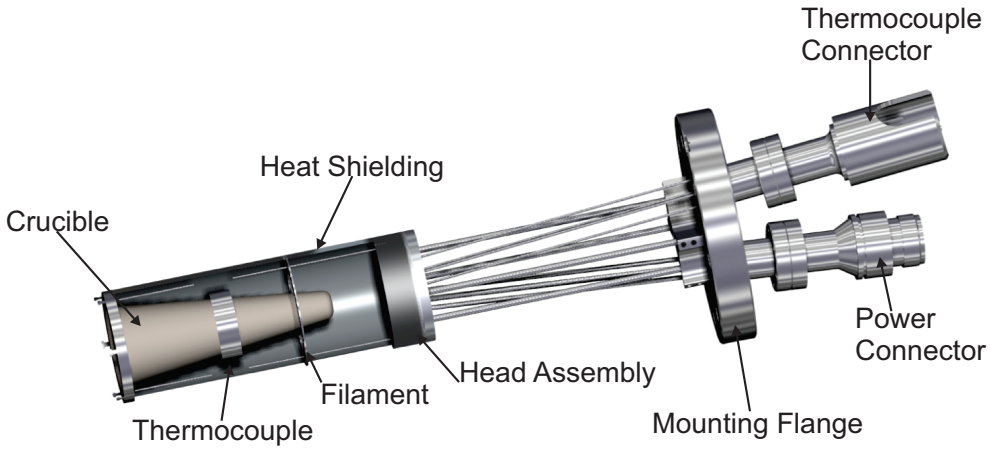

Figure 3.1: Diagram of a typical effusion cell showing internal construction of crucible, heating wire, thermocouple and heat shields. Figure from Veeco Instruments Inc.

Effusion cells are simple in premise, involving the heating of source material by a resistive element that causes the material to sublimate or evaporate into the gas phase with some kinetic energy outward from the cell. It is assumed that within the cell the condensed (solid/liquid) phase and the vapour phase are in equilibrium. The behaviour of the cell is then well understood, following the form of Eq. 3.2.

$$f = f_0 \exp\left(\frac{m_1}{m_2}\left(1 - \frac{m_1}{T}\right)\right), \tag{3.2}$$

where the delivered flux from the cell f is dependent on two characteristic temperatures m_1 and m_2, the temperature of the cell T (read by a thermocouple) and some constant scaling factor f_0. There are 2 characteristic temperatures due to 2 different thermodynamic equilibrium processes. Firstly the evaporation or sublimation of the source material into the gas phase and second the egress of the gas phase through the aperture of the cell. The cells used here generally have wide openings and so the process is dominated by only the evaporation or sublimation of material. It is generally convenient to consider $\ln(f)$ in which case a linear fit may be used to extract a good calibration of the cell as shown in Appendix A.

In a perfect example of epitaxial growth one would like to achieve a full monolayer of deposition onto the substrate material before overgrowing with the next layer, a so called Frank-van der Merwe growth mode. Unfortunately, this is not always the case and other growth modes may also occur, as outlined in Fig. 3.2. In simple terms the mode in which a film grows depends upon the chemical potential of the deposited film, a thorough account of this is given in Ref. [41]. It is possible to distinguish between these growth modes *in-situ* using reflection high-energy electron diffraction (RHEED), and is discussed later.

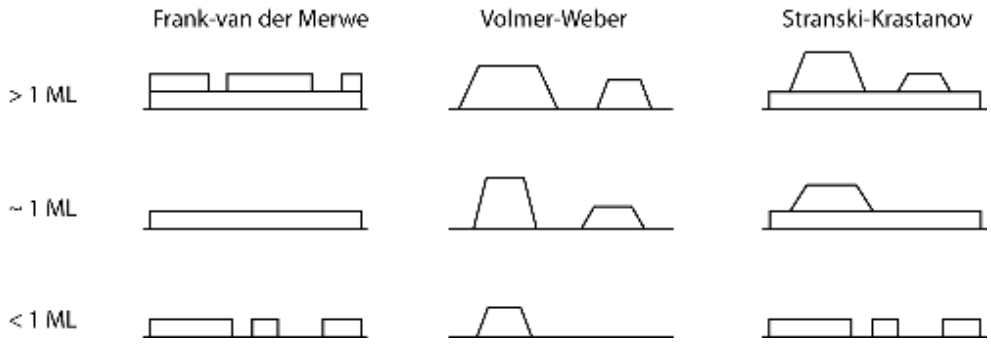

Figure 3.2: Growth modes of thin films as a function of layer thickness. Left: Frank-van der Merwe, layer-by-layer growth. Centre: Volmer-Weber growth, 3D islands. Right: Stranski-Krastanov, a wetting layer followed by island growth. Figure from Ref. [42].

3.1.2 Design of MBE System

The MBE system used for this thesis, shown in Fig. 3.3, is made up of 3 chambers: growth chamber, preparation chamber and the load lock. The load lock is used for the loading of substrates and unloading of grown films. It can hold 4 samples at a given time of up to 2" diameter on Riber style holders. For the majority of thin films grown in this thesis the samples were mounted on 1/4 wafer holders [Fig. 3.4(a)], which provides an adequate size of film for our measurements. Some samples were mounted using a method of Indium soldering on blank holders [Fig. 3.4(b)]. The load lock is pumped by an Edwards nEXT 400D turbomolecular pump and associated scroll backing pump. A 1 kW heating lamp is installed to bake the chamber after substrate loading and 2 of the sample stages are capable of independently heating samples up to ∼800°C. After pumping down and baking the chamber for 8 hours a typical vacuum of $\sim 3 \times 10^{-9}$ Torr is reached. Further, the load lock has a second stage which may be configured either for use as an *in-situ* electrical probe by means of a co-linear four point probe or as an additional load lock used to interface with a vacuum suitcase. This vacuum suitcase has been trialled in collaboration with beamline I05 at Diamond Light Source and can be used to transfer grown films for

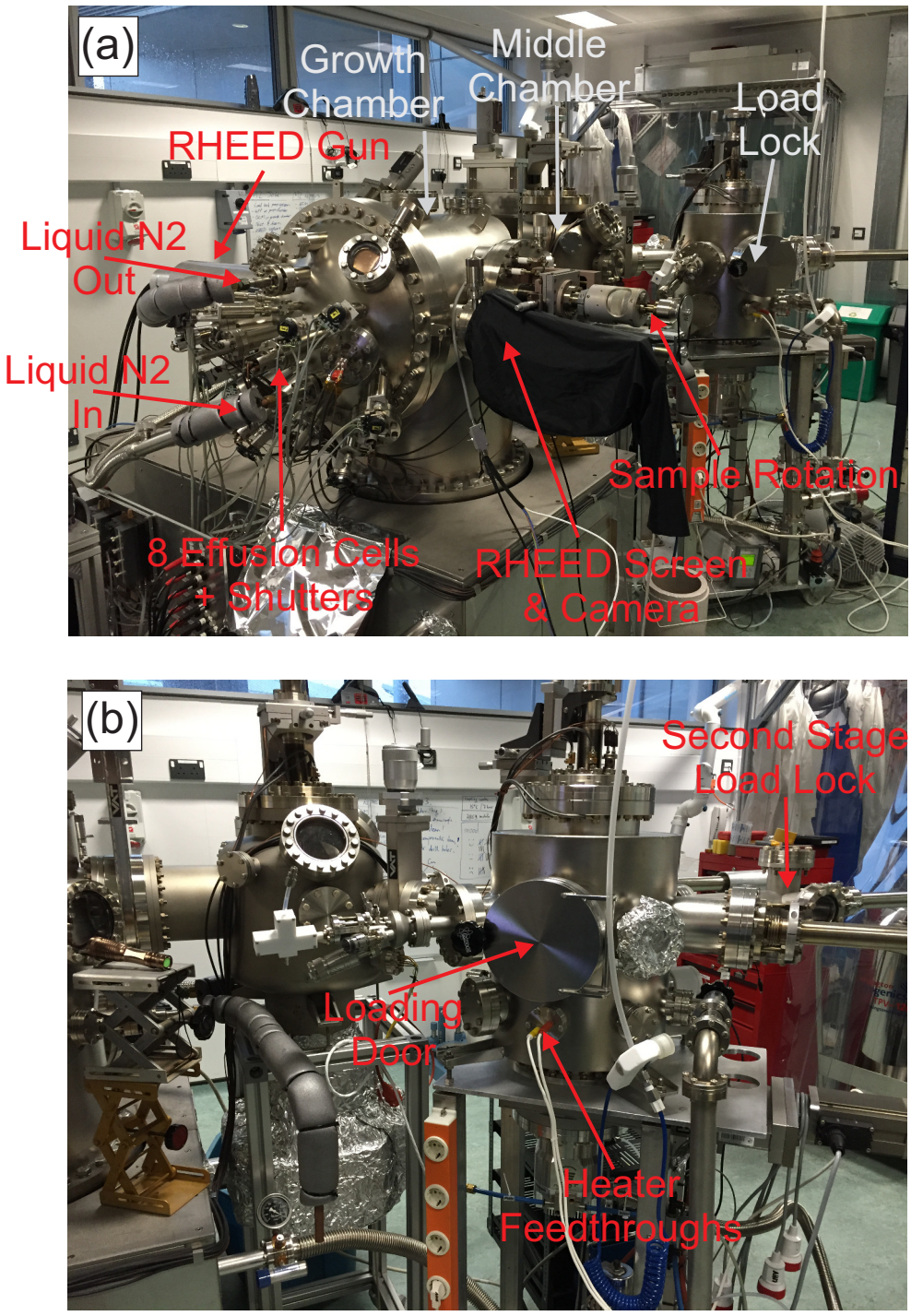

Figure 3.3: Photographs of the MBE system used to grow films. (a) Growth chamber of the MBE with key parts labelled. Note: The residual gas analyser is removed for repair in this image. (b) Load lock and preparation chamber. The second stage load lock (explained in text) is labelled.

beamline experiments whilst maintaining UHV conditions to protect the surface.

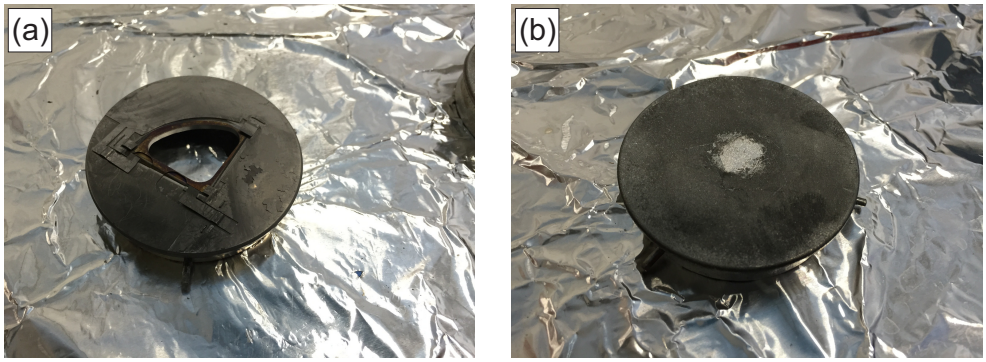

Figure 3.4: Types of sample holders used for MBE growth. (a) 1/4 of 2" wafer holder. Most commonly used in this thesis, holds 1/4 sized samples of standard semiconductor 2" wafers. (b) Blank holder for Indium soldering. Used for smaller or oddly shaped samples.

The preparation chamber has capacity for 4 samples, held in the same manner as the load lock. It is pumped with an ion pump and typically reaches a base pressure of $\sim 8 \times 10^{-11}$ Torr. Due to the chamber being pumped only with an ion pump it is unsuitable for the operation of evaporation sources with high vapour pressures. The chamber contains a UHV scanning tunnelling microscope, which is presently unused and is an expansion step for the machine. Presently this chamber mainly acts as a buffer between the load lock and growth chamber to ensure the purest possible environment is maintained in the growth chamber.

The growth chamber itself is pumped through a variety of mechanisms to accommodate the high vapour pressures produced from elemental sources. The main pump is a Leybold magnetic levitation turbomolecular pump which has a documented pumping rate of 1500 l/s for nitrogen gas. This pump is then backed by a smaller Pfeiffer mechanical turbo pump and finally the low vacuum scroll pump. The chamber is simultaneously pumped by a Gamma Vacuum ion pump and a cryo-pumping effect from the liquid nitrogen shroud. This cryo-shroud gives both a pumping effect (by removing kinetic energy from free gas molecules) and also works to ensure ther-

mal stability of the cells. For instance it is possible in this machine to have a cell running at 1200°C next to a cell at 50°C with very high thermal stability. The final pumping method available is a titanium sublimation pump. This works by means of a titanium filament that coats the walls of the pump with Ti, which reacts with contaminants to remove them from the rest gas. This is particularly effective with water. The pump is only used when necessary and usually is needed when outgassing cells or when using new source material that may contain some water. The chamber contains 8 effusion cells that may be reconfigured depending on the growth system of interest. In general the sources are always configured with the 4 base elements of the chalcogenide TIs: Bi, Sb, Se, and Te, plus a selection of transition-metal dopants: Mn, Fe, Cr and rare-earth dopants: Dy, Ho. It is worth noting at this point that Se is evaporated from a special hot-lip cracker effusion cell, supplied by Createc. The hot-lip is usually set to be 100°C higher than the cell temperature and serves to crack Se_4 down to Se and Se_2, as required for the epitaxial growth. Source fluxes are monitored and calibrated at the start and end of growth using an *in-situ* beam-flux monitor which monitors the molecular flux arriving at the substrate position. This is used to set the required flux ratio between elemental sources (e.g. for doping studies) as well as confirm a nominal growth rate. The substrate is held on a continuously rotating stage that may be filament heated up to 850°C. Growth may be monitored in real time by RHEED. The chamber is equipped with a mass spectrometer (SRS RGA300) to measure the rest gas of the system. This is used to identify sources of possible contamination in the vacuum and also to leak test the system using He after any chamber opening.

3.1.3 Calibration of Elemental Sources

To grow high quality thin films in a repeatable and systematic manner it is important to have close control of the deposition conditions. Although the cells are continuously

monitored and controlled by a thermocouple plus Eurotherm controller, as the cell is depleted of material the flux output from the cell will decrease for a constant temperature. This effect occurs over weeks rather than hours and so to ensure samples may be grown under controlled conditions over time the sources are regularly calibrated (weekly) by an automatic script (given in Appendix A). Example calibration curves for two elemental sources (Bi and Te in this case) is shown in Fig. 3.5. It can be seen that the curve is well characterised by a linear fit to a logarithmic plot. Records are kept of the fit parameters for each source so that a quick determination of the source temperature for a desired flux may be made. In this thesis dopant levels are determined with reference to the dopant to Bi flux ratio and samples are grown with a typically 10 times higher (Te/Se) flux pressure compared with Bi; the reasons for this will be elucidated later. The fluxes are measured using a beam flux monitor, essentially a nude ion gauge, and it should be noted that for true quantitative measurements of beam flux the relative ionisation efficiencies of the different elements (see p. 78 of Ref. [43]) are required. This is not required here as only a repeatable determination of relative fluxes is required.

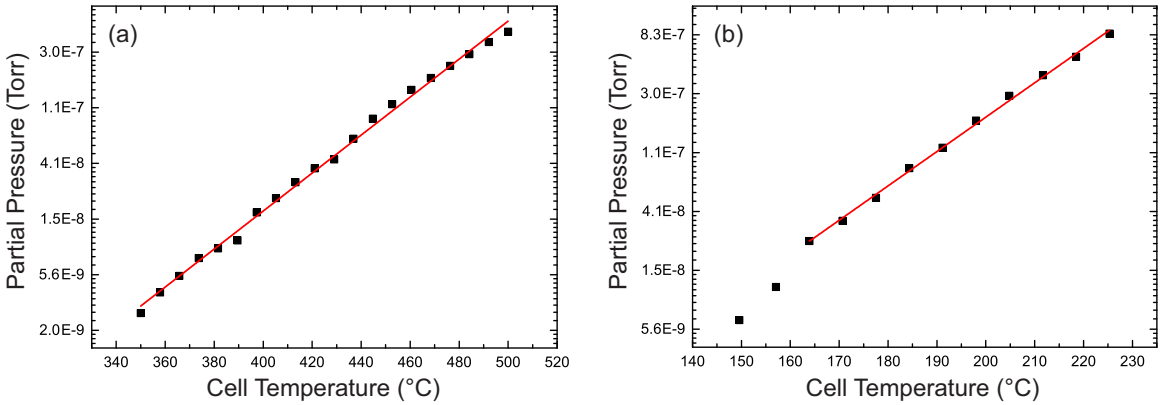

Figure 3.5: Calibration of effusion sources for (a) Bi and (b) Te by an automated script. The full linear fits for all cells are given in Appendix A.

3.1.4 Substrate Preparation Methods

Perhaps the most important aspect of MBE growth of thin films is substrate preparation, without correct preparation techniques no worthwhile film may be grown. It is therefore necessary to cover some technical details of the preparation of substrate materials.

The vast majority of thin films grown in this thesis used sapphire (0001) as a substrate material. These substrates are bought as pre-cut and epi-ready 2" diameter wafers from the manufacturers (CrysTec, Universitywafer, MTI Crystal) and in theory should be ready to grow by MBE as received. However, in practice this has proved inconsistent and so a wet chemical process is used to ensure that the substrates are free from organic contaminants introduced through handling or shipping. These organic contaminants are removed by following the steps outlined in Appendix B. All solvents used are of the highest available purity, typically labelled as 'semiconductor grade'. The samples are then baked in the load lock in UHV conditions up to $\sim$250°C for around 8 hours (overnight).

This method of preparing samples has empirically been shown to be successful for preparing the surface of nearly all samples presented here. It has been previously reported [44] that sapphire substrates may be etched with a mixture of H_2O_2 and NH_4OH before annealing in oxygen. This was attempted, but no improvement was seen for films grown on substrates prepared in this way.

3.1.5 In-Situ Probes

There are three main *in-situ* probes employed in the MBE system used for this thesis: beam flux monitoring, RHEED and residual gas analysis (RGA). Since beam flux monitoring has already been covered, here there is a brief account of the usage of RHEED and RGA in relation to thin film growth.

RHEED is an electron diffraction method used to gain qualitative and quantitative

information about the surface of a growing thin film in real time. From diffraction images one may obtain information regarding surface cleanliness, reconstructions, in-plane lattice constants, smoothness, growth mode and growth rate. An exceptionally detailed description of the relevant theory around RHEED is given in Ref. [45]. RHEED operates by the thermal emission of electrons from a hot filament before

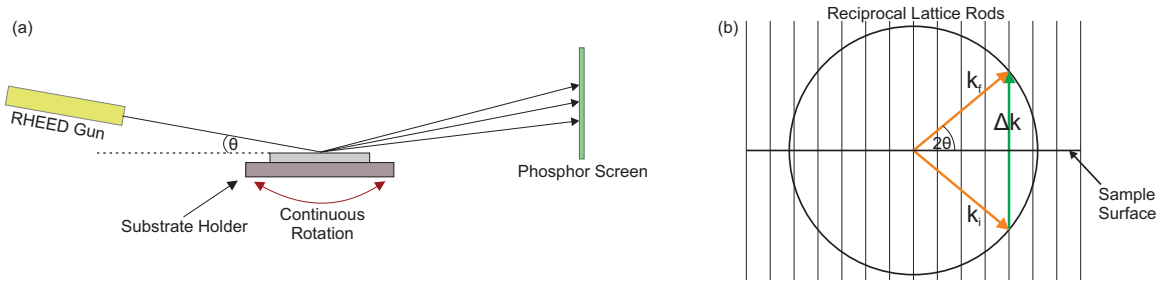

Figure 3.6: (a) Schematic geometry of the RHEED system used in the MBE. Incident electrons from the RHEED source are diffracted by the sample and are detected on the phosphor screen. For our system $\theta \approx 1°$. (b) Ewald sphere construction of diffraction conditions. Diffraction occurs at points where the Ewald sphere (radius defined by energy conservation) intersects with the reciprocal lattice. The scattering vector is defined as $\Delta k = k_f - k_i$.

acceleration up to a single energy (30 keV here) by an accelerating field and are then focussed by a magnetic lens. These high energy electrons then impinge on the sample at grazing incidence to the surface ($\sim$1°) after which the diffracted electrons impact on a phosphor coated screen where the pattern is then either directly observed or recorded with a camera. A schematic of the geometry used for RHEED is shown in Fig. 3.6(a). The usage of grazing incidence combined with the highly interacting nature of electrons as a diffraction probe means that the incident electrons penetrate only the first few monolayers of the film surface. So from the perspective of diffracting electrons the film surface represents a two-dimensional grating since the lattice spacing in the direction of the surface normal is effectively zero. The observed diffraction by RHEED can be understood using the Ewald sphere construction (explained fully in Ref. [46]), in which the periodic 2D surface is considered as a series of lattice rods

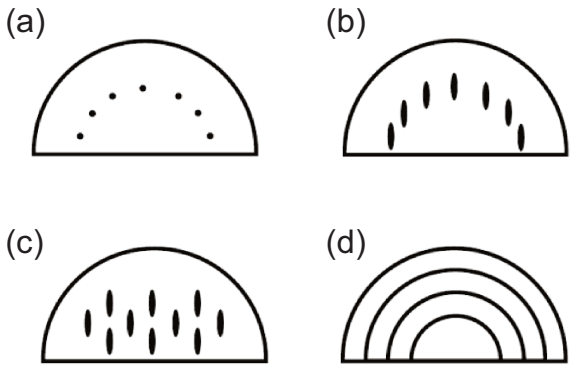

Figure 3.7: Explanation of commonly observed RHEED patterns: (a) An ideal smooth surface intersecting Ewald sphere and single points. (b) A real smooth surface intersecting along a finite length. (c) Diffraction through 3D clusters (d) A polycrystalline or textured surface.

in reciprocal space, as shown in Fig. 3.6(b). In this construction, diffraction occurs wherever the Ewald sphere intersects with the reciprocal lattice rods (in real terms over some finite region). In RHEED (for 2D diffraction) streaks are observed as the diffraction pattern due to the finite intersection of the Ewald sphere with the reciprocal lattice rods and because the Ewald sphere diameter is significantly larger than the spacing of these rods due to the high energy diffraction.

Qualitative information about the film morphology may be gained from a brief glance at the RHEED pattern, making it a highly valuable tool for quick understanding of the growth process as it progresses. A simplified guide to possible RHEED patterns observed is shown in Fig. 3.7. In short for a perfect 2D single crystal we see stripes as expected. If the surface is dominated by 3D islands (see Volmer-Weber growth) then the assumption of a 2D periodic lattice grating is no longer valid and instead diffraction spots are seen, i.e., reciprocal lattice vectors are now defined in all 3 directions. If the film is growing in a polycrystalline way then the lattice rods get smeared out across the screen and are instead seen as rings due to the more isotropic diffraction.

Quantitative information about the film structure in the sample plane can be obtained by the spacing of the diffraction lines on the phosphor screen. The spacing of the RHEED streaks (D) can be related to the lattice spacing (d) by Eq. 3.3.

$$D = \frac{\lambda L}{d} \tag{3.3}$$

Where λ is the wavelength of incoming electrons and L the distance from the sample to the screen. This equation assumes grazing incidence diffraction, where $\sin\theta \approx \theta$. In practice such quantitative information about the lattice constants of grown films is not obtained by RHEED in this thesis and instead x-ray diffraction is generally used.

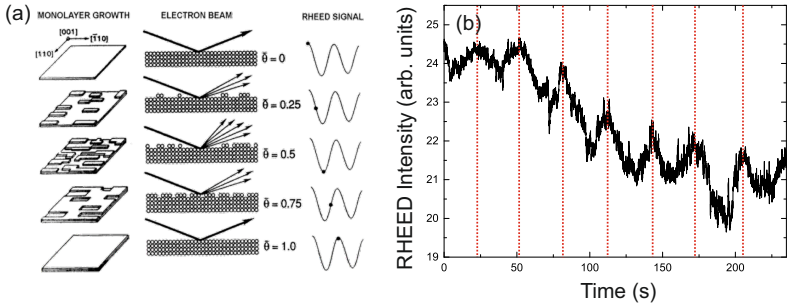

Figure 3.8: (a) Model of the origin of RHEED oscillations based on interpretation of surface filling. Minimum in RHEED intensity corresponds to a maximum in film roughness. Figure from Ref. [47]. (b) Measured RHEED oscillations for a thin film of Bi_2Te_3 showing a growth rate of ∼2.14 quintuple layers per minute. The red dashed lines are a guide to the eye, indicating the completion of each full quintuple layer.

Real-time information about the growth rate can be gained by recording the intensity of the specular reflection from RHEED as a function of time. Such RHEED oscillations occur as a function of the filling factor of the surface layer, as shown in

Fig. 3.8(a). It may be considered that a maximum in reflection will occur for the smoothest surface (fully filled layer) and a minimum for maximum surface roughness (50% filled layer). By measuring these oscillations as a function of time a figure in terms of monolayers (or quintuple layers here) grown per unit time is obtained. If information about the lattice constants and film orientation is already known then this may be easily converted to a growth rate in nm/min. An example of RHEED oscillations obtained using the MBE is shown in Fig. 3.8(b). Experimental experience of the chalcogenide TIs has shown that prolonged exposure to RHEED has a significantly damaging effect on the structural quality of the grown film, visible to the eye as a dark line 'burned-in' to the sample surface. As such, RHEED oscillations are generally not used on these films and growth rate information is instead obtained *ex-situ* by x-ray reflectivity.

Measurement of the residual gas by quadrapole mass spectrometry gives useful information about the rest gas of the system and is predominantly used to identify sources of contamination. This is not the only use of the system and when properly configured it can also be used for desorption studies from thin films and for characterisation of the elemental characteristics of effusion sources e.g., whether it produces Se, Se_2, Se_3 or Se_4 and in what proportions. In this work the RGA has mainly been used to analyse contaminants in the rest gas and to perform leak tests on the system by looking for He leaks through the metal seals as He gas is sprayed around the external walls. An example spectrum observed with our RGA is shown in Fig. 3.9.

3.2 Structural Characterisation

Thin films grown by MBE are analysed using a variety of lab based tools to study their growth characteristics. In general the results from these methods are parameterised in some manner that gives a measure of the quality of the growth and information

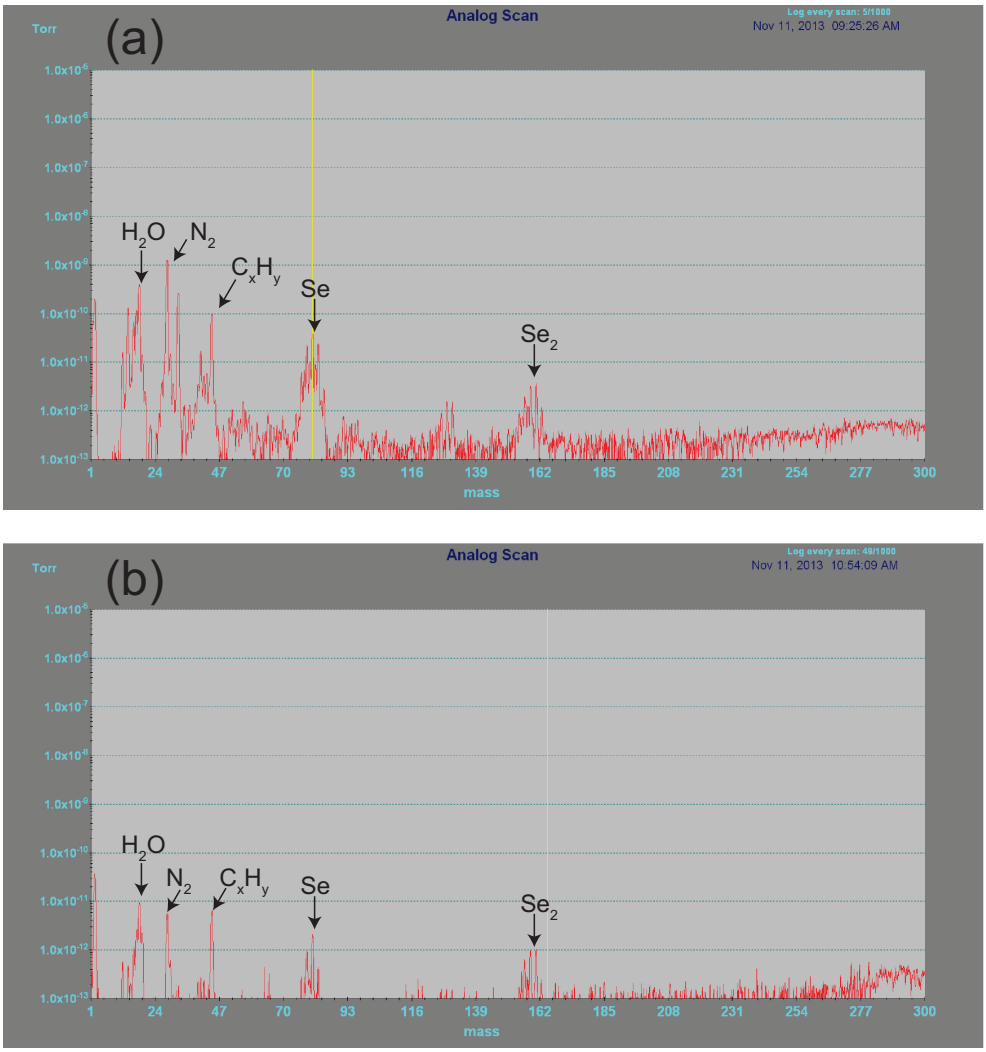

Figure 3.9: RGA scans of the MBE growth chamber for (a) Baked chamber without liquid nitrogen cooling. (b) Baked chamber with liquid nitrogen cooling. The likely compounds contributing to the residual gas are labelled.

gained is fed back into the growth system for the next round of films. In this thesis, in general, the end result of a long iterative process will be shown for a variety of growth systems. One should note that, as a rule of thumb, for each 'good' film grown upwards of 20 'bad' films may be required before hitting the desired parameters. Given the iterative nature of this growth technique, it is essential to have fast feedback from characterisation tools to improve films before they are used for detailed studies, for example, by synchrotron radiation.

3.2.1 X-Ray Studies

X-ray studies: namely x-ray diffraction (XRD), x-ray reflectivity (XRR) and rocking curves are the main methods employed to characterise the quality of thin film growth. XRD probes the crystal structure and when combined with appropriate modelling and/or refinement can extract the crystalline phase, stoichiometry and lattice constants. XRR is an interference based technique where, for a reasonably flat film, periodic oscillations are observed which scale inversely with the film's thickness. With appropriate modelling XRR measurements give detailed and accurate information about the film thickness, layer structure, interfacial mixing and roughness. Rocking curves are measured by 'rocking' the sample around a defined diffraction peak. The full width at half maximum (FWHM) of the rocking curve peak shows broadening due to a variety of effects, e.g., sample curvature, site dislocations, defect density and strain. A detailed understanding and modelling of these effects is not strictly required, but simply to note that a narrow rocking curve implies a better sample.

A thorough theoretical overview of these tools is somewhat unnecessary here given that x-ray diffraction theory is covered in the vast majority of undergraduate level physics texts, a particularly good overview of x-ray as well as neutron diffraction

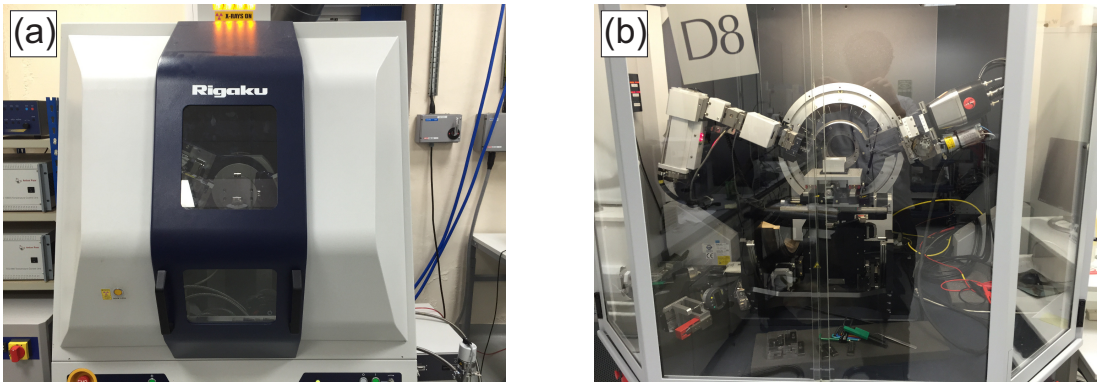

Figure 3.10: Photographs of x-ray diffraction tools used in this thesis: (a) Rigaku Smartlab at ISIS Neutron & Muon Source, (b) Bruker D8 at Diamond Light Source.

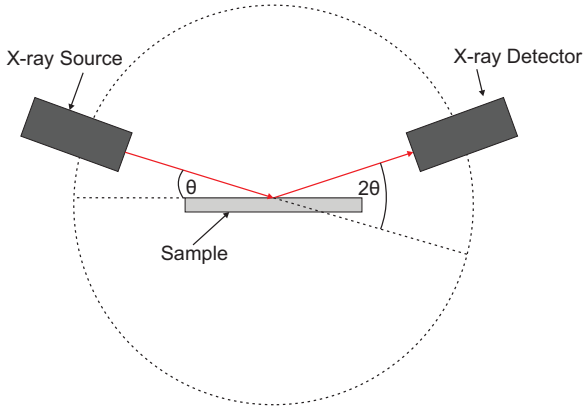

Figure 3.11: Bragg-Brentano geometry used for x-ray studies in this thesis. The sample is kept fixed with the source and detector moving symmetrically about it.

methods is given by Ref. [46]. Two x-ray diffractometers have been used in the course of this thesis and are of slightly different designs. One is a Rigaku Smartlab diffractometer [Fig. 3.10(a)] using a rotating Cu anode, producing Cu-K_{α_1} radiation at 45 keV and 200 mA. The second used is a Bruker D8 diffractometer [Fig. 3.10(b)] which also used a Cu anode, but operating at lower generator settings of 40 keV and 40 mA. Both of these machines use the standard Bragg-Brentano geometry with a fixed sample and movable source and detector, as shown in Fig. 3.11.

XRR measurements rely on oscillations about the expected Fresnel reflectivity. These oscillations provide information about inhomogeneities perpendicular to the sample surface. In practice XRR curves are best understood by building an appropriate model of the system and using an iterative regression technique to refine the

simulated pattern to the measured one. In this thesis all XRR measurements were modelled using the package GenX [48] and details of the relevant fitted parameters are given in the following chapters. Nonetheless it is useful to have an appreciation of the generally important features of XRR scans and the physical properties that drive them. Figure 3.12 serves as a good explanation of these features. In general, we are most interested in the period of oscillations which depend on the thickness of the film, the critical angle and oscillation amplitude, which both depend on film/-substrate density, and of the decay rate as a function of angle, which depends on the surface and interface roughness. For a more thorough explanation of these effects Ref. [49] is highly recommended, from which this figure was taken.

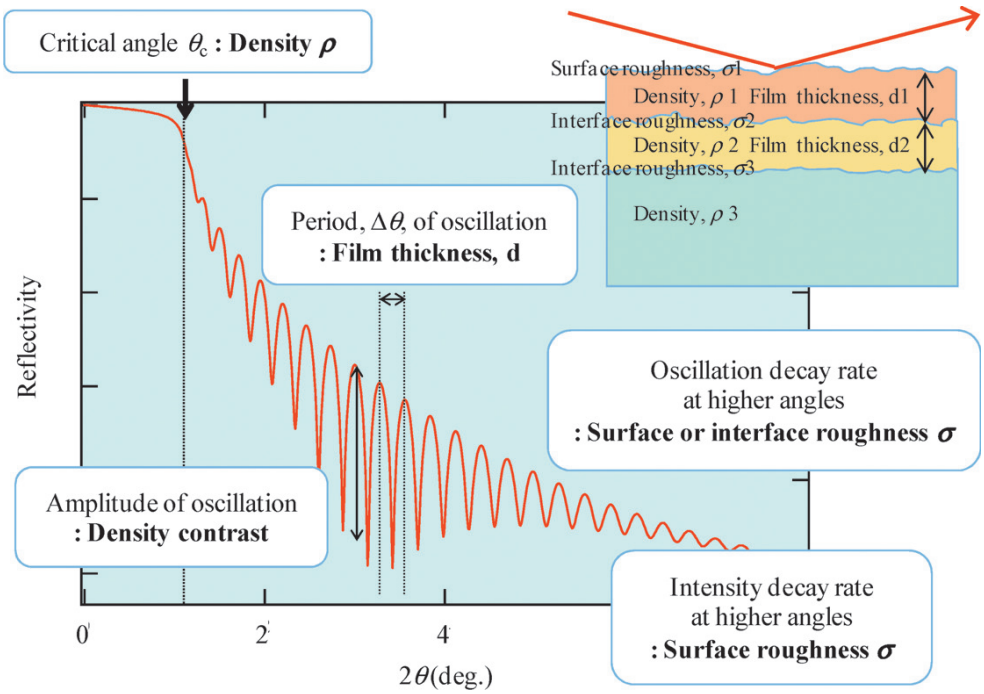

Figure 3.12: General features of XRR explained with reference to their physical origins. Figure from Ref. [49] .

XRD measurements are a staple of crystallography and condensed matter physics, providing clear information regarding the crystallographic properties of the probed matter. The diffraction conditions are defined by Bragg's law ($n\lambda = 2d\sin\theta$) and in

the case of the rhombohedral symmetry class of the chalcogenide TIs ($R\bar{3}m$) the d spacing of Bragg's law is related to the lattice parameters by Eq. 3.4.

$$\frac{1}{d^2} = \frac{4}{3}\left(\frac{h^2 + hk + k^2}{a^2} + \frac{l^2}{c^2}\right), \tag{3.4}$$

where h,k and l are the Miller indices of the relevant reflection and a and c are the crystal axes (note: $|a| = |b|$ for this space group). XRD measurements of thin films in this thesis are measured for a purely out of plane diffraction geometry. For these thin films this means measurements along the $00l$ set of lattice planes and since (by Eq. 3.4) l and c are linearly independent from h, k and a, such measurements contain only information about c and not a. It is possible to extract the desired lattice constants by a linear fit of peak positions to Eq. 3.4 or by Rietveld refinement in an appropriate software. Both methods have been used, and for Rietveld refinement the software Fullprof has been used in combination with crystal structure files from the inorganic crystal structure database (ICSD).

3.2.2 Atomic Force Microscopy

Atomic force microscopy (AFM) is a scanning probe microscopy tool utilising a cantilever tip to measure the vertical force between the probe and the sample as it is scanned across the sample laterally. This then allows the direct mapping of the sample's surface topology. In this thesis AFM scans were acquired using a Veeco Multimode V AFM (Fig. 3.13) which operated in tapping mode. In tapping mode the AFM tip makes intermittent contact with the surface rather than utilising the small attractive forces in non-contact mode. Although tapping mode is semi-destructive it was found to yield better results for these samples than non-contact mode. AFM scans are shown in the relevant later chapters and are useful for understanding the growth mode and morphology of grown films. It is also possible to extract out sta-

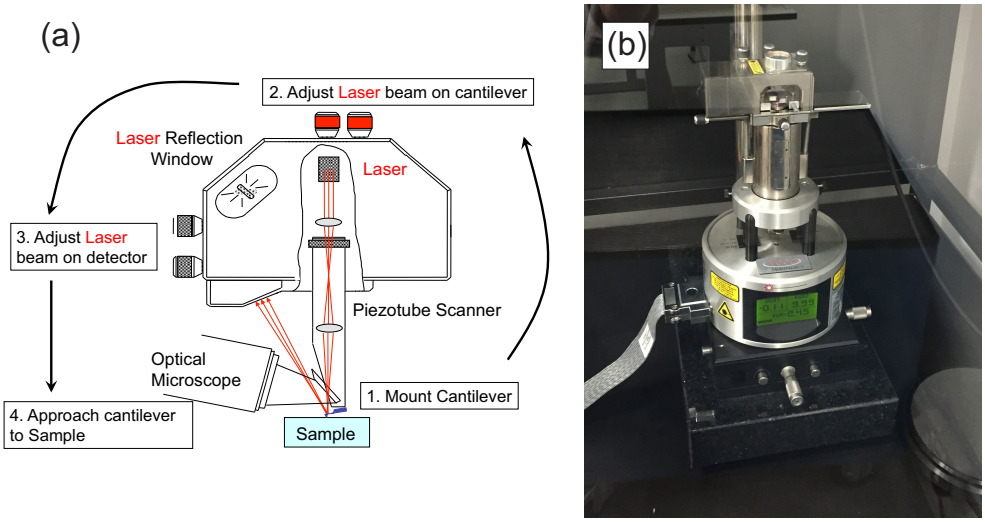

Figure 3.13: (a) Schematic diagram of the AFM used in this thesis. Steps for aligning the AFM for measurement are shown. Figure from Veeco Instruments Inc. (b) The Veeco Multimode V AFM used for studies in this thesis.

tistical quantities, such as surface roughness, to further parameterise the quality of film growth. The open source software Gwyddion has been used to manipulate the images and extract parameters presented here [50].

3.2.3 Doping Concentration Determination

Although XRD provides an excellent method for the determination of crystallographic phase and stoichiometry, it provides limited information regarding the low level doping of the grown crystals with magnetic elements. Multiple methods have been used during this thesis to ascertain the doping concentrations of films and each have advantages and drawbacks.

The simplest method of determination that is used for all films is beam flux monitoring (BFM, explained earlier). To determine a nominal doping concentration a measurement of beam flux is taken with respect to the flux of the group V element (usually Bi) for co-evaporation. A simple approximation would say that, for substitutional doping on the group V site, the doping concentration x in, e.g., $TM_xBi_{2-x}Te_3$

(where TM is our transition metal dopant) scales proportionally with the TM:Bi flux ratio measured by the beam flux monitor. This approach makes some key assumptions that are not necessarily true:

1. The doping mode is purely substitutional.
2. The sticking factor is the same for the dopant as the group V element.
3. The relative ionisation efficiencies of the transition metal and group V element are the same.

Although these assumptions are not fully justified this method does provide a reliable way of systematically growing samples in a reproducible way. For example a sample with $x = 0.12$ (determined by BFM) may be grown and although x is not truly 0.12, the same sample growth may later be repeated for an identical recorded flux ratio and the doping concentration would be the same.

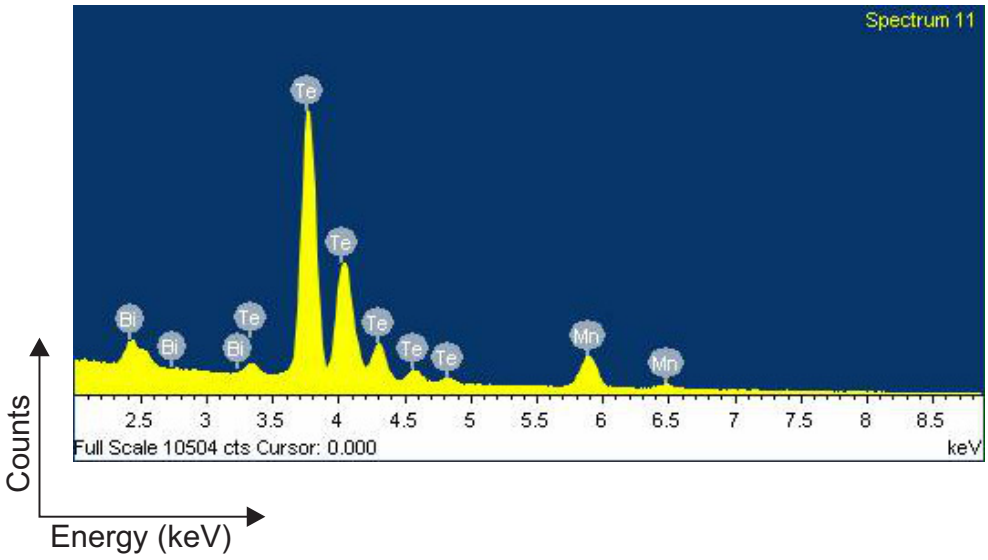

Figure 3.14: EDS data measured for a Mn-doped Bi_2Te_3 bulk crystal.

Two quantitative *ex-situ* methods have been used for the determination of doping concentrations: Energy-disperse x-ray spectroscopy (EDS/EDX, built into a scanning

electron microscope) and Rutherford back-scattering spectrometry (RBS). The EDS system (Oxford Instruments) used in this thesis is fitted within an SEM and the data are measured and analysed in the software Aztec. Although the SEM itself has too low a resolution to directly image the thin films grown in the same manner as AFM, by averaging over the observed film area quantitative information about elemental composition can be obtained by EDS. An atom at rest will contain a certain number of fully filled core shells and some (partially) filled outer shells. In an EDS measurement, a core-level electron is ejected from an inner shell by an externally applied excitation from the incoming electron beam. An electron from a higher energy orbital will then decay into this hole state and in the process emit an x-ray with energy equal to the change in energy between orbitals. The energy of this x-ray is characteristic of the particular electronic configuration and thus the specific element probed. It is necessary to irradiate the sample with electrons with energy greater than the binding energy of the core-level for the element we wish to probe. Typically the system used here is set to 20 keV, which is more than sufficient to probe the elements of interest. An example spectrum of typical measured data is shown in Fig. 3.14. The Aztec software will automatically quantify measured spectra in terms of the atomic percentages of elements specified. The software itself does not deliver an error on its measurement and an estimation of this is not straightforward. By measuring the sample multiple times and through comparison with other techniques (e.g., RBS) this method is found to have a typical error of 5-10%, with the actual error varying depending on the doping concentration and hence peak intensity. Quantification can also be made more challenging by overlapping peaks from various elements. For thin films measured here there is a significant overlap between the Se and Al (from the sapphire substrate) peaks. This effect is mitigated by allowing the software to independently fit higher energy, non-overlapping, peaks.

RBS works in a fundamentally different way to EDS and has some key advan-

tages and drawbacks. In an RBS measurement, high-energy (∼2 MeV) He^{2+} ions are directed at the sample and back-scatter from the nuclei as per Rutherford's original and well known experiment. The energy and outgoing angle of the back-scattered He^{2+} ions are recorded by an energy sensitive detector. For straightforward 2-body elastic collisions a basic kinematic scattering model may be used to determine, from the energy and outgoing angle, the scattering cross-section of the nuclei that the ion interacted with. This scattering cross-section is again a unique property of the particular nucleus and allows unambiguous determination of the element being scattered from. Due to the nature of 2-body elastic scattering, this technique is only applicable for the measurement of elements significantly heavier than He, fortunately that is very much the case for our samples. By simulation of the measured data an accurate determination of elemental quantities as well as their varying as a function of depth can be achieved without reference to calibration standards. An overview of this technique is given in Ref. [51]. All RBS measurements were performed by A. Pushp and A. J. Kellock at IBM Almaden Research Center, San José.

Judging by the data acquired using these techniques, RBS offers the best quality and most reliable determination of elemental composition. However, it is a more in-depth experiment relying on collaborative efforts and so is unsuitable for everyday characterisation of grown films. *In-situ* beam flux monitoring gives immediate information, but with the disadvantage of measuring the incident flux rather than the quantities truly incorporated into the film. EDS does measure the film as-grown but suffers from overlapping peaks and a lower quality of fit than RBS. In general, beam-flux and EDS are used to characterise films as they are grown and RBS is used on a smaller subset of the samples on which a publication is being written. In the end all these techniques do agree with some linear offset between them. It is reasonable to assume that once RBS has determined the composition of a film grown with a certain flux ratio, then future films grown at the same ratio will have the same composition

as previously measured.

3.3 Magnetic Properties

Since the aim of doping topological insulators with various transition metal elements is to induce long-range magnetic order and therefore an opening of a surface band gap, detailed investigation of the magnetic properties of grown films forms a core part of this work. Two main methods are employed for the magnetic characterisation of these samples: superconducting quantum interference device (SQUID) magnetometry and x-ray magnetic circular dichroism (XMCD). Chapter 6 makes use of polarised neutron reflectometry (PNR) to gain depth resolved magnetic order information. Here, an overview will be given of the application of each of these techniques to the present work.

3.3.1 SQUID Magnetometry

SQUID magnetometers are lab-based tools capable of detecting exceptionally small magnetic moments within the pick-up loop. The physical basis on which these devices are built is described in Ref. [52]. In short, a loop of superconducting material is designed with a deliberate 'weak-link', forming a Josephson junction. This ring then operates as a highly sensitive interferometer where a persistent current will be generated proportional to any magnetic moment threaded through the loop.

In this thesis SQUID studies were carried out either in a Quantum Design MPMS 3, SQUID VSM (Diamond Light Source, UK) or in a Quantum Design MPMS XL (ISIS Neutron and Muon Source, UK). Both devices used are capable of applying a 7 T field to the sample and operating from room temperature down to 1.5 K. Thin film samples are typically mounted either on a quartz rod (for measurements in-plane) or by wedging the sample into a cut in a drinking straw (for out of plane

measurements). After measurement all data are processed to remove the diamagnetic contribution from the substrate material by a linear fit to the high field data. The instrument measures data in 'emu' magnetic units; for comparison with literature and theory these should be converted to μ_{B}/ion.

The first step in this conversion is an accurate determination of the magnetic dopant concentration per formula unit. As mentioned earlier this may be done by beam-flux monitoring, EDS, or RBS; with RBS giving the smallest error bar. Next, it is necessary to know the volume of the measured film without the substrate contribution. There are multiple ways to achieve this, but the simplest method that has been successfully applied is as follows. Firstly, the film thickness must be known from XRR studies. The samples mass (m) is measured using a precision mass balance and it is assumed that all of the measured mass is from the substrate. The thickness of the substrate (t) is quoted by the manufacturer to $\pm$ 1μm and, using given documented density values for sapphire ($\rho_{\mathrm{Sapph.}}$), it's cross-sectional area (A) can then be calculated by Eq. 3.5.

$$A = \frac{m}{\rho_{\mathrm{Sapph.}} t}. \tag{3.5}$$

Combined with the thickness measured by XRR this now gives the film volume. From here it is possible to calculate the number of formula units in this volume, from there the number of magnetic present and then use this to normalise the measured magnetisation appropriately. Equation 3.6 provides this conversion.

$$M\,[\mu_{\mathrm{B}}/\mathrm{Ion}] = M\,[\mathrm{emu}]\,\frac{m_{\mathrm{rel}}}{N_A \mu_{\mathrm{B}} \rho V d}, \tag{3.6}$$

where M is the magnetic moment (in different units), m_{rel} is the relative molecular mass of the film, d is the dopant concentration (in atomic %), N_A is Avagadro's number, μ_{B} the Bohr magneton (in emu), ρ the film density and V the film volume.

It is important during this conversion that consistent units are used.

Magnetic hysteresis loops (magnetisation vs. applied field) are useful for extracting critical parameters such as saturation magnetisation and coercive field. With reference to magnetism theory it is possible to infer from saturation magnetisation the likely valence state of the magnetic ion. Though this is an imperfect method as the measured magnetisation can be reduced by effects such as crystal field quenching. By measuring hysteresis both in-plane and out-of-plane for each sample, one may also determine the magnetic anisotropy of the sample. Temperature dependent measurements are used to determine the Curie temperature (T_C) either by fitting the measured data to the Curie-Weiss law or by looking for a minimum in the first derivative of magnetisation. The Curie-Weiss law is defined as:

$$\chi_m \propto \frac{1}{T - T_C}, \tag{3.7}$$

where χ_m is the magnetic susceptibility, T is temperature and T_C the Curie temperature marking the transition from a paramagnetic to ferromagnetic ground state. This is not the only way of extracting T_C, others include Arrot plots or examination of $1/\chi_m$ as a function of temperature. Methods for determination of T_C are discussed in Ref. [53].

3.3.2 X-ray Magnetic Circular Dichroism

XMCD is an element specific probe of magnetic order utilising synchrotron radiation at energies tunable to the element probed. When combined with appropriate simulations and atomic multiplet theory it can provide highly detailed information about the electronic character of the magnetic ground state. This tool is therefore well suited for the investigation of magnetic order in materials with unusual band structures. Many reviews already exist giving a thorough overview of the subject [54, 55, 56, 57]

and I will present the key elements required to understand this technique and its application to doped TIs.

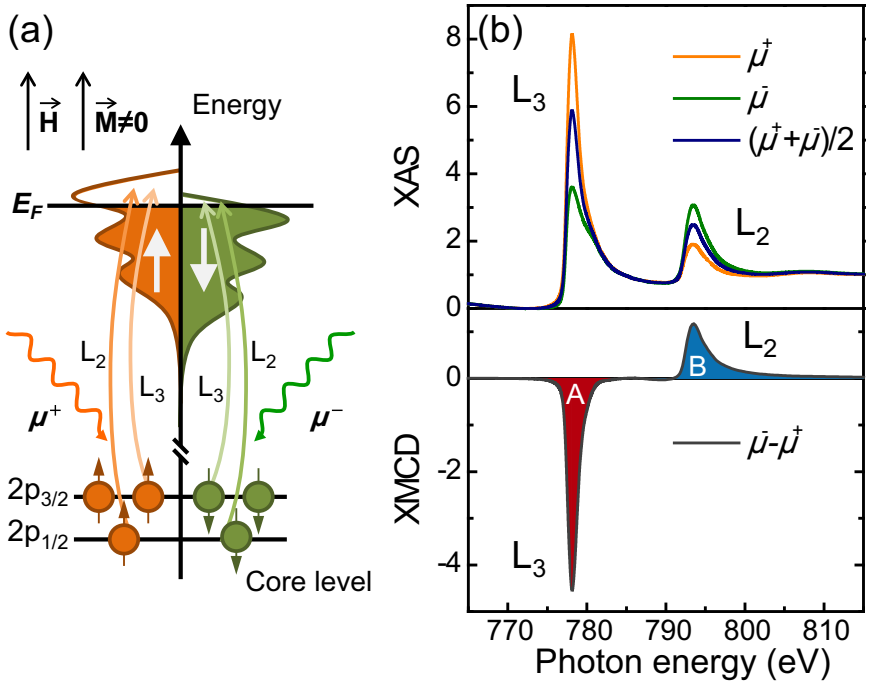

Figure 3.15: (a) Two-step model of XMCD for the resonant excitation of a single electron in a magnetic material. First a circularly polarised photon excites a spin polarised electron from the $2p$ level, which is split by spin-orbit coupling. For circularly polarised light it is the case that at $2p_{3/2}$ level (L_3 edge) a photon with positive helicity will excite more spin-up than spin-down electrons. For the $2p_{1/2}$ level (L_2) edge a photon with positive helicity will excite more spin-down than spin-up electrons. The second step is for these excited electrons to find a hole state in the $3d$ band. If the $3d$ electrons are spin polarised then selection rules in the transition create a difference between the spin states observable as XMCD. (b) XAS of the Co $L_{2,3}$ edge for right ($\mu+$) and left ($\mu-$) circularly polarised light. Below is the difference spectrum (the XMCD) resulting from polarisation of the $3d$ band. Figure from Ref. [57].

Within this context dichroism refers to the preferential absorption of light by a material based on the polarisation of the light. This varying absorption is a result of broken symmetry within the material (time-reversal symmetry in this case) and may therefore be used as a probe of those broken symmetries. XMCD is simply taken as the difference of two x-ray absorption spectra (XAS) for opposing helicities of incident

light. As such it provides us with all the information of XAS spectra (e.g., composition and valency) as well as a magnetic probe. A simplified picture of the physics behind XMCD is shown in Fig. 3.15(a). An incident circularly polarised photon will have a defined positive or negative helicity (μ^+ or μ^-). This photon will excite an electron from the spin-orbit split $2p$ core level up to the $3d$ band (for L edges). It is possible through spin-orbit coupling for angular momentum of the photon to be transferred to the spin of an excited electron. A positive helicity photon will excite primarily spin-up electrons from the $2p_{3/2}$ level and primarily spin-down from the $2p_{1/2}$ level. This fact demonstrates the change of sign for XMCD between the L_3 and L_2 edges; the inverse statement is true of negative helicity photons. Since spin-flips are forbidden in electric-dipole interactions then a spin-up excited electron must occupy a spin-up hole state in the $3d$ band. As such, if there is net polarisation in the $3d$-band (magnetic order) then there will be a difference in transition probabilities for each spin-state, observable as the circular dichroism [Fig. 3.15(b)].

In XMCD, similarly to XAS, there are two main detection mechanisms employed: total-electron yield (TEY) and fluorescence yield (FY). TEY directly detects the drain current from a probed sample through highly sensitive current amplifiers. This method is most effective for metallic samples and typically gives far higher signal to noise than FY. TEY is highly surface sensitive due to the relatively short electron escape depth. Therefore, for thin film samples careful protection of the surface against oxidation effects is necessary. This is achieved either by capping and then *in-situ* de-capping or by *in-situ* cleaving. In some instances this problem may be avoided totally by *in-situ* deposition of the film prior to measurement. FY relies on fluorescence of the sample proportional with the x-ray absorption, it is therefore more effective on some samples (which fluoresce highly) than others.

Much can be learned from the qualitative lineshape of XMCD by inspection. Of particular importance here is that metallic oxides of e.g. Mn, Cr, Fe generally have a

pronounced multiplet structure to their XAS or XMCD compared with the typically singlet structure of the metal. Such an effect is seen in thin film samples suffering from surface oxidation and indicates that further surface preparation is required. Quantitative information is extracted from XMCD either by the widely used 'sum rules' or by comparison of measured data with simulations using atomic multiplet theory. The sum-rules [58] allow a direct relation between the integrated XMCD spectrum and the ground state expectation value of the orbital magnetic moment. In this thesis XMCD work as been performed collaboratively with Prof. G. van der Laan, who has performed the presented atomic mutiplet theory calculations in Wien2K.

XMCD measurements were performed at beamlines I06 and I10, Diamond Light Source, UK and beamlines 4.0.2 and 6.3.1, Advanced Light Souce, CA. Measurements at Diamond were performed at He temperatures ($\sim$1.5 K) within a superconducting magnet ($\pm$10 T). ALS measurements used a lower field (0.8 T) electromagnet and have a slightly higher base temperature ($\sim$8 K for He cooling). Specific details of measurements performed are given in the relevant chapters.

3.3.3 Polarised Neutron Reflectometry

Polarised neutron reflectometry (PNR) is a neutron technique with highly similar theory to x-ray reflectometry covered earlier. With it being a neutron based technique the contrast in scattering length density comes from the nuclei of interacting elements (defined by the b-factor) rather than by interaction with the electrons, as with x-rays. This distinction, for the most part, has no direct impact for this work and is more valuable for experiments with very light elements, for which neutrons are more resolving than x-rays. If a material is magnetically polarised then spin-up and spin-down polarised neutrons will each see a different pseudopotential, combining the structural and magnetic components. Through appropriate modelling the scattering length density for different neutron spin states can be obtained and, in turn, the

magnetic and physical structure of the film. A detailed description of PNR and its application is given in Ref. [46]. In summary it provides information of the magnetic order of the material in relation to the physical structure of the film. This is highly applicable to TIs where it has been predicted [59, 60] that enhancement of ferromagnetic order may occur at the surface by mediation through free electrons of the TSS (RKKY interaction).

PNR data presented in this thesis were measured at the POLREF instrument at ISIS Neutron and Muon Source, UK. Measurements were taken for neutrons polarised in the plane of the samples and detected using time-of-flight. The sample is within a cryostat capable of He temperatures ($\sim$5 K) and with a field applied in the sample plane. Please note that although an out-of-plane field is desirable, this has the effect of de-polarising the neutron beam. Data are modelled in GenX, with all modelling performed collaboratively with POLREF beamline staff.

Chapter 4

MBE Growth of Bi_2Se_3, Bi_2Te_3 and Sb_2Te_3

The main focus of this work has been the controlled doping of TI thin films with transition metal elements, with the expectation of inducing ferromagnetic order and hence tuning the surface band gap. Before this can begin it is necessary to establish optimum growth recipes of the relevant undoped binary alloys and to explore fundamental properties of these base materials. Various considerations affect the choice of substrate material and high quality growth has been successfully demonstrated on a wide variety of substrates [61, 62, 63, 64, 65, 66, 67, 68]. Most films grown as part of this thesis were fabricated on sapphire (0001) substrates, on which it is possible to grow high quality single crystal Bi_2Te_3, Bi_2Se_3, and Sb_2Te_3 crystals, as presented below. Sapphire is advantageous as it provides an excellent surface for growth, is relatively low cost, easy to prepare and is readily available as a high quality substrate, due to its use in the semiconductor industry. This chapter will demonstrate the optimum growth of Bi_2Te_3, Bi_2Se_3, and Sb_2Te_3 thin films on sapphire substrates as a building block to later magnetic doping. Later in this chapter it will be shown that high quality films can be fabricated on the amorphous substrate material fused

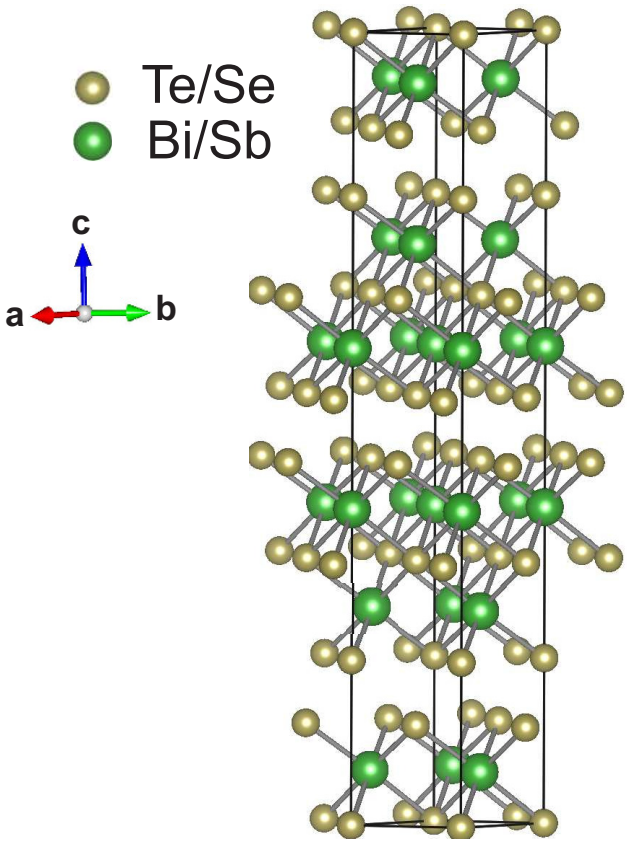

Figure 4.1: Crystal structure of $(Bi/Sb)_2(Te/Se)_3$ within the $R\bar{3}m$ space group. The quintuple layered structure is clearly visible, with van der Waals bonding between the Se/Te layers.

silica. Growth of Bi_2Te_3 on Ge (111) semiconductor wafers will also be explored.

4.1 Growth on Sapphire

As has been mentioned earlier, all of the chalcogenide TI materials (Bi_2Se_3, Bi_2Te_3, and Sb_2Te_3) grow via a mechanism of van der Waals epitaxy [69], with a strongly layered structure of $R\bar{3}m$ space group symmetry, as shown in Fig. 4.1. The lattice constants for these materials are summarised in Tab. 4.1. Sapphire substrates (received from Crystec and MTI Crystal) were cleaved into 1/4 pieces of a 2" wafer. After cleaving, the substrates were solvent cleaned using the procedure described in Appendix B before loading into the load lock and baking under UHV conditions overnight (∼8 hours).

Material	$a = b$ (Å)	c Å
Bi2Se3	4.1396	28.636
Bi2Te3	4.3852	30.483
Sb2Te3	4.262	30.450

Table 4.1: Summary of lattice parameters of the chalcogenide TI compounds. a, b, and c are the lattice vectors defined in Fig. 4.1.

Thin films of Bi_2Se_3, Bi_2Te_3 and Sb_2Te_3 were grown by MBE using broadly similar recipes, with some notable differences which will be highlighted as necessary. At the start of growth a clean c-plane sapphire (0001) substrate is transferred into the growth chamber before the start of source calibrations. During source calibrations the substrate is heated to 450°C to further ensure a pure surface and to prevent any deposition during source calibration. During this process the substrate is facing away from the cells and so there is no direct incident flux. Sources are each calibrated by first setting the approximate temperature required for the desired flux, dictated by the last full calibration (see Appendix A), and then adjusting the temperature up or down to meet the desired output flux. Based on previous publications [64], as well as personal experience, the (Bi/Sb):(Te/Se) flux ratio is kept fixed at 1:10 for all grown samples. This overpressure of the chalcogen element reduces the formation of Te/Se vacancies within the crystal and has been shown to lead to the desired 2:3 stoichiometry [67]. This growth rate is limited by the incident Bi/Sb flux and any excess Te/Se not incorporated into the crystal will desorb from the surface (when above a critical substrate temperature). Typically the Bi/Sb flux is set to $\sim 7 \times 10^{-7}$ Torr, which for the substrate temperatures used here leads to a typical deposition rate of $\sim$0.9 nm/min.

After source calibration the substrate RHEED pattern is recorded using 30 keV incident electrons (Fig. 4.2) to ensure a clean surface for growth. Although the full RHEED streaks are not fully visible (due to the sample not lying fully flat) some Kikuchi lines are visible in the pattern, indicating a high quality surface.

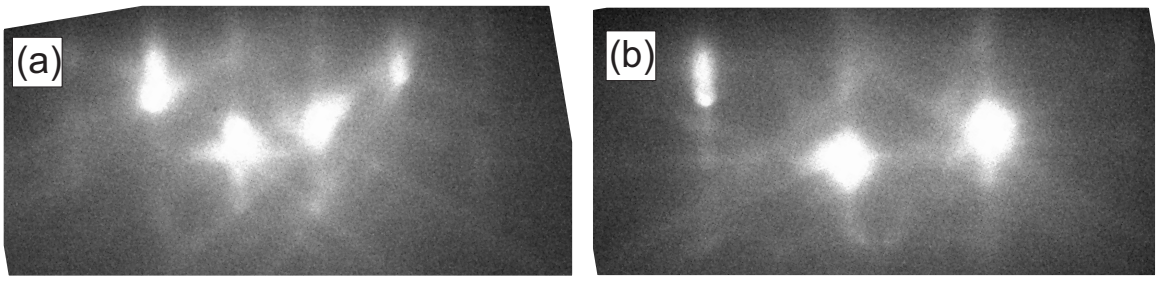

Figure 4.2: RHEED pattern of a cleaned sapphire substrate at 300°C. Images along (a) the $[10\bar{1}0]$ azimuth and (b) the $[11\bar{2}0]$ azimuth of *c*-plane sapphire.

4.1.1 Bi_2Se_3 Growth on Sapphire

Bi_2Se_3 thin films were deposited by first growing a lower temperature seed layer at $T_{\text{sub}} = 250$°C of approximately 10 nm thickness, before overgrowing the remaining film at a higher temperature of $T_{\text{sub}} = 300$°C. This approach has yielded the highest quality films and the use of a seed layer becomes critical to establish the correct crystalline phase when later doping with transition metals.

After deposition of the nucleation layer the sample is overgrown for 120 minutes at the raised substrate temperature. After growth, a sharp 2D-like RHEED pattern is observed [Fig. 4.3(a)], indicative of high quality layer growth. This pattern is invariant upon sample rotation by 60° increments, indicating a 3-fold symmetry (plus twin domains) in the sample plane. AFM studies confirm the spiral growth mode of the film [Fig 4.3(b)] and it is easy to see the 3-fold (plus inversion) in-plane symmetry of the material from the applied fast Fourier transform (FFT) [Fig 4.3(c)]. The root-mean-square (RMS) surface roughness (σ_{RMS}) is found to be (1.76 ± 0.18) nm across the 4 μm^2 scanned area.

X-ray studies are used to characterise the thin film using the Bruker D8 diffractometer described in section 3.2.1. The XRD [Fig 4.4 (a)] measured is fitted using Fullprof and gives a stated *c*-axis parameter of (28.65 ± 0.01) Å, closely agreeing with the anticipated Bi_2Se_3 lattice parameter of 28.636 Å (ICSD 617072) [70]. Some vari-

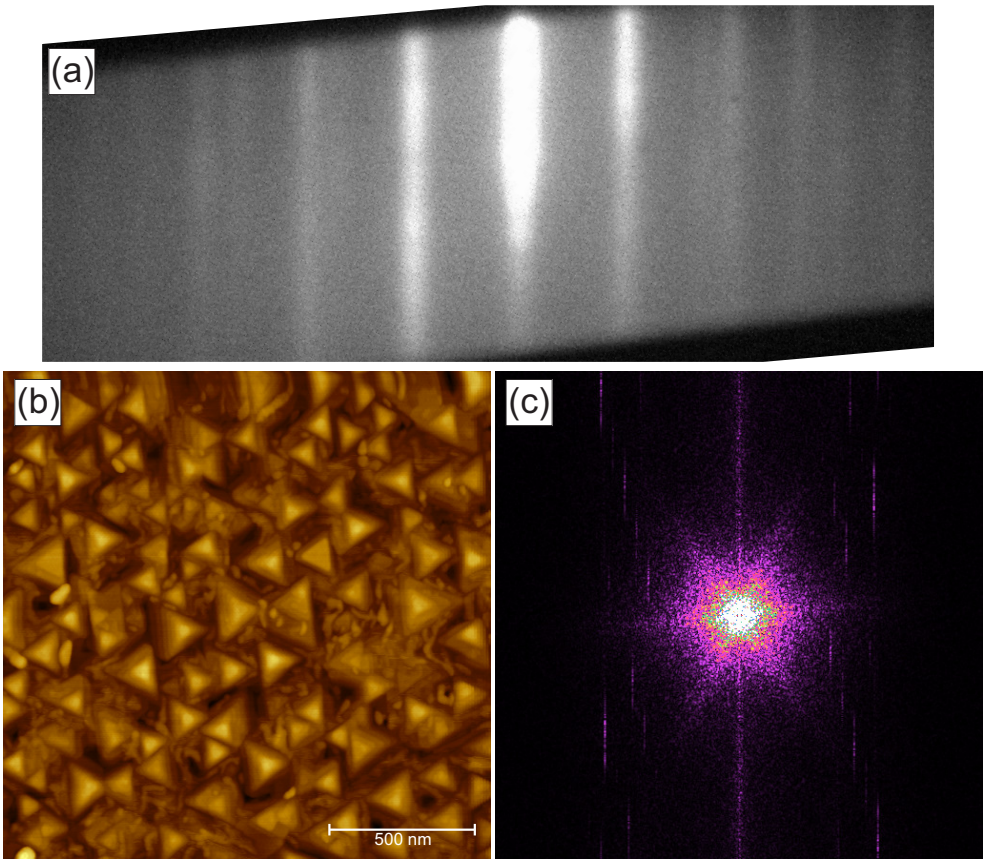

Figure 4.3: (a) RHEED pattern of a grown Bi_2Se_3 film (T_{sub} = 110°C) along the $[10\bar{1}0]$ azimuth of the sapphire substrate. The pattern indicates good 2D film growth. (b) AFM scan of grown 90 nm thick Bi_2Se_3 film, showing triangular islands indicative of spiral growth in this material. (c) Fast Fourier transform (FFT) of the AFM scan area, from which one can see the 6-fold symmetry (3 plus twin domains) of the $R\bar{3}m$ space group.

ation in the lattice constants is to be expected between bulk samples and thin films, due to epitaxial strain effects present in the film.

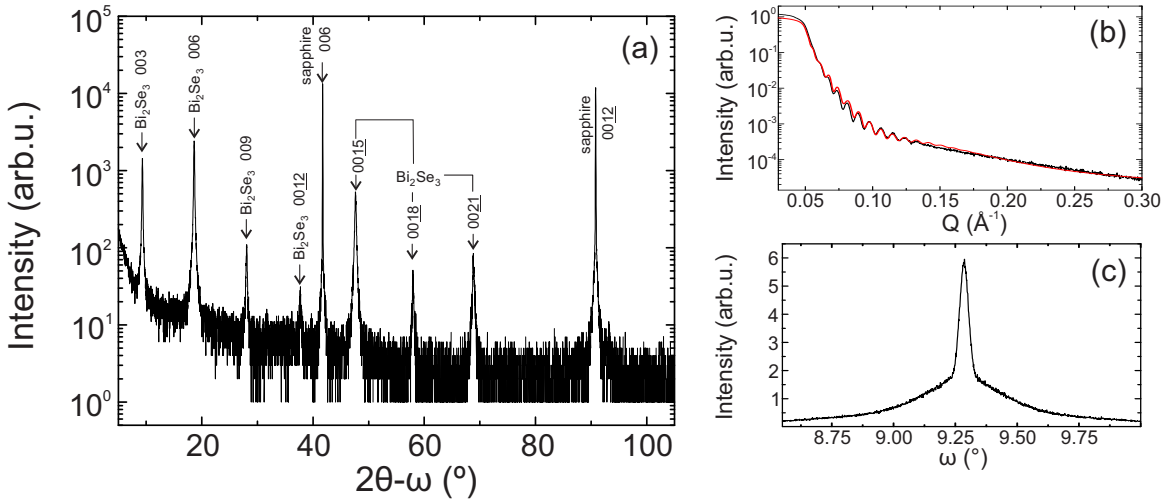

Figure 4.4: X-ray studies of a Bi_2Se_3 thin film on a sapphire (0001) substrate. (a) X-ray diffraction with relevant peaks labelled. (b) X-ray reflectivity of the measured film (black) and fitted model in GenX (red). (c) Rocking curve of the 006 Bi_2Se_3 peak.

XRR studies are carried out [Fig. 4.4 (b)] and modelled using GenX. The best fit to the experimental data is obtained by using a 3-layer structure for the Bi_2Se_3 film that will allow the film thickness and density to independently vary towards the substrate and surface interfaces. This approach permits the incorporation of strain and relaxation effects present in the film into the fitted model. The model indicates a full film thickness of (90.4 ± 1) nm with a surface roughness of (3.3 ± 0.1) nm, in broad agreement with the RMS roughness from AFM studies. X-ray rocking curve measurements of the 006 Bi_2Se_3 peak show high-quality crystalline order with a peak FWHM of 0.0556°.

Bi_2Se_3 has been demonstrated to grow well on *c*-plane sapphire with a high degree of crystalline quality. The van der Waals epitaxy growth mechanism allows the film to overcome the relatively large (∼8%) lattice mismatch between sapphire and Bi_2Se_3 whilst AFM studies indicate that the overgrown film still retains in-plane or-

der enforced by epitaxial constraints. This section will set a baseline from which it is possible to determine the effect that doping has on the crystal structure.

4.1.2 Bi_2Te_3 Growth on Sapphire

Similar to the previous Bi_2Se_3 growth, Bi_2Te_3 is first deposited on the cleaned sapphire substrate at a lower substrate temperature of $T_{sub} = 200°C$ to establish a nucleation layer of ∼10 nm thickness, as observed by RHEED. The sample is then annealed to $T_{sub} = 250°C$ for 30 minutes under a background of Te. This sample recipe has previously demonstrated the highest quality film growth, with large terraces observed by AFM, due to the limitation of Te vacancies by the background overpressure [64]. The remaining film is then overgrown for 120 minutes at the elevated substrate temperature. Unlike Se, the Te is not evaporated from a cracker cell, though this has no apparent impact on the quality of films grown here compared with prior work where a cracker cell was used [64].

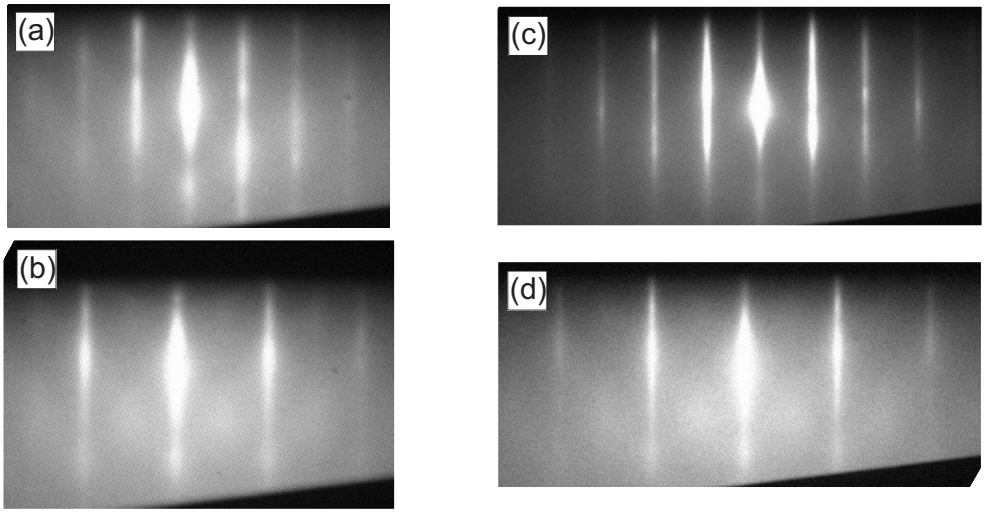

Figure 4.5: RHEED images of grown Bi_2Te_3 film on sapphire for 30 keV incident electrons. (a) Diffraction pattern of 10 nm nucleation layer at $T_{sub} = 200°C$ along the $[10\bar{1}0]$ azimuth of sapphire. (b) Same conditions along the $[11\bar{2}0]$ azimuth of sapphire. (c) Bi_2Te_3 film at end of annealing and full growth at $T_{sub} = 250°C$ along the $[10\bar{1}0]$ sapphire azimuth, and (d) along the $[11\bar{2}0]$ azimuth.

RHEED studies are carried out using 30 keV incident electrons on both the nucleation layer and upon the final grown film (Fig 4.5). The nucleation layer shows a clear 2D-like pattern with well defined RHEED stripes. It is evident, though, that after annealing and overgrowth the pattern is significantly enhanced. RHEED stripes are seen with greater contrast, are sharper and are present out to higher orders than in the nucleation layer. All these factors indicate an improvement to the in-plane crystal order and surface morphology for the annealed and overgrown film. Each of the distinct patterns in (a) and (c), and (b) and (d) repeat 6 times over a 360° rotation. This is, again, indicative of the anticipated 3-fold symmetry whilst including the presence of 180° rotated twin domains. The ratio of fringe spacings between the different patterns, taken at 30° relative angle, is $\sqrt{3}$, as expected for the $R\bar{3}m$ space group.

AFM studies are carried out on the grown film to further understand the growth morphology. Previous studies have demonstrated high quality Bi_2Te_3 growth on sapphire, parameterised by large terraces and large, flattened Bi_2Te_3 spirals [64]. The aim here is therefore to replicate such demonstrated growth quality as a starting point for doping studies.

Figure 4.6 shows the AFM results obtained for the grown film. It is clear by inspection that the growth mode is broadly similar to that of Bi_2Se_3 , which is not unexpected given their identical space group. The surface of the material is exceptionally smooth, however, with very large 'islands' of spiral growth compared with Bi_2Se_3. Figure 4.6 (c) shows a linescan over the highlighted area in (b) from which one may see the typical quintuple layer steps of this material of around 1 nm in height (1/3 of the unit cell), c.f. Fig 4.1. The spiral growth mode referenced here has been observed in thin films of Bi_2Se_3 [71] and Bi_2Te_3 [72]. These growth spirals originate from a single screw dislocation during the step-flow growth of the crystal. Evidence of this spiral growth mode is seen by AFM as triangular shaped domains with defined

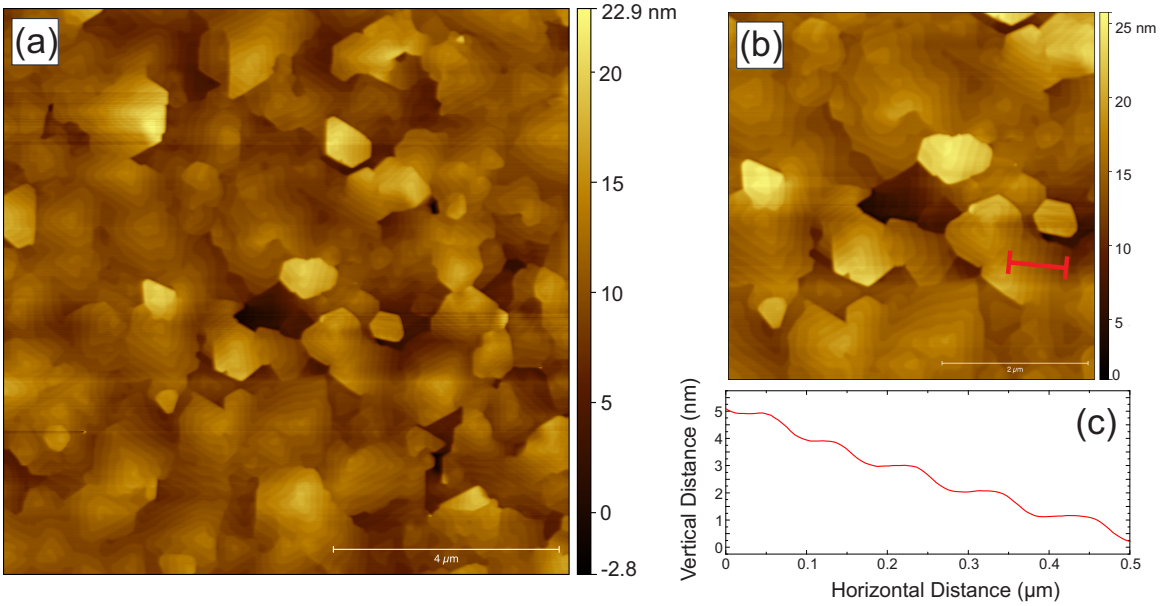

Figure 4.6: AFM images of grown Bi_2Te_3 film on sapphire. (a) 10x10 μm^2 AFM scan showing a highly smooth surface morphology with well defined terraces and spiral growth. (b) A smaller scan area showing greater detail. The red line indicates a linescan shown in (c), demonstrating the ∼1 nm-high quintuple layer stacks in this material.

terraces of quintuple layer (∼1 nm) height.

To further understand the structure of the grown material, X-ray studies are carried out in the same manner as for the Bi_2Se_3 sample; the results of which are shown in Fig. 4.7. The measured XRD spectrum [Fig. 4.7 (a)] indicates a highly *c*-axis oriented high quality crystal, with no evidence of parasitic phases or of distortions to the cryt-sal lattice. Fullprof refinement provides a *c*-axis lattice parameter of (30.44 ± 0.01) Å. This value is in excellent agreement with the anticipated value of 30.497 Å (ICSD 158366). This would indicate the film grows with very little (or no) imposed epitaxial strain. XRR is again used to determine the film thickness and roughness [Fig 4.7 (b)], giving a layer thickness of (69.1 ± 0.1) nm and a surface roughness of (3.4 ± 0.1) nm. This data is modelled using a 3-layer split film in GenX. Rocking curve measurements on the 006 peak of Bi_2Te_3 show a highly confined peak, with FWHM of 0.04306°, in-

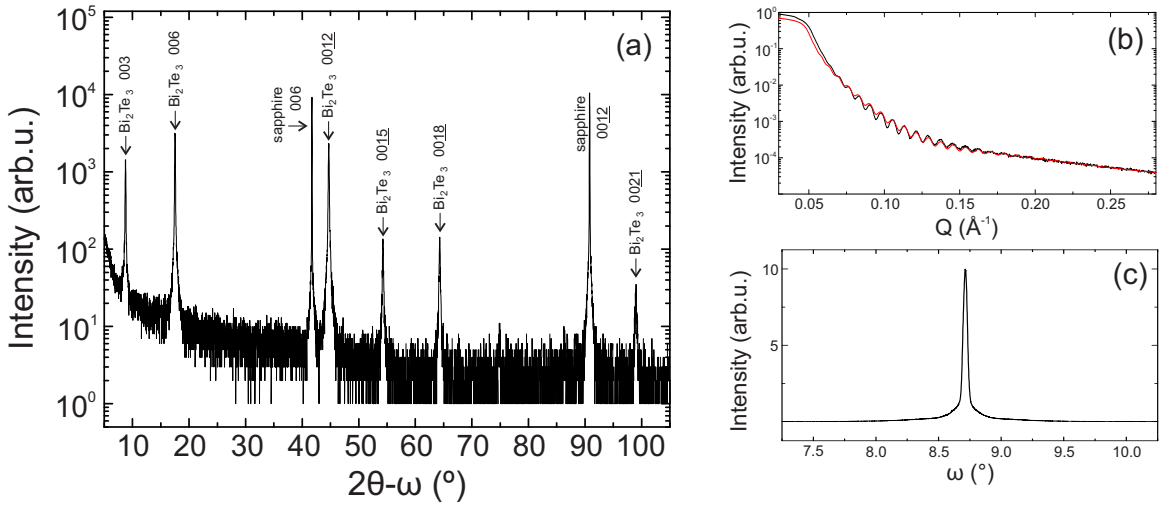

Figure 4.7: X-ray studies of a Bi_2Te_3 thin film on a sapphire (0001) substrate. (a) X-ray diffraction with relevant peaks labelled. (b) X-ray reflectivity of the measured film (black) and fitted model in GenX (red). (c) Rocking curve of the 006 Bi_2Te_3 peak.

dicative of good crystallinity along the *c*-axis. This value is slightly smaller than for Bi_2Se_3 indicating (as seen by AFM) that this a more ordered crystal.

The optimum growth recipe for high-quality Bi_2Te_3 thin films has been shown. It is evident from RHEED and AFM images that the annealing step used in growth here yields a very smooth surface and ordered crystal, superior to that of Bi_2Se_3 samples grown earlier. Unfortunately, a similar anneal has not had favourable results when applied to Bi_2Se_3 samples. A possible explanation for this is the extra volatility of Se compared to Te. It has been practically observed that Bi_2Se_3 films, for instance, are much less tolerant to heat (e.g., when mounting on a hot plate) than Bi_2Te_3 films.

4.1.3 Sb_2Te_3 Growth on Sapphire

The last binary alloy in our list of chalcogenide TIs is Sb_2Te_3. It is anticipated that this material will grow in a broadly similar, layered fashion, to the others already presented. Films are deposited on cleaned *c*-plane sapphire using the same deposition recipe as for the Bi_2Te_3 thin films. That is, a roughly 10 nm nucleation layer

is deposited at $T_{\text{sub}} = 200°\text{C}$ before annealing for 30 minutes and overgrowing at the higher substrate temperature of $T_{\text{sub}} = 250°\text{C}$. To reduce the formation of Te vacancies, the anneal is once again performed with an overpressure of Te.

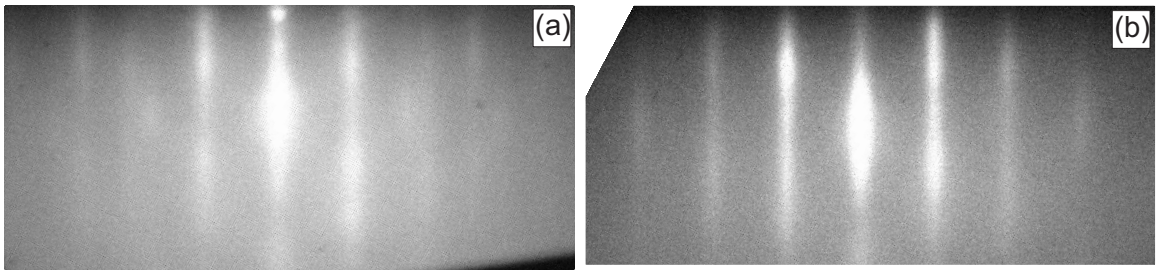

Figure 4.8: RHEED images of grown Sb_2Te_3 film on sapphire for 30 keV incident electrons, along the $[10\bar{1}0]$ azimuth of sapphire. (a) Sb_2Te_3 buffer layer at $T_{\text{sub}} = 200°\text{C}$. (b) Sb_2Te_3 annealed and overgrown film at $T_{\text{sub}} = 250°\text{C}$.

RHEED studies are carried out on the growing Sb_2Te_3 film (Fig. 4.8) and indicate a 2D layered growth as before. The pattern is not as sharp as seen for Bi_2Se_3 or Bi_2Te_3 thin films, indicating a somewhat rougher surface to the crystal. The pattern is significantly improved by annealing and overgrowing [Fig 4.8 (b)], compared with the unannealed nucleation layer [Fig 4.8 (a)].

X-ray studies are carried out, as before, on the Sb_2Te_3 thin film, as shown in Fig. 4.9. The XRD spectrum once again shows the well-ordered structure that is familiar, aligned with the $(00l)$ family of peaks along the c-axis. Rietveld refinement, using Fullprof, gives a c-axis lattice parameter of (30.395 ± 0.01) Å, compared with an anticipated (bulk) value of 30.458 Å (ICSD 2084). XRR (using the same 3-layer structure) is modelled using GenX. This gives a total film thickness of (43.6 ± 0.1) nm with a surface roughness of (5.7 ± 0.1) nm. This higher surface roughness confirms the inference from RHEED that the film grows rougher than Bi_2Te_3 or Bi_2Se_3 .

The growth of Sb_2Te_3 is an ongoing project at the time of writing and remains interesting due to recent work regarding the QAHE in Cr-doped Sb-containing chalco-

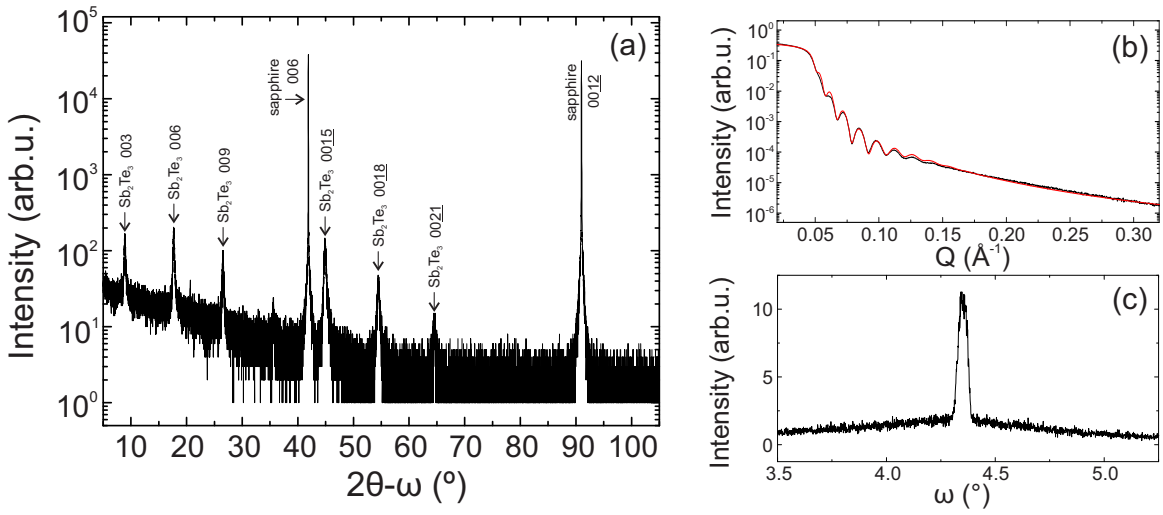

Figure 4.9: X-ray studies of a Sb_2Te_3 thin film on a sapphire (0001) substrate. (a) X-ray diffraction with relevant peaks labelled. (b) X-ray reflectivity of the measured film (black) and fitted model in GenX (red). (c) Rocking curve of the 003 Sb_2Te_3 peak.

genide TIs [12]. The thin films of Sb_2Te_3 demonstrate a proof of concept and the recipe could likely be refined to achieve the growth quality of other binary alloys.

4.2 Growth on Amorphous Fused Silica

4.2.1 Motivation

It should be clear by this point that the chalcogenide TIs Bi_2Se_3 and Bi_2Te_3 can be grown as high quality single crystals on single crystalline substrates [e.g. Sapphire (0001)] by the mechanism of van der Waals epitaxy. The question remains as to whether, given the loose epitaxial conditions imposed by van der Waals epitaxy, it is possible to grow these films on amorphous substrates as well as single crystals. Generally, this is not possible in MBE as epitaxial constraints between the substrate and overgrown film are a prerequisite for single crystal growth.

Bi_2Se_3 and Bi_2Te_3 have long been known and studied within the context of thermoelectric materials long before their re-discovery as topological insulators [6]. It is

valuable then to make a further investigation of their thermoelectric properties in thin film form within the new context of TIs. However, the typically used single crystal substrates are not suitable for detailed thermoelectric measurements, for which thermally and electrically insulating substrates are needed. Many insulating oxides, such as α-SiO_2, are also piezoelectric which leads to induced charges at the interface with the TI. Finally, thermal expansion in the temperature range of interest can lead to a significant substrate dependence to the measured thermoelectric properties [73]. SiO_2 in its amorphous form (vitreous SiO_2 or fused quartz) is not piezoelectric, has one of the lowest thermal conductivities of any solid, and a small thermal expansion coefficient, which makes it the ideal substrate for these types of measurements [74]. For comparison, its thermal conductivity (measured at room-temperature) is two orders of magnitude lower than that of Si.

The challenge with the growth of single-crystalline films on an amorphous substrate is to form a coherent crystalline order, given the lack of epitaxial constraints which can stabilise a particular phase or crystalline orientation. Exfoliated films have been previously used to avoid unwanted thermal contributions from the substrate. However, these have generally been seen to be of low quality and therefore are unsuitable for reproducible thermal or electrical measurements [75]. It has been shown that Bi_2Se_3 can be grown with a c-axis orientation on SiO_2/Si owing to van der Waals epitaxy [76], however, the lack of in-plane rotational ordering begs the question whether the topological surface state will survive. For Bi_2Se_3 on SiO_2 films on Si the question has been answered positively and the TSS has been found to be robust [77]. However, this still leaves the thermal expansion problem due to the underlying Si substrate, which may strain the film.

In this section, I will demonstrate that Bi_2Se_3 and Bi_2Te_3 can be grown as high-quality mosaic single-crystalline layers on amorphous fused silica substrates. The topological surface state is investigated (via ARPES) and is found to be robust, even

in the presence of in-plane rotational disorder. The work presented in this section has been published as Ref. [78].

4.2.2 Experiment and Results

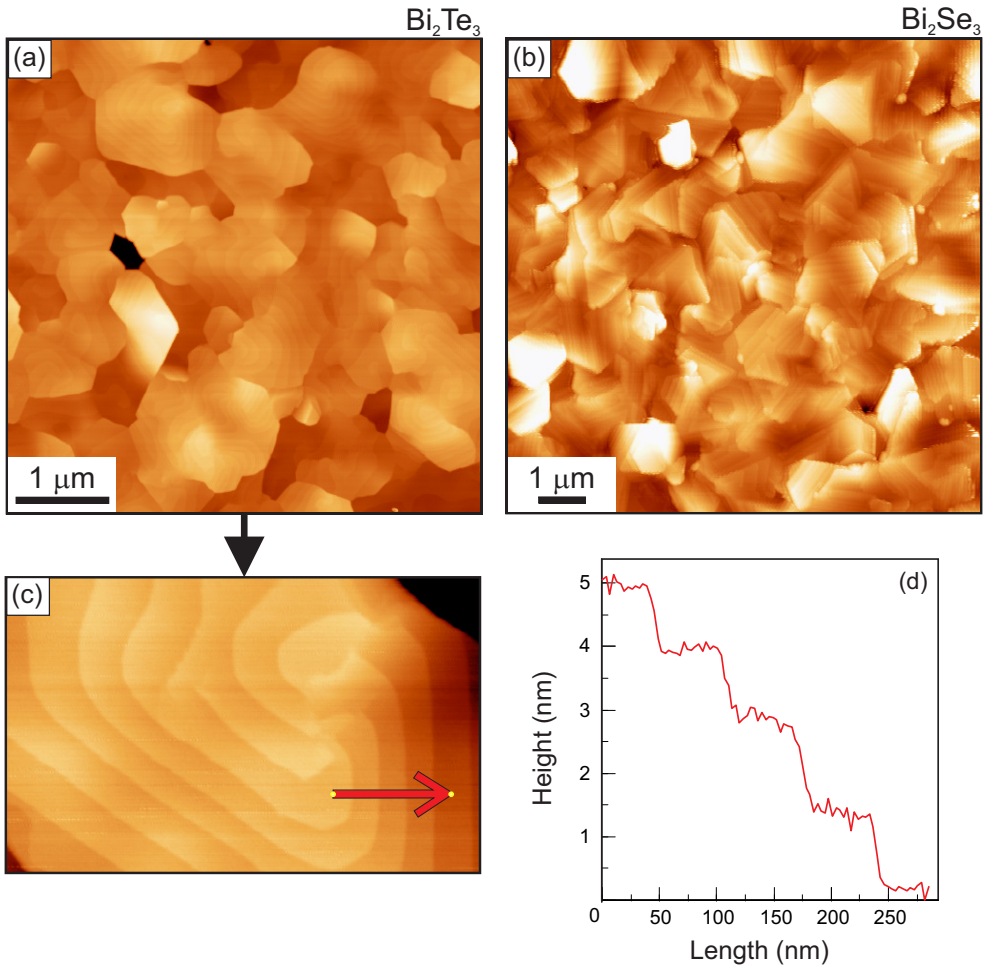

Figure 4.10: (a) AFM of a 32.8-nm-thick Bi_2Te_3 film on fused silica. The typical spiral growth pattern with distinct terraces, common for this material, are observed. (b) AFM of a 69.9-nm-thick Bi_2Se_3 film on fused silica. The film shows more 3D-like defects than Bi_2Te_3. (c) Larger scale image of a Bi_2Te_3 spiral growth. Red arrow indicates a linescan direction. (d) Linescan from (c) demonstrating the ∼1 nm quintuple layer steps of the Bi_2Te_3 thin film.

The Bi_2Se_3 and Bi_2Te_3 thin films were deposited using the same recipe as has proved successful on sapphire. In brief, solvent cleaned fused silica substrates are

baked in vacuum up to ∼500 °C to provide a clean surface. The thin films are deposited by co-deposition, with the Se again originating from a cracker cell. The beam-flux monitor (BFM) is used to maintain a Bi:(Se/Te) flux ratio of 1:10 during growth. Films were grown by a two-step method that has previously yielded high quality single crystals. By this method an initial 15-nm-thick nucleation layer of $Bi_2(Se/Te)_3$ is grown at a lower substrate temperature ($T_{sub} = 200°C$) before overgrowing at a 50 °C higher substrate temperature. Additionally Bi_2Te_3 films are annealed for 30 minutes after the nucleation layer deposition.

AFM studies, shown in Fig. 4.10, were performed in tapping mode and revealed a spiral growth mode common for this class of materials [64]. It is clear by inspection that Bi_2Te_3 shows an improved surface morphology, similar to that obtained on single crystal substrates, than that of Bi_2Se_3, which displays a significantly rougher surface with more 3D-like surface features. This is confirmed by a slightly increased RMS surface roughness of $\sigma = 1.345$ nm for Bi_2Se_3 compared to $\sigma = 1.128$ nm for Bi_2Te_3, both taken over a 2 μm scan area. A closer look at the Bi_2Te_3 spirals [Fig. 4.10 (c)] reveals the layer-by-layer spiral growth and distinct terraces normally observed for Bi_2Te_3 thin films. Figure 4.10 (d) shows a linescan across the terraces (red line) displaying the Te-Bi-Te-Bi-Te quintuple layer steps of ∼1 nm height.

XRD, XRR and rocking curves were performed using the Bruker D8 diffractometer with incident Cu K-α_1 radiation. The incident beam was limited by a 0.4 mm beam limiting slit. Extraction of the c-axis lattice parameter was performed using Fullprof and models of the X-ray reflectivity data were simulated in GenX. Reflectivity models were built using tabulated density values for the relevant materials ($\rho_{Bi_2Se_3} = 7.51$ g/cm^3, $\rho_{Bi_2Te_3} = 7.73$ g/cm^3, $\rho_{Silica} = 2.2$ g/cm^3 [79, 80]). Figures 4.11 (a) and (b) show measured XRR data for Bi_2Se_3 and Bi_2Te_3 respectively (black) as well as the associated simulated curves from the given model (red). Films were modeled using a split structure of three layers of $Bi_2(Se/Te)_3$ where each layer was

permitted to vary independently within the model. It was found that the best fit was achieved by permitting a ∼50% reduction in film density towards the top surfcae. This is likely caused by an incomplete layer termination at the sample surface. The film thicknesses obtained for the best-fit model are shown inset to each figure. The main parameter extracted from such fits is the layer thickness, although film density and interfacial roughness parameters may also be extracted. The surface roughness obtained for these samples was 3.6 nm and 1.6 nm for Bi_2Se_3 and Bi_2Te_3 respectively, in broad agreement with parameters obtained from AFM studies.

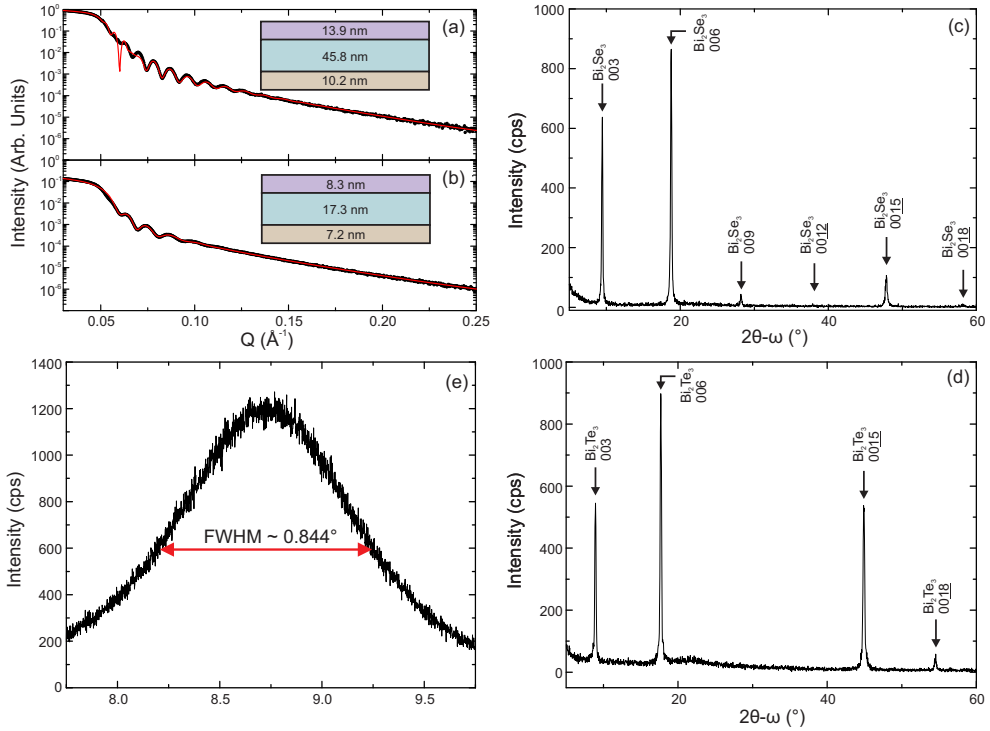

Figure 4.11: XRR studies for (a) Bi_2Se_3 and (b) Bi_2Te_3 films, respectively. Data are shown as black dots and the red line is the model fit. The layer structures determined from the fits are shown as insets to each figure. XRD spectra for (c) Bi_2Se_3 and (d) Bi_2Te_3, with the observed reflections marked. (e) Rocking curve of the 006 Bi_2Te_3 peak with indicated full width at half maximum (FWHM) of 0.844°.

XRD spectra [Figures 4.11 (c) & (d)] are modeled by Rietveld refinement to extract key structural parameters of the crystal. The best fits for these crystals provide a

value of c to be (28.62 ± 0.01) Å for Bi_2Se_3 and (30.42 ± 0.01) Å for Bi_2Te_3, in close agreement with reported values (for bulk crystals) of 28.636 Å and 30.483 Å for Bi_2Se_3 and Bi_2Te_3 (ICSD 165226 and 158366), respectively. A rocking curve of the 006 peak of Bi_2Te_3 is shown in Fig. 4.11 (e). This shows a FWHM of 0.844°, an increase from similar films grown on sapphire (c.f., Fig. 4.7 and indicative of some increased disorder due to the lack of epitaxy.

ARPES measurements were undertaken at Beamline 10.0.1 of the Advanced Light Source, Berkeley (by B. Zhou and Y. L. Chen). Base pressure during measurement was $<5\times10^{-11}$ Torr at all times. ARPES data were recorded by a Scienta R4000 analyzer at 15 K sample temperature. For these measurements a thin film of Bi_2Te_3 was prepared *in-situ* by cleaving to reveal a pristine surface [81]. Figure 4.12 (a) demonstrates the band dispersion in the $k_{\|}$ direction. The samples are clearly n-type and display a distinct Dirac cone indicative of the topological surface state at the zero-momentum Γ-point. Constant energy maps [Fig. 4.12 (b)] cut along the $k_{\|}$ plane show a circular feature in the plane, where previous studies on single crystal substrates have displayed a hexagonal feature moving away from the Dirac point [36]. This smearing out of the features within the plane is attributed to the small rotational domains found within this sample, which will average out across the beam spot. Nonetheless, the characteristic Dirac band dispersion of the topological surface state remains intact despite the in-plane disorder present in the sample.

4.2.3 Conclusions

In summary, it has been shown that it is possible to grow, by MBE, high-quality, single crystalline samples of Bi_2Se_3 and Bi_2Te_3 on amorphous fused silica substrates. These samples display a well-defined out-of-plane crystallinity, with some rotational domains formed in the sample plane due to the lack of epitaxy with a single crys-

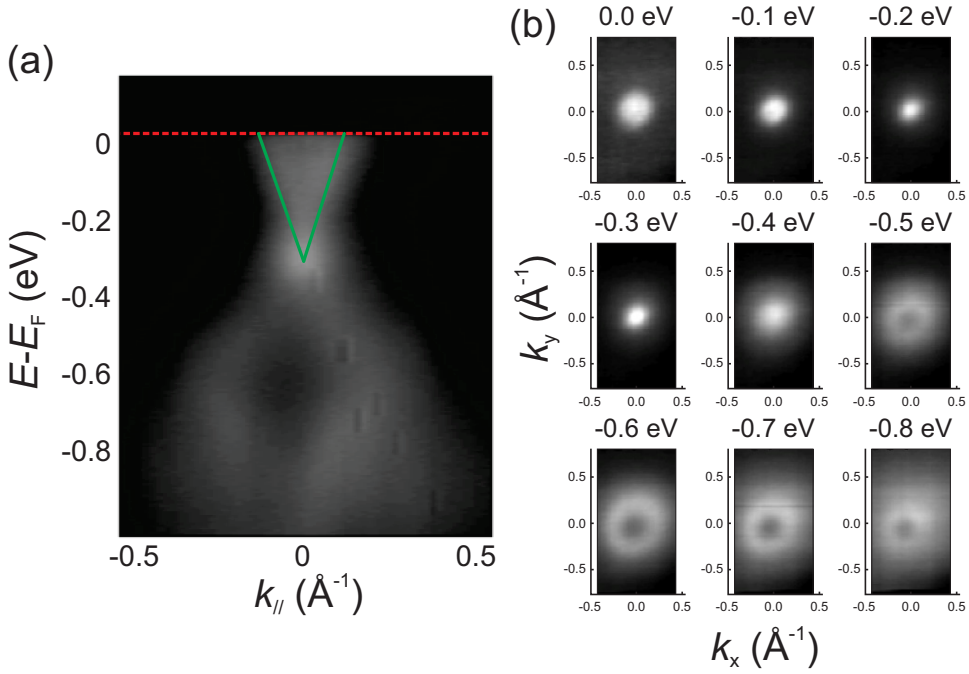

Figure 4.12: ARPES spectra obtained for a Bi_2Te_3 thin film: (a) typical Dirac band dispersion, cut along $k_{||}$ of the topological surface state (marked green) below the Fermi energy (red). (b) Constant energy cuts showing band dispersion in the $k_x - k_y$ plane.

tal substrate. The optimum growth conditions to achieve the best quality samples have been highlighted and it is generally observed that Bi_2Te_3 is of higher quality than Bi_2Se_3 on fused silica. It is seen that the typical band dispersion observed for these TI materials can be seen with ARPES, even for such amorphous substrates. Crucially, this work indicates that the topological surface state remains robust, even in the presence of significant in-plane disorder from an amorphous substrate. This work forms a key stepping stone towards further study of these materials by thermoelectric measurements and towards device application requiring flexible, transparent substrates.

4.3 Growth of Bi_2Te_3 on Ge (111)

It has been asserted so far in this chapter that the chalcogenide TIs grow by van der Waals epitaxy in a manner that is mostly independent of the usual epitaxial constraints requiring a lattice matched substrate material. Recently, work was published by Schreyeck *et al.*, which has shown that significant improvement of the grown film quality of Bi_2Se_3 can be obtained when grown on lattice-matched InP (111) substrates [82]. The lattice mismatch between film and substrate in this case is 0.16%. Bi_2Te_3 has a lattice mismatch of 8% when grown on *c*-plane sapphire, although single crystals are still achievable. The plane spacing along the (111) direction of Ge is 3.266 Å [83]. The *a*, *b*, lattice constant of Bi_2Te_3 is 4.38 Å which gives a plane spacing of 3.09 Å for a 45° rotation of the film with respect to the Ge (111) substrate. This is then a 5.3% lattice mismatch between the film and substrate, greater than for InP (111) but less than with *c*-plane sapphire. It may, therefore, be expected that higher quality films may be grown on Ge (111) substrates than has been previously achieved on sapphire. Ge is a promising candidate substrate for future integration of TIs for device applications. Specifically Ge has for some time been used and interfaced with electronics as a high-mobility semiconductor. If TI-based devices are to be realised, then interfacing with existing electronics is a critical requirement. As such, the demonstration of TI growth on semiconductor substrates such as Ge is an important stepping stone.

Ge (111) substrates are received as 'epi-ready' 2" wafers from CrysTec GmbH. The full wafer is cut into 4 to fit into the 1/4-sized sample holder used in the machine. All substrates were cleaned using the standard recipe outlined in Appendix B and baked in vacuum to 250°C overnight to leave a clean surface for growth. Ge substrates generally have a surface oxide layer that is not desirable for growth. This oxide is easily desorbed from the material by heating to higher (∼600°C) substrate

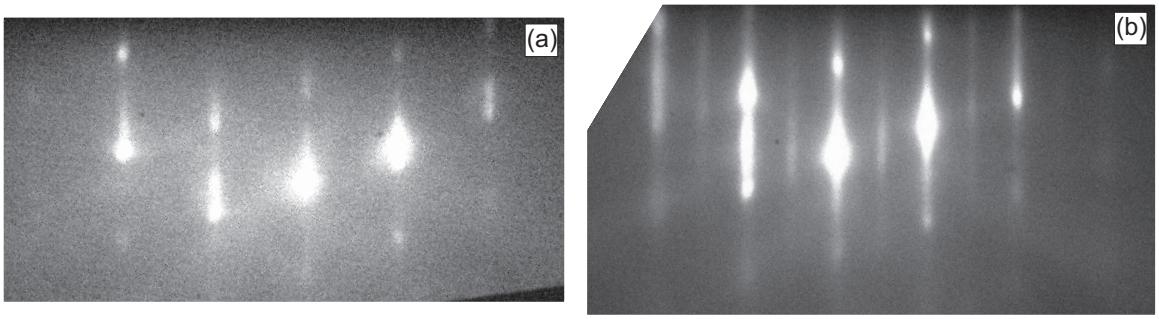

Figure 4.13: RHEED images of Ge (111) substrate taken along the $< 2\bar{1}\bar{1} >$ azimth with 30 keV incident electrons. (a) Cleaned substrate at $T_{\text{sub}} = 50°\text{C}$. (b) Reconstructed Ge (111) surface after 30 minute anneal at $T_{\text{sub}} = 600°\text{C}$ showing a c(8x2) surface reconstruction.

temperatures [84]. Figure 4.13 demonstrates the observed surface reconstruction after such an anneal for 30 minutes. The oxide layer leads to a dull RHEED pattern with some 3D nature to it, evidenced by distinct spots in the pattern [Fig 4.13 (a)]. After a high temperature anneal the RHEED pattern is brighter with clear 2D stripes of the clean, reconstructed surface [Fig 4.13 (b)].

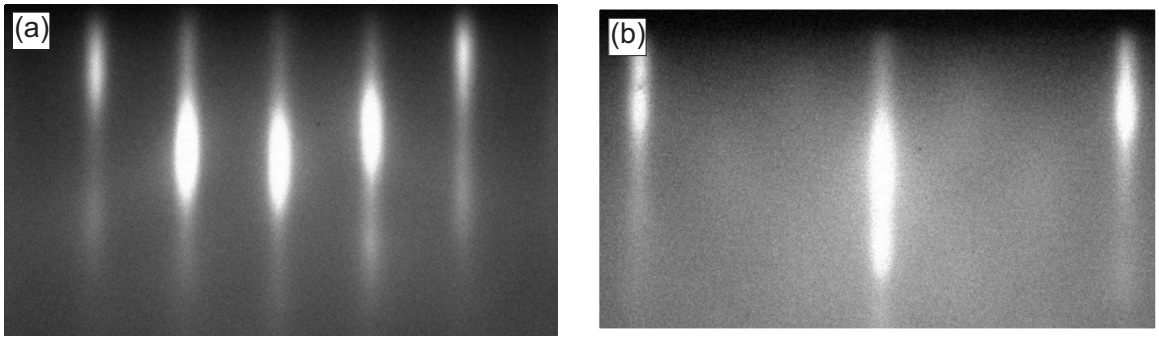

Figure 4.14: RHEED images of Bi_2Te_3 thin film on Ge (111) substrate with 30 keV incident electrons. Images taken at $T_{\text{sub}} = 250°\text{C}$. Images (a) and (b) are taken at a relative 30° rotation of the sample.

Bi_2Te_3 thin films were deposited on Ge substrates by the same co-deposition recipe as previously outlined. First a nucleation layer at $T_{\text{sub}} = 200°\text{C}$, followed by a 30 minute anneal and overgrowth at $T_{\text{sub}} = 300°\text{C}$. Additionally, it is common for MBE growth of III-V systems to first deposit a buffer layer of the substrate material before

the main film growth. This is also attempted, where a ∼10 nm film of Ge is first deposited onto the substrate before the Bi_2Te_3 overgrowth. In both cases RHEED (Fig. 4.14) appears identical for the finally grown film and displays a broadly similar pattern to that seen for growth on sapphire. The RHEED patterns have the same 6-fold periodic pattern upon sample rotation as has been previously observed.

AFM studies are carried out on the grown films, as before. These studies indicate a considerable difference in the growth morphology between films grown directly on the Ge substrate [Fig 4.15 (a), (b)] compared with those grown on top of a grown Ge buffer layer [Fig 4.15 (c), (d)]. Although without the buffer layer no terraces or anticipated 3-fold symmetry are observed, the RMS roughness over a 1 μm^2 scan area is only (0.86 ± 0.1) nm. This value would indicate a surface as good, or better, than the growth on sapphire. However, after growing on a buffer layer of Ge, this value increases significantly to (2.9 ± 1.8) nm. The film grown on a Ge buffer does appear to have the anticipated spiral growth mode of Bi_2Te_3 though.

Overall the AFM results indicate a markedly different growth mode for the unbuffered sample from that of films grown on sapphire. The samples grown on a Ge buffer do show spirals, but still have visible 'flakes' on the terraces that are not seen in samples grown on sapphire. It appears that, though van der Waals epitaxy is reasonably tolerant to lattice mismatch, there is still a significant affect of the substrate on the grown film.

X-ray studies are once again employed to further understand the manner of growth on these Ge substrates. XRD, XRR and rocking curves are measured using the same Bruker D8 diffractometer as earlier. XRD spectra [Fig. 4.16 (a), (b)] of the unbuffered and Ge buffered film show little difference between them. Both show the expected $(00l)$ peak ordering along the c-axis as has been previously observed. However, at higher angles some lifting of the peak degeneracy is present as peaks broaden asymmetrically and form peak doublets. This effect is attributed to some

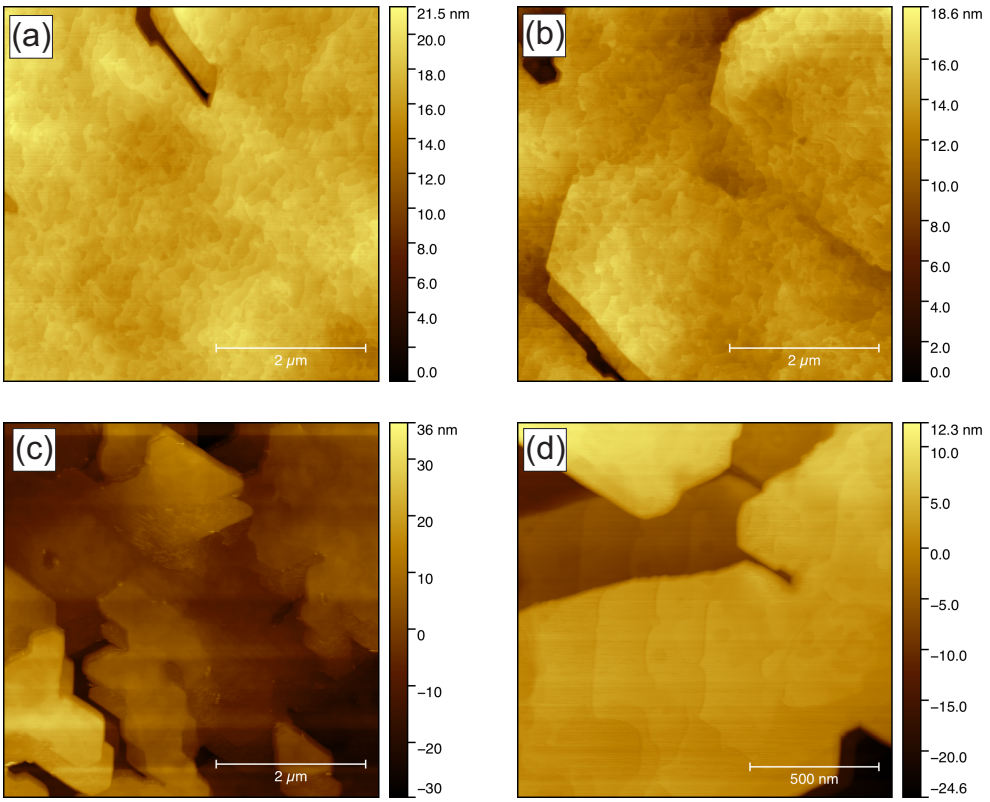

Figure 4.15: AFM images of grown Bi_2Te_3 film on Ge (111). (a) Bi_2Te_3 film with no Ge buffer. A 5×5 μm^2 AFM scan showing a relatively smooth surface, but without defined terraces. (b) Another portion of the same film, showing some poorly defined terraces. (c) AFM of a 5×5 μm^2 scan area of a Bi_2Te_3 film on a Ge buffer. The surface is considerably rougher, but terraces are visible. (d) Finer, 1.5×1.5 μm^2, image of the same sample showing greater detail of observed terraces.

additional rotational domains being present in the sample (or 3D defects) that cause some elements of the film to not have the *c*-axis normal to the sample surface. Fullprof is used to fit only the (003) family of Bi_2Te_3 peaks for each of the samples. The *c*-axis lattice constants are found to be (30.47 ± 0.01) nm for the unbuffered sample and (30.46 ± 0.01) nm for the Ge buffered sample. Both values are slightly higher than that obtained for Bi_2Te_3 on sapphire, though only just outside of the error bar.

XRR curves [Fig. 4.16 (c), (d)] are measured for the unbuffered and Ge buffered samples. These XRR curves show no periodic oscillations and as such no fit to extract film thickness and roughness parameters is possible. There are two possible causes of

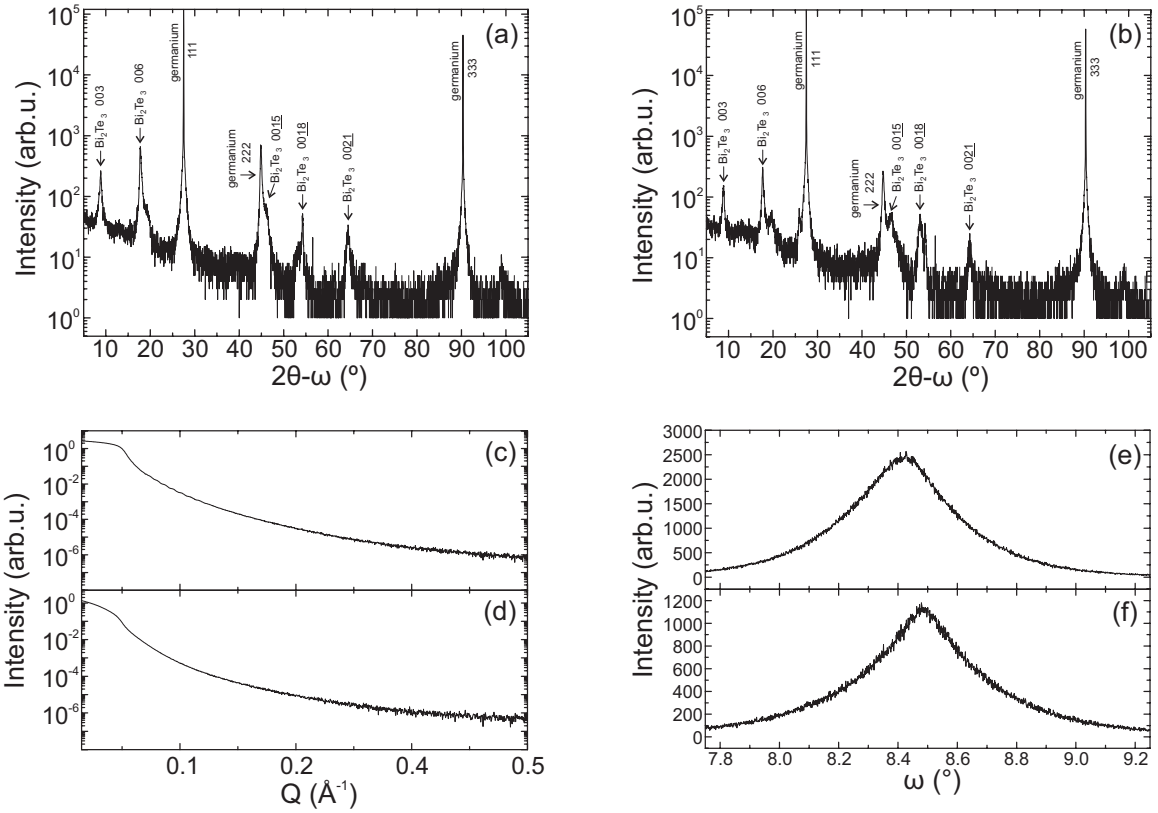

Figure 4.16: X-ray studies of a Bi_2Te_3 thin film on a Ge (111) substrate. (a) X-ray diffraction with relevant peaks labelled of the unbuffered sample. (b) X-ray diffraction with relevant peaks labelled of the Ge buffered sample. (c) X-ray reflectivity of the unbuffered film. (d) X-ray reflectivity of the Ge buffered film. (e) Rocking curve of the 006 Bi_2Te_3 peak for unbuffered film. (f) Rocking curve of the 006 Bi_2Te_3 peak for the Ge buffered film.

such an effect: a lack of x-ray contrast between the substrate and film, or such a high surface roughness that all oscillations are fully damped out. X-ray contrast is defined by the scattering length density (SLD), a function of both mass density and atomic numbers. The calculated SLDs (from GenX) for Ge and Bi_2Te_3 are markedly different and, in fact, provide only slightly lower contrast than for films grown on sapphire. As such, this lack of oscillations is determined to originate from the higher surface roughness, as observed by AFM. Rocking curves are measured about the 006 peak of Bi_2Te_3 for the unbuffered [Fig. 4.16 (e)] and Ge buffered [Fig. 4.16 (f)] samples. Both clearly show a defined, but broader, rocking curve than observed for films grown on

sapphire. The measured peak FWHM for the unbuffered and Ge buffered samples is 0.3579° and 0.3268° respectively. These values are an order of magnitude higher than obtained for sapphire, indicating considerably more disorder in the crystal along the *c*-axis.

In summary, it seems that samples grown on Ge show the expected phase, but with a different growth mode and greater disorder than for films grown on sapphire. There seems to be little effect on the bulk crystallinity of the film by growing with and without a Ge buffer layer, though this layer does seem to affect the surface morphology somewhat, as evidenced by AFM. Although the effective lattice mismatch between Ge (111) and Bi_2Te_3 is less than for *c*-plane sapphire, the films grown on Ge substrates seem to be of significantly lower crystal quality compared with those grown on sapphire. It seems sensible, therefore, to continue with sapphire as the substrate of choice for the continuing dopant studies.

4.4 Summary and Conclusions

This chapter has presented the growth of chalcogenide TIs on a variety of substrate materials. The highest quality crystals are obtained for films deposited on solvent cleaned *c*-plane sapphire substrates, and the optimum recipe for the growth for these samples has been presented. This optimisation of growth for binary alloys sets the stage for the doping of these materials with magnetic dopants, as shall be presented in later chapters.

Chapter 5

Mn-Doped Bi_2Te_3 and Bi_2Se_3

As has been mentioned in previous chapters, the aim here is to induce a ferromagnetic ground state in the material through doping with $3d$ transition metals into the bulk of the chalcogenide TI. Previous work has demonstrated the formation of a ferromagnetic ground state in Mn-doped Bi_2Te_3 bulk samples [85, 86, 87] as well as Mn-doped Bi_2Se_3 [88, 89] and Bi_2Te_3 [90] thin films. The work presented in this chapter focuses on forming a greater understanding of the nature of this doping. For instance, whether the doping is substitutional or interstitial, the limits placed on the quantity of dopant, as well as the impact the dopant has on the electronic and magnetic properties of the host material. A variety of techniques are employed to investigate the structural and magnetic properties of these doped materials. The end goal of these studies is to determine the impact such doping, and the resulting magnetic order, has on the topological surface state. This work forms the first steps towards direct manipulations of the surface band gap and, by extension, the spin states of the TSS electrons.

5.1 Mn-Doped Bi_2Te_3 Single Crystals

The work presented in this section is a collaborative effort with M. D. Watson, University of Oxford and published in Ref. [22]. Relevant experiments and figures that

are part of this collaboration have been highlighted.

5.1.1 Motivation

Although the focus of research efforts during this thesis has been on doped thin film topological insulators, there is still a large amount about these materials that may be understood from bulk crystals. There are, however, materials issues that have impacted on the quality of grown bulk samples and therefore the derived magnetic properties. In particular, it has proved challenging to control the bulk electronic properties, to find ways of reducing the defect densities and to understand the role of dopants and intercalated ions. One of the first studies to show the interplay between ferromagnetism and the breaking of time reversal symmetry in a TI was reported by Hor *et al.* [87] in Mn-doped Bi_2Te_3. They found that ferromagnetic order is established for Mn concentrations higher than $x = 0.04$ in $Mn_xBi_{2-x}Te_3$, with a Curie temperature (T_C) varying between ∼9 K and 12 K. ARPES of the surface state has shown a gap opening at the Dirac point due to the presence of magnetic impurities [37].

This section will demonstrate a study of Mn-doped Bi_2Te_3 single crystals with nominal Mn concentrations of $x_n = 0.09$ and $x_n = 0.15$, according to $Mn_{x_n}Bi_{2-x_n}Te_3$. For this section, the samples are referred to according to their nominal Mn composition, x_n. This assumes a fully substitutional doping mode, which is not really the case. The off-stoichiometry caused by other doping modes is addressed later. These samples show a ferromagnetic transition temperature of ∼9-13 K with clear signatures of a phase transition in magnetometry measurements. A combination of structural and magnetic techniques, such as SQUID, muon spin rotation (μSR) and XMCD, are employed to obtain an insight into the doping of this material, studying the link between the structural details and the physical properties.

5.1.2 Crystal Growth and Structure

Mn-doped Bi_2Te_3 single crystals, typically measuring 2-3 cm in length and 1 cm in diameter, were grown using high purity (> 99.99%) Bi, Te, and Mn. All samples in this section were fabricated by D. Prabhakaran, University of Oxford. Stoichiometric amounts of the constituent materials, according to $Mn_{x_n}Bi_{2-x_n}Te_3$ with nominal Mn concentrations of $x_n = 0.09$ and $x_n = 0.15$, were mixed, sealed in an evacuated quartz ampoule and then heated to a temperature of 1003°C over 24 h. After 10 h at this temperature they were cooled down to 855°C at a rate of 10°C/h. The actual crystal growth occurred during the cooling of the melt from 855°C to 529°C at the rate of 5°C/h. Finally, the crystals were annealed at 529°C ($x_n = 0.09$) and 579°C ($x_n = 0.15$) for 80 h and then cooled to room temperature at the rate of 10°C/h. It has to be noted that the melting point increases with Mn concentration.

The obtained single crystals were analysed by XRD using a SuperNova Oxford Diffraction system, confirming the Bi_2Te_3 crystal structure with space group $R\bar{3}m$ (Fig. 5.1). Lattice parameters are calculated using the built in software from Oxford Diffraction. The lattice parameters show very little variation with doping concentration: $a = (4.39 \pm 0.02)$ Å and $c = (30.35 \pm 0.15)$ Å for $x_n = 0.09$, and $a = (4.386 \pm 0.006))$ Å and $c = (30.42 \pm 0.1)$ Å for $x_n = 0.15$, respectively. They are almost identical to the values obtained previously for undoped samples ($a = 4.384$ Å and $c = 30.45$ Å), as well as to the values expected from literature ($a = 4.385$ Å and $c = 30.497$ Å, ICSD 158366). The samples are cleaved in the ab-plane, with the c-axis normal to the cleaved surface. Due to the relatively weak van der Waals forces between the quintuple layer stacks, stacking faults are common in this material [91]. This is evidenced by the observed XRD in Fig. 5.1 where some disorder is evident in the $(h0l)$ plane, whilst the $(hk0)$ looks considerably cleaner and more ordered.

EDX measurements were performed on these samples by S. C. Speller, University

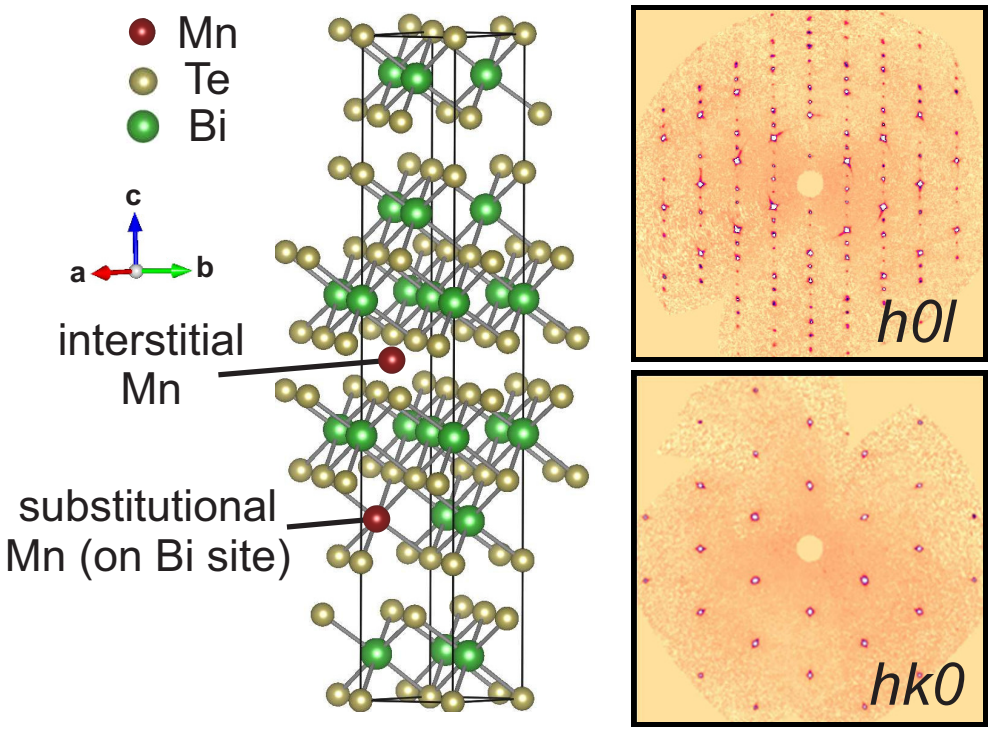

Figure 5.1: Left: Crystal structure of Bi_2Te_3 (space group $R\bar{3}m$), showing the possible doping sites for Mn atoms, which may enter the matrix in the van der Waals gap or substitute onto a Bi site. Right: X-ray single crystal diffraction patterns in the $(h0l)$ and $(hk0)$ planes for a crystal with $x_n = 0.15$, showing a weak site disorder in the $(h0l)$ plane. XRD by M. D. Watson, figure appears in [22].

of Oxford. Extensive EDX analysis from over 30 points taken from different regions on each sample is shown in Fig. 5.2. These results indicate that the samples with nominal Mn concentrations of $x_n = 0.09$ and $x_n = 0.15$ have similar average Mn doping concentrations. The statistical error for the Mn concentration is ∼1 % and for Bi ∼2 %.

The sample stoichiometry obtained by EDX (Fig. 5.2) shows a wide range of values obtained for elemental composition, depending on the location probed. This scatter seems less pronounced for the $x_n = 0.09$ sample, which was annealed at a lower temperature. Two model doping scenarios are presented: the fully interstitial doping regime ($Mn_xBi_2Te_3$) is marked by a solid line and the fully substitutional

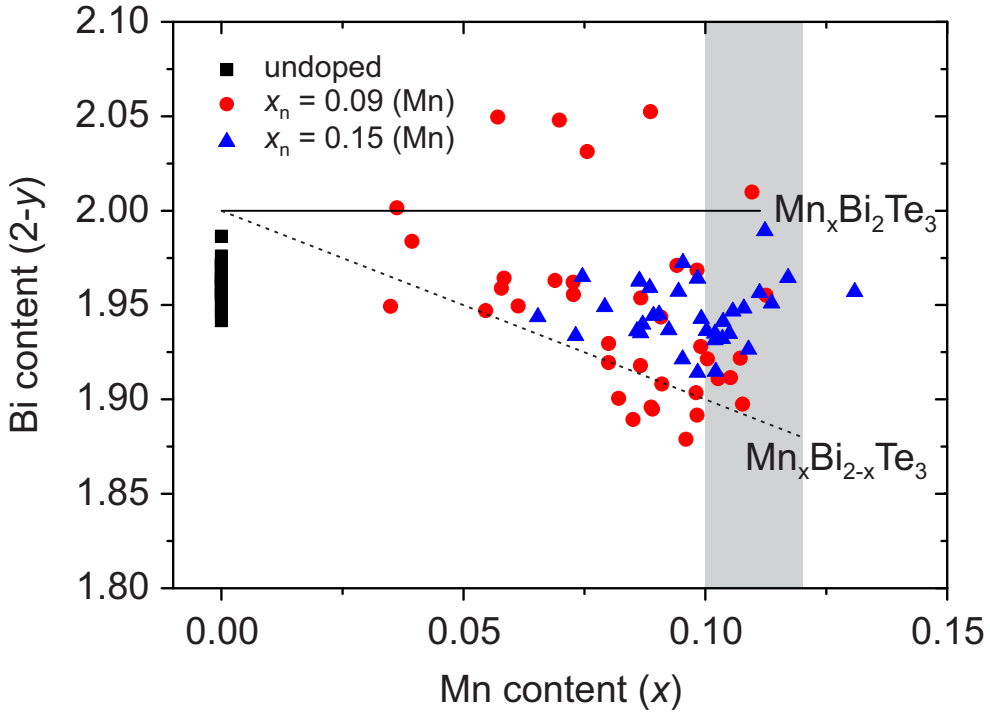

Figure 5.2: EDX analysis of Mn-doped Bi_2Te_3 crystals obtained on various cleaved pieces and several spots for nominal Mn doping concentrations of $x_n = 0.09$ (red dots) and $x_n = 0.15$ (blue triangles). The solid line represents a fixed Bi:Te stoichiometry of 2:3 with Mn being incorporated interstitially; the dashed line represents a fully substitutional Mn incorporation according to $Mn_xBi_{2-x}Te_3$. The undoped sample data is indicated by black squares. The grey shaded area represents the approximate range of the observed solubility limit of $x = 0.11 \pm 0.01$. Data from S. C. Speller, figure appears in [22].

doping regime ($Mn_xBi_{2-x}Te_3$) is shown by a dashed line. It is clear that, for both samples, there is a significant spread generally bounded by these two lines. This would indicate a mixed doping mode with some of the Mn incorporating substitutionally into the host matrix and some interstitially. It seems that for the higher doping concentration of $x_n = 0.15$, the sample is more homogeneous, with a clearly mixed doping mode. The lower doping sample ($x_n = 0.09$) has a much greater spread of measured data, but a more pronounced trend towards the fully subsitutionally doped regime. The data presented in Fig. 5.2 seems to indicate a pronounced solubility limit at $x_{\mathrm{lim}} = 0.11 \pm 0.01$, indicated by the shaded area in the figure. It may

be anticipated that, due to this solubility limit, the excess Mn in a sample with higher doping must somehow precipitate out from the host crystal. This hypothesis is supported by transmission electron microscopy (TEM) experiments, performed by S. C. Speller and shown in Fig. 5.3. TEM results show the prescence of small (nm-scale) Mn-rich precipitations on the cleaved surface of the $x_n = 0.15$ [Fig. 5.3 (b)] that are not observed on the $x_n = 0.09$ sample [Fig. 5.3 (a)]. These results suggest that Mn incorporates almost fully within the solid solution in the $x_n = 0.09$ crystal. However, as the Mn concentration is increased, a supersaturation of Mn occurs within the crystal which then precipitates out during cooling. The TEM results support the previous assertion of a solubility limit not greater than $x_{\text{lim}} = 0.11$.

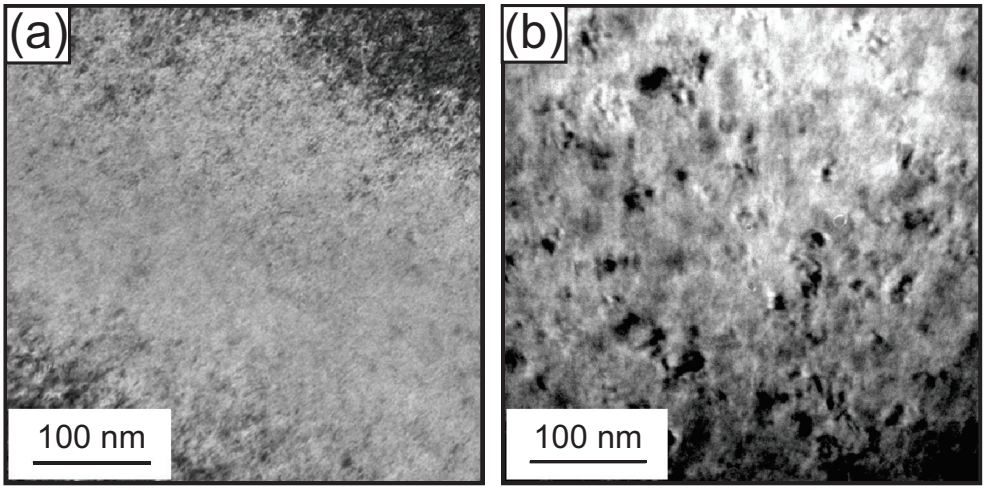

Figure 5.3: Bright-field TEM images for crystals with nominal compositions: (a) $x_n = 0.09$ and (b) $x_n = 0.15$. Diffraction contrast from the strain fields surrounding the Mn-rich precipitates is visible only for the high Mn content in (b). Data from S. C. Speller, figure appears in [22].

5.1.3 Magnetic Properties

Magnetic properties of the Mn-doped Bi_2Te_3 crystals were investigated by means of complementary magnetic characterisation techniques. SQUID magnetometry and

μSR are used, providing information about the bulk magnetic properties of the samples. XMCD (in TEY mode) is highly surface sensitive and is used to provide information regarding any variation in magnetic properties (RKKY enhancement, for instance) towards the sample surface.

5.1.3.1 SQUID Magnetometry

SQUID measurements were performed in a Quantum Design MPMS as a function of temperature and magnetic field. The samples were mounted in two orthogonal directions with respect to the *ab*-plane. The full set of measurements taken are shown in Fig. 5.4. In general, it is seen that the samples behave as soft ferromagnets with the easy axis of magnetisation parallel to the *c*-axis, as judged by measurements as a function of field for orthogonal sample orientations. Hysteresis curves of the $x_n = 0.15$ sample [Fig. 5.4 (a)] measured at 1.8 K show a small coercive field of $H_c \approx 70$ mT with the field applied parallel to the *c*-axis. The saturation magnetisation (reached at ∼1.5 T) is found to be (4.4 ± 0.5) μ_B/Mn. To obtain this value, the measured magnetisation data (in e.m.u.) has been normalised using the sample's mass and the average elemental composition, as determined earlier by EDX. This approach assumes the only source of magnetic moment is the Mn itself. This is a reasonable assumption in this case and magnetisation data is also obtained at 300 K (not shown) to demonstrate that no ferromagnetic impurities have been introduced through sample handling. Later, XMCD will also provide element selectivity for the magnetic properties. The $x_n = 0.09$ sample shows a more complicated behaviour as a function of field, as shown in Fig. 5.4(c). The sample shows a 'double-step' behaviour for measurements along the magnetic hard axis. The first step saturates at (3.5 ± 0.4) μ_B/Mn, before reaching a full saturation value of (5.0 ± 0.5) μ_B/Mn. For all of these values, the stated uncertainty is dominated by error within the compositional analysis.

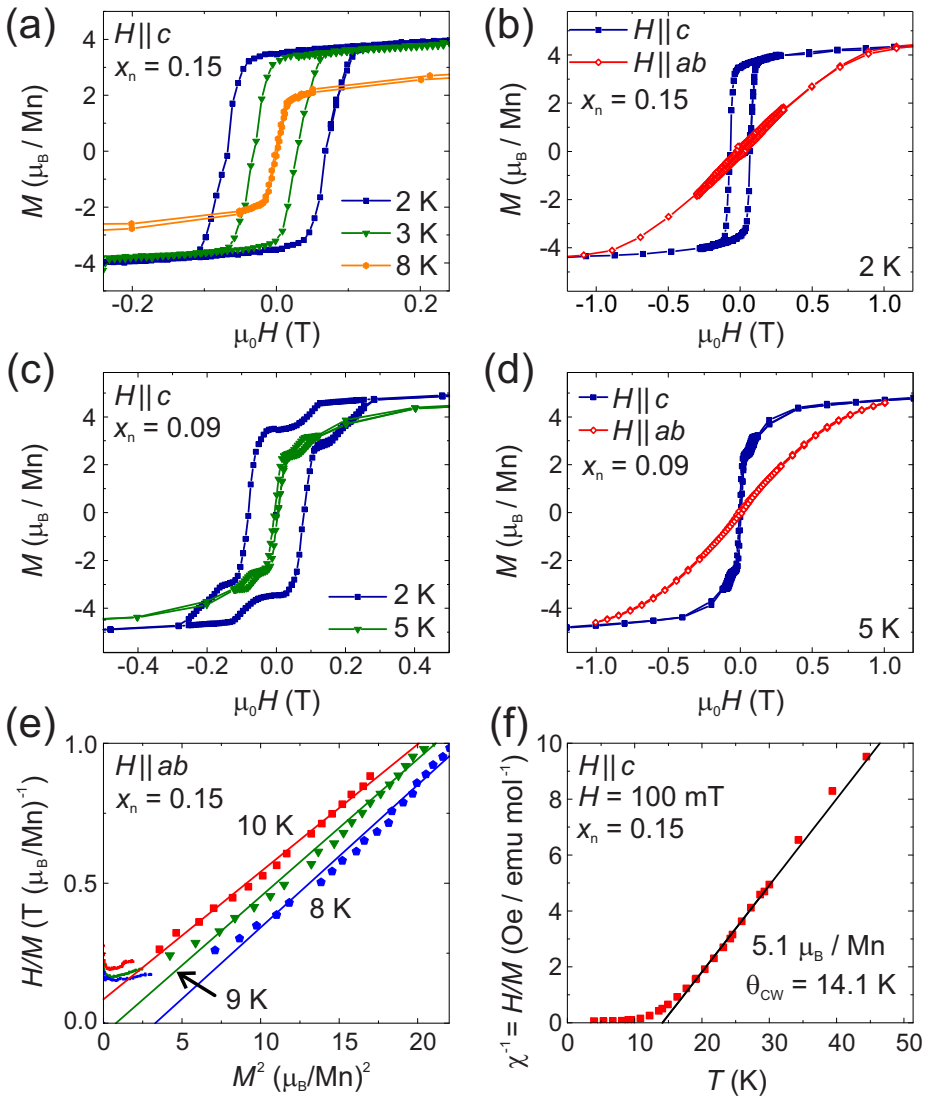

Figure 5.4: SQUID magnetisation measurements of Mn-doped Bi_2Te_3 single crystals. (a) Magnetisation as function of field of a $x_n = 0.15$ crystal with the magnetic field applied parallel to the c-axis, with a saturation moment of 4.5 ± 0.4 μ_B/Mn at 2 K. (b) Hysteresis loops obtained with the applied parallel and perpendicular to the c-axis, showing an easy axis of magnetisation parallel to the c-axis. (c) Magnetisation as a function of field for a $x_n = 0.09$ crystal at 2 K and 5 K. The sample shows a very clear 'double-step' structure, saturating at a value of 5.0 ± 0.5 μ_B/Mn. (d) Hysteresis loops for the $x_n = 0.09$ crystal, showing similar anisotropy properties to the $x_n = 0.15$ sample. (e) Arrott plot analysis. Extrapolating from the high field data, T_C is found to be between 9 and 10 K for the $x_n = 0.15$ sample. (f) Inverse magnetic susceptibility as a function of temperature for the x_n=0.15 crystal. The solid line is a fit to the Curie-Weiss law in the paramagnetic phase, indicating a transition temperature of 14.1 K. Data from M. D. Watson, figure appears in [22].

The steps observed in the magnetisation curve for the hard axis loop for $x_n = 0.09$ (which also appear in XMCD, later) have been similarly observed in Fe-doped ZnSe [92], and other diluted magnetic semiconductors (DMSs). For Fe-doped ZnSe it was found that the position of the first step in the magnetisation curve is almost insensitive to crystal fields and sample orientation. Further, it was shown that it can be used to determine the nearest-neighbour coupling constant, J_{NN} [92]. It is possible, given that this behaviour occurs only for the $x_n = 0.09$ sample, that this effect is related to the mixed substitutional and interstitial doping mode, with Mn dopants in each lattice site saturating at different values. The measured saturation magnetisation of (4.4 ± 0.5) μ_{B}/Mn is found to be between the expected value for high spin Mn^{3+} (4 μ_{B}) and Mn^{2+} (5 μ_{B}). It is consistent with calculations which give 4 μ_{B} [93] and 4.5 μ_{B} [94], respectively. However, these results disagree with previous reports on $x_n = 0.09$ crystals, which give a saturation magnetisation of 1.5 μ_{B}/Mn [87].

Figure 5.4(e) shows the extraction of the paramagnetic-ferromagnetic transition temperature, T_C, by following Arrott's method [95] for the $x_n = 0.15$ sample. This method follows a Landau approach, and says that above hysteresis limits the magnetisation will be of the form,

$$H/M = a(T - T_C) + bM^2 + cM^4, \tag{5.1}$$

where H is the applied field, M the measured magnetisation, T the sample temperature and T_C the transition temperature. a, b and c are free parameters for the fit. From this equation it is evident that the sign of the y-intercept will change either side of T_C. So, by measuring field sweeps at various, fixed temperatures, a determination of T_C may be made from linear fits to the high field data, extrapolated to the intercept. It is clear from Fig. 5.4 that this value lies between 9 and 10 K in this case, a

more detailed fit places this value at $T_C \approx 9.4$ K.

An effective moment of (5.1 ± 0.5) μ_B/Mn is extracted from the high temperature susceptibility data (for the $x_n = 0.15$ sample), with the applied field perpendicular to the c-axis, using a Curie-Weiss law fit, as shown in Fig. 5.4 (f). This value is greater than the $\sim$4 μ_B/Mn reported by Hor *et al.* [87]. Again, the value of the magnetic moment is between the anticipated effective moments for Mn^{2+} and Mn^{3+}, when assuming only a spin contribution to the measured moment. For Mn^{3+}, $p_{\text{eff}} = 2\sqrt{S(S+1)}$ is 4.9 μ_B/Mn and 5.9 μ_B/Mn for Mn^{2+}. These results imply no significant reduction of the moment, compared with the full paramagnetic moment, contrary to that observed by Hor *et al.* [87], who attributed the reduction of moment to effects associated with itinerant ferromagnetism in the sample. Such a variation between the theoretical and experimental values for the Mn moment have also been observed in the dilute magnetic semiconductor $Ga_{1-x}Mn_xAs$. In that material values of 4 μ_B/Mn for defect free samples and 4.5 μ_B/Mn for samples with interstitial Mn were reported [96].

The hysteresis loops recorded with the field perpendicular and parallel to the crystals' c-axis [Fig. 5.4 (b) & (d)] display a uniaxial anisotropy with the c-axis being the easy axis of magnetisation. For the $x_n = 0.15$ sample, the magnetic anisotropy is found to be $K_1 = 11$ kJ m^{-3}, according to $K_{\text{eff}} = \int_0^{M_S} \mu_0 H \, dM$. Comparatively, $Mn_xGa_{1-x}As$ has a magnetocrystalline anisotropy constant of $\sim$3 kJ m^{-3} [97].

5.1.4 Muon Spin Rotation

μSR experiments were performed at the ISIS pulsed neutron and muon facility on the instrument EMU in collaboration with Z. Salman, PSI - Switzerland and S. Giblin, Cardiff University. Muons are spin-$\frac{1}{2}$ particles that are sensitive to their local magnetic environment. μSR is well suited to the exploration of local magnetic correlations, since the spatial sensitivity of the probe decreases rapidly, giving an effective sampling radius of 20 Å. The energy of the incident muons (4 MeV) gives a bulk

implantation depth of ∼0.5 mm and allows for an estimation of the magnetic volume fraction of the sample. The spin of the muon is anti-parallel to the incoming momentum. Therefore, homogenous internal fields with respect to the muon stopping site lying off this axis give rise to oscillating spectra with respect to the symmetrical detectors in zero field [98]. When the internal field is larger than ∼60 mT the oscillations can no longer be resolved at the ISIS pulsed source and the fast frequency results in a missing asymmetry fraction, whereas any ordered moments aligned along the muon polarisation axis result in an observable non-relaxing tail. For Mn-doped Bi_2Te_3 in zero field there is a missing asymmetry below T_C due to a large internal field resulting from a precession frequency which is too fast to be resolved at the ISIS pulsed source. This is in contrast to Fe-doped Bi_2Se_3, which has a lower internal field at the muon stopping site [99]. However, weak transverse field (with respect to the muon spin) experiments can be performed which allow for the calculation of the magnetic volume fraction.

Samples were mounted by nominally aligning the crystals in a mosaic with their c-axis along the direction of the incoming muon spin on a hematite backing plate. In the temperature range of interest hematite is an ordered magnet with internal fields too large to be resolved. Therefore, when a transverse field is applied only a flat background is observed. Figure 5.5 (a) shows the spectra recorded for the $x_n = 0.15$ sample at 20 K and 2.3 K, above and below T_C, respectively. The spectra can be fitted with a function of the form:

$$A(t) = A_1 \exp(-\lambda_i t) \cos(2\pi \upsilon_i t) + A_{\mathrm{NO}} \ , \tag{5.2}$$

where A_1 represents the relative contribution for those muons undergoing coherent precession, A_{NO} is the non-precessing signal amplitude due to a local field distribution parallel to the initial spin polarisation of the muon, λ is the relaxation rate and the

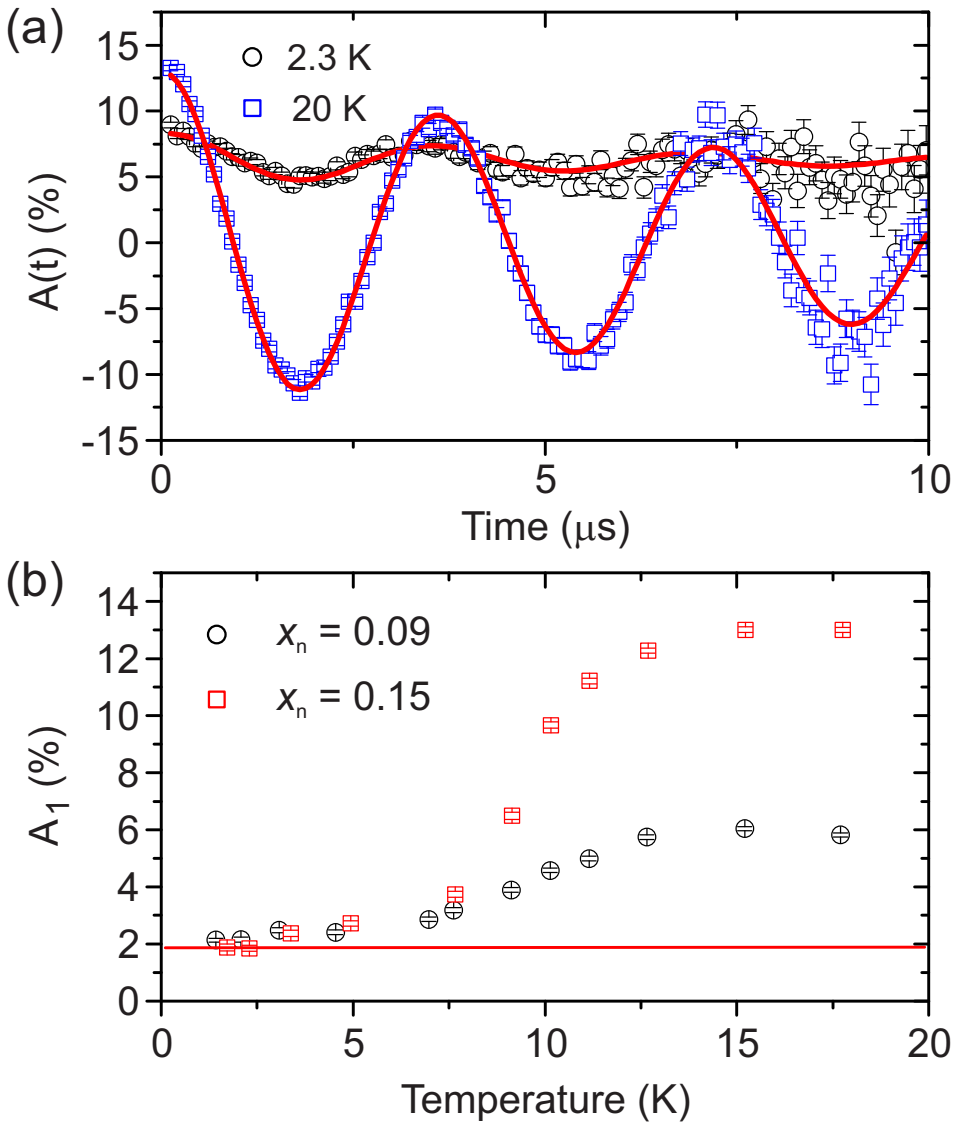

Figure 5.5: Muon spin rotation measurements on Mn-doped Bi_2Te_3. (a) Total asymmetry plotted as a function of time for the $x_n = 0.15$ sample. The solid red lines are fits to the data. (b) The amplitude A_1 of the oscillating component in Eq. 5.2, as a function of temperature for both the $x_n = 0.15$ and $x_n = 0.09$ sample. The horizontal red line represents the signal from the hematite backing plate. A_1 drops down to the background level which suggests that the full volume fraction of both samples is magnetically ordered. Figure appears in [22].

frequency of the oscillations, υ_i can be expressed by $\upsilon_i = \gamma_\mu |B_i|/2\pi$, where B_i is the average magnitude of the local field at the i^{th} muon site and γ_μ is the muon gyromagnetic ratio. Above T_C the detected signal is composed of muons stopping in the sample and a small background component of muons stopping in the loss pipe behind the cryostat rather than the hematite backing plate. However, below T_C, A_{NO} increases as the applied field of 2 mT is smaller than the randomly oriented internal static fields (> 60 mT), which may have a component along the direction of the incoming muon spin. In this case, the only oscillating component is from the instrument background, i.e., muons stopping in the cryostat tail. To confirm this, measurements were performed with only the hematite backing plate and the amplitude of the oscillating component is shown as a horizontal red line in Fig. 5.5 (b). Figure 5.5 (b) shows the temperature dependence of A_1 for both the $x_n = 0.09$ and $x_n = 0.15$ Mn concentrations. In both cases the signal from the sample vanishes below T_C, suggesting a full volume fraction of magnetisation. The difference in the initial asymmetry between the two samples above T_C is simply a consequence of the mass of sample material used, with the $x_n = 0.09$ sample having a smaller stopping area. Fitting a critical type behaviour to both λ and A_{NO} gives an estimation of $T_C \approx 9.5$ K for both samples, in good agreement with the bulk SQUID measurements.

5.1.5 XMCD Measurements

XMCD is used to probe the local electronic character of the magnetic ground state of these samples in an element selective manner [54]. This technique allows an unambiguous determination of the electronic and magnetic state of magnetic dopants in TIs [100, 101, 102, 103, 104].

X-ray absorption spectra (XAS) of $x_n = 0.09$ samples were obtained in the temperature range from 1.8 K to 200 K on beamline I06 at Diamond Light Source using

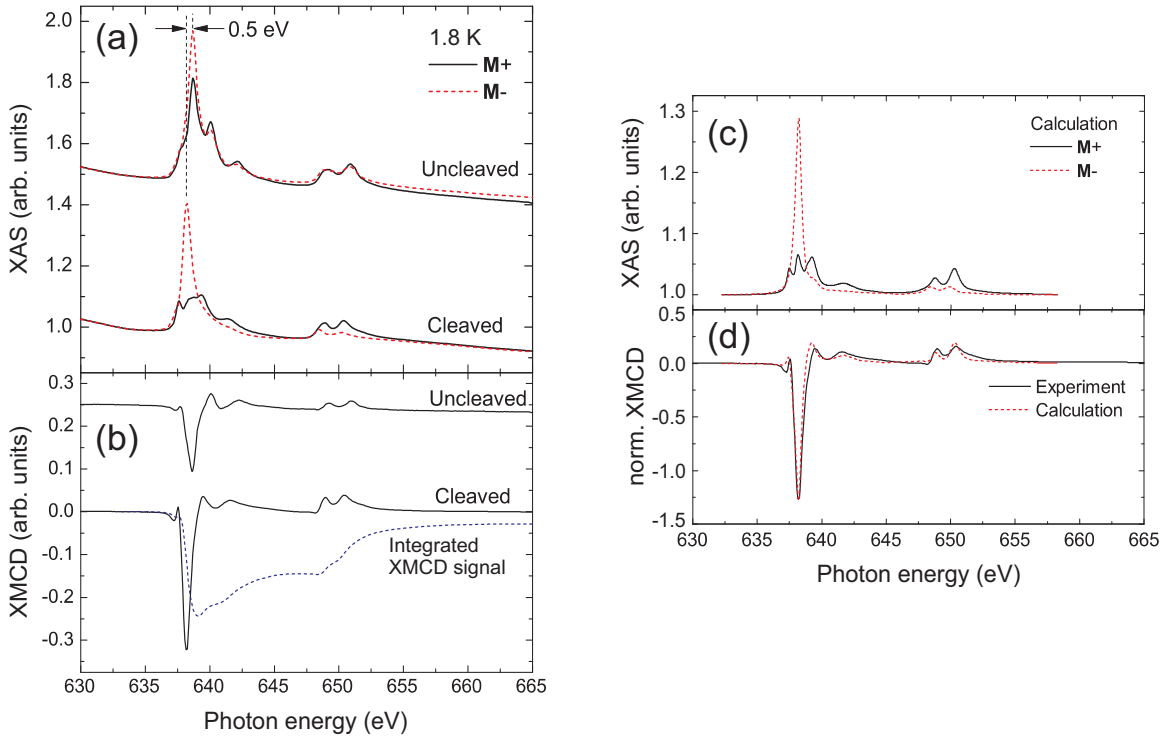

Figure 5.6: (a) Mn $L_{2,3}$ XAS and (b) XMCD spectra of uncleaved and *in-situ* cleaved Mn-doped Bi_2Te_3, $x_n = 0.09$, at 1.8 K. The solid and dashed XAS curves correspond to positive and negative magnetic fields, respectively, of 6 T perpendicular to the surface. Cleaving of the sample gives a shift of -0.5 eV in the photon energy of the Mn L_3 peak maximum and changes the multiplet structure in the XAS spectra, while features in the XMCD signal are less affected. The integrated XMCD signal from the cleaved sample is also shown (dashed line). (c) Calculated XAS spectra for Mn with opposite magnetisation for 100% circularly polarised x-rays. (d) Direct comparison of experimental and calculated XMCD normalised to the maximum average XAS. Figure appears in [22].

a superconducting magnet capable of applying fields up to 6 T along the direction of the incident x-ray beam. The degree of circular polarisation of the x-ray beam delivered in the energy region of interest is close to 100%, and the spot size of the beam is typically 20×200 μm^2, much smaller than the area of the crystal surfaces. XAS measurements were made in total-electron-yield (TEY) mode, which is surface sensitive (with an exponentially decaying sampling depth of 3-5 nm). Clean sample surfaces were obtained by *in-situ* cleaving under ultra-high vacuum conditions ($< 10^{-10}$ Torr). The XMCD is obtained from the difference between two XAS spectra recorded with

x-ray helicity vector and applied magnetic field parallel and antiparallel, respectively.

Figure 5.6 (a) shows the Mn $L_{2,3}$ XAS spectra before and after *in-situ* cleaving measured in a 6 T field at 1.8 K. The surface previously exposed to air displays a distinct multiplet structure that is characteristic of a highly localised ground state [105]. After cleaving of the crystal, the multiplet structure becomes less pronounced and the Mn L_3 peak maximum shifts by ∼0.5 eV to lower energy. A similar observation was made for the DMS $Ga_{1-x}Mn_xAs$, where the energy shift and the different multiplet structure after cleaning indicated that the Mn ground state has a mixed d^4, d^5, and d^6 character [105]. From Fig. 5.6 it is clear by inspection that the $L_3/(L_3 + L_2)$ branching ratio (L_3 and L_2 stand here for the integrated peak intensities) is higher than the statistically expected value of 2/3. This is an indication that, to a large extent, the Mn d electrons are localised rather than itinerant [106, 107]. Figure 5.6 (b) shows the corresponding XMCD spectra. The XMCD asymmetry is normalised by taking the background of the XAS spectra equal to 1. For the uncleaved crystal the XMCD resembles the multiplet splitting of the atomic Mn d^5 configuration [108]. After cleaving the XMCD becomes more intense and shows a sharper and somewhat different multiplet structure. The XMCD of the cleaved crystal arises from a mixed ground state [107, 109].

5.1.5.1 Spin and Orbital Moments from XMCD

Application of the sum rules [58] allow for the extraction of the ratio of the orbital to spin magnetic moments from the integrated intensities of the L_3 and L_2 edges in the XMCD spectrum. In Mn, the $L_{2,3}$ edge has a large jj-mixing between the $2p_{3/2}$ and $2p_{1/2}$ core levels and so a correction factor (determined as 1.47 by comparing calculated specra with the ground state magnetic moment) must be applied when using the sum rules [109]. The integrated XMCD signal from the cleaved sample shown in Fig. 5.6 (b) gives, after the mentioned correction, an orbital to spin moment ratio

of $m_L/m_S = 0.043$, confirming the expected large spin- and small orbital-magnetic moment. For a magnetic ground state of mainly d^5 character the contribution of the magnetic dipole term, T_z (which accounts for inhomogeneity in the spin magnetisation) is negligible and therefore is ignored during the sum-rule calculation. Since the derived m_L and m_S have the same sign the spin and orbital moments are parallel, which according to Hund's third rule means that Mn has a more than half filled d shell.

In addition to using the sum rules, it is also possible to extract quantitative information from XMCD spectra by comparing the measured spectra directly with the results from atomic multiplet theory calculations. The atomic multiplet calculations presented here were performed by G. van der Laan. These calculations circumvent the problems outlined above regarding the large jj-mixing as well as other ambiguities present in the sum rule analysis. For an atomic many-electron system, the transitions $3d^n \rightarrow 2p^5 3d^{n+1}$ are calculated using multiplet theory, in which spin-orbit and electrostatic interactions are treated equally. An overview of this theoretical approach is given in Ref. [110]. The exact manner in which the multiplet spectra are calculated (using Cowan's atomic Hartree-Fock code) is given in Ref. [57].

Figure 5.6(c) shows the calculated results for a mixed ground state with 16% d^4, 58% d^5, and 26% d^6 character, which gives an average total d electron count of 5.1. Figure 5.6(d) shows a comparison of the calculated and experimental XMCD, where the magnitudes of the spectra are normalised to the maximum of the average XAS. Compared to the purely atomic d^5 configuration, the Anderson-impurity-model calculation for the mixed state gives an energy shift of -0.5 eV. This shift arises from the additional screening from the increased mobility of the d electrons, in good agreement with the experimentally observed energy shift. The calculation gives a ground state with spin moment of (4.3 ± 0.3) μ_{B}/Mn atom and orbital moment of (0.16 ± 0.02) μ_{B}/Mn atom. The best agreement between experimentally measured

and the calculated spectra of the XMCD amplitude is obtained for the Mn being 100% magnetically polarised. Confirming the earlier results from SQUID (showing a full moment of saturation) and of μSR which demonstrated a uniform magnetisation within the sample volume. The calculated total d electron count of 5.1 (i.e., more than half filled d shell) is consistent with the result derived from the sum rule analysis that spin and orbital moments are parallel (i.e., $m_L/m_S > 0$), according to Hund's rules.

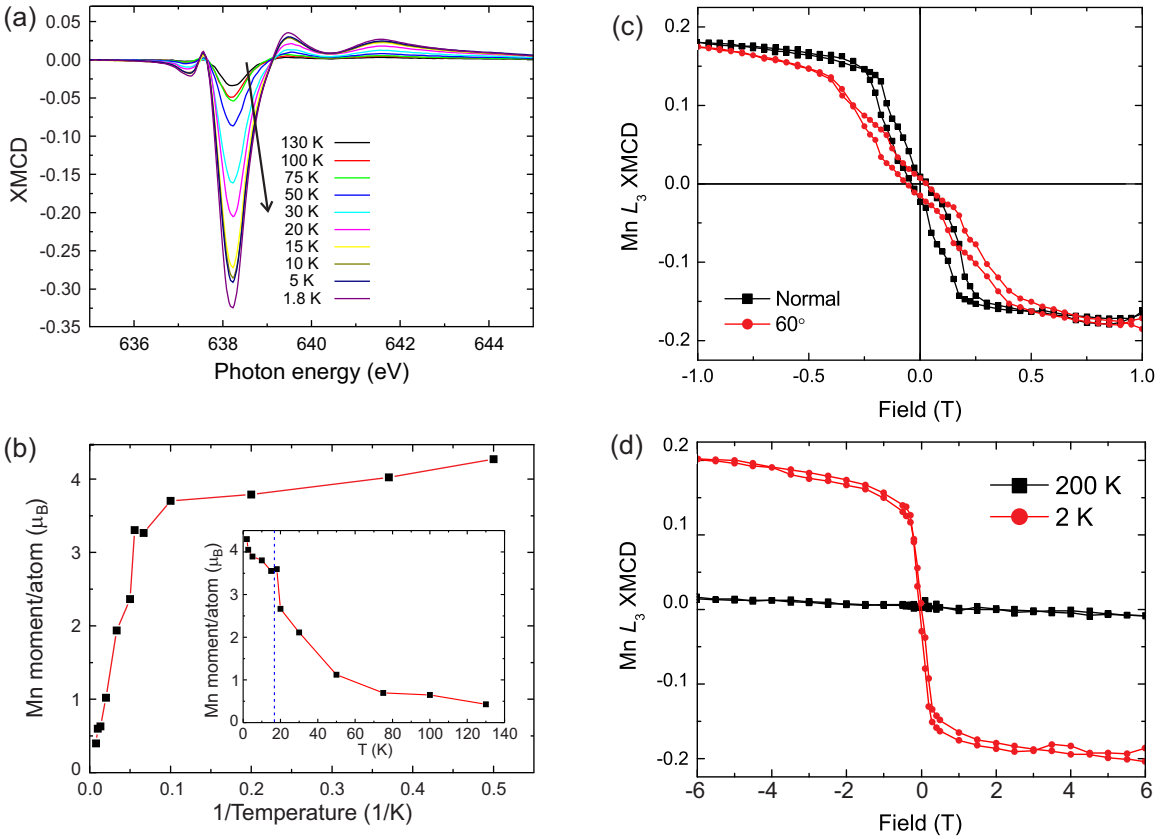

Figure 5.7: (a) Mn L_3 XMCD in a magnetic field of 6 T for the indicated temperatures. (b) The Mn magnetic moment/ion derived using the Mn L_3 XMCD peak asymmetries in (a) as a function of inverse temperature, and directly of the temperature (inset), showing a ferromagnetic to paramagnetic phase transition at $T \approx 16$ K. (c) Hysteretic Mn L_3 XMCD recorded at 1.8 K with the field applied normal to the sample and at an angle of 60°. The gap opening of the loops indicates a ferromagnetic order at low temperature, in which the preferred axis of magnetisation is normal to the surface. (d) XMCD hysteresis for ±6 T field scans applied normal to the sample surface at 200 K and 1.8 K. Figure appears in [22].

5.1.5.2 Temperature Dependence

Figure 5.7(a) shows the Mn L_3 XMCD measured with an applied field of 6 T at a range of different temperatures. With increasing temperature, the spectral shape of the Mn $L_{2,3}$ XMCD remains the same, and there is no energy shift, which suggests that there is only one kind of magnetic Mn ion present. It is clear that a non-vanishing Mn magnetic moment persists up to temperatures well above 100 K. A recent ARPES, magnetometry, and XMCD study [104] on MBE-grown, Mn-doped Bi_2Se_3 thin films reported ferromagnetic order at $T = 45$ K at zero field after applying a magnetic field of 0.5 T along the surface normal, although this result is not confirmed by work presented later in this chapter on similar samples.

The temperature dependence of the magnetic moment obtained from the Mn XMCD asymmetries is shown in the inset of Fig. 5.7(b), and, to further highlight the observed phase transition, it is also plotted as a function of inverse temperature in the main panel. Above $T \approx 16$ K the magnetisation shows the typical temperature dependence for paramagnetic ordering. At the transition around 16 K there is a stark change in slope of the magnetisation curve. Conclusive evidence for ferromagnetic order at low temperature is provided by the hysteresis curve in Fig. 5.7 (c), which is measured at 1.8 K.

In the first instance, such a high transition temperature of $T \approx 16$ K seems surprising since magnetometry resulted in $T_C \approx$ 9-13 K. However, as has been known for some time [114], a ferromagnetic material does not transform instantaneously to the paramagnetic state, but enters a state between ferromagnetism and paramagnetism over a certain range of temperatures above the Curie temperature (the so-called transition region). In a purely ferromagnetic material this range of temperatures is relatively narrow, whereas in alloys and dilute ferromagnetic materials (such as the sample presented here), it is usually considerably broader [115, 116]. Inhomogeneities, clearly observed from EDX and TEM results, within the samples must also

be considered. These inhomogeneities, namely varying Mn concentration, may cause the sample to undergo a phase transition at different temperatures across its volume, depending on the local Mn concentration. This behaviour is consistent with the μSR results, which show an onset of loss of asymmetry at temperatures higher than T_C (Fig. 5.5). To define the boundaries of the transition region, in addition to the ferromagnetic Curie point θ_f, there has been introduced the so-called paramagnetic Curie point θ_p, which fixes the 'upper' boundary of the transition region. The difference, $\theta_p - \theta_f$, increases with increasing concentration of the non-magnetic elements in the material, which leads to an enhancement in the tail of the spontaneous magnetisation.

In the case of a ferromagnetic material near the Curie point an external field causes a strong para-process, resulting in short range ordering of the spins even above the Curie point [114]. Spin density waves have also been claimed to play a role [117], although from evidence presented here such a process may only be speculated. The magnetic field hinders the phase transition from ferromagnetism to paramagnetism. Therefore, one can strictly only speak of a Curie point in the absence of an applied magnetic field. Approaching the Curie point from the high-temperature side, exchange forces begin to play an important role and become sufficient to establish order at short distances, so regions of parallel spins appear, which are essentially local fluctuations of the magnetic order. Averaged over the entire specimen, however, the number of regions with opposite orientations of the magnetisation cancel each other out, and therefore the specimen as a whole does not have any spontaneous magnetisation above the Curie temperature. This will be influenced by the presence of an applied field and the magnetic history, as it favours short-range ordering of spins parallel to the applied magnetic field. Hence, the observed transition point at $T = 16$ K gives the temperature below which an applied field of 6 T induces magnetisation. This transition point is necessarily above the Curie temperature, θ_f. In order to obtain the true Curie temperature one requires measurements across a wider

region of H-T space [95]. This was not pursued, as the T_C had already been obtained by SQUID measurements, in particular by using Arrott's method. The results of the XMCD measured in a limited region of the H-T space are consistent with this result.

5.1.5.3 Hysteresis Loops from XMCD

Sweeping the applied magnetic field at the fixed photon energy of the Mn L_3 absorption peak, an XMCD hysteresis loop can be obtained which reveals the magnetic state of the Mn moments. XAS loops were recorded for both left- and right-circularly polarised x-rays at each value of the applied field. In Fig. 5.7(c), the inset shows XMCD loops recorded in fields up to ± 6 T at 200 K and 1.8 K. The main panel shows the details of the magnetic hysteresis for a smaller field range up to ± 1 T, recorded for two different orientations of the applied field. The magnetisation saturates at $H \approx 0.2$ T and at zero field there is a clear hysteretic opening with finite remanent magnetisation. Loops measured with applied field normal and at 60° grazing incidence to the surface show that the preferred magnetisation axis is along the surface normal (i.e., along the crystalline c-axis), in agreement with SQUID and consistent with measurements on other magnetically doped tetradymites [118].

5.1.5.4 Summary and Conclusions

This section has demonstrated the formation of a ferromagnetic ground state in Mn-doped Bi_2Te_3 crystals grown by solid state methods. The samples show significant inhomogeneities that may limit their usefulness for future devices, which would require high quality single crystals with low defect densities. Nonetheless, the samples show an easy axis of magnetisation along the crystalline c-axis, which is an important step towards our intended goals. This magnetisation acts like an effective field, $\mathbf{B}$, on the spins of the surface-state Dirac fermions. The Hamiltonian of the massive Dirac

model can be written as: [119, 120]

$$\mathcal{H} = \hbar v_{\mathrm{F}}(\sigma_x k_y - \sigma_y k_x) + g\mu_{\mathrm{B}}\mathbf{B}\cdot\sigma \ , \tag{5.3}$$

where v_{F} is the Fermi velocity, $\mathbf{k}$ is the crystal momentum, and $\sigma = \{\sigma_x, \sigma_y, \sigma_z\}$ represents the Pauli matrices, with x and y in the surface plane and z along the normal. The last term represents the Zeeman energy where g is the Landé g-factor. An in-plane field, $B_{x,y}$, shifts the Dirac point, so that there is no opening of a gap, despite breaking the TRS. However, an out-of-plane field, B_z, leads to the opening of a band gap. With the easy-magnetisation direction along the c-axis, as observed here, it is possible to open a surface band gap in the TSS. Therefore, by improving the quality of the grown crystals, with MBE for instance, Mn-doped chalcogenide TIs could be a route into the novel physical effects, and therefore new device applications, anticipated for these materials.

5.2 Mn-doped Bi_2Se_3 Thin Films

Up to this point this chapter has focussed on Mn-doped bulk samples and has demonstrated the formation of a ferromagnetic ground state in these materials. However, there is significant inhomogeneity within the crystals combined with a relatively low solubility limit of the dopant. It may be anticipated that higher dopant solubility along with greater homogeneity may be achieved for thin films grown by MBE, due to the non-equilibrium growth method available.

5.2.1 Motivation

In general, the aim for perfect samples is to achieve a ferromagnetic insulator, i.e., ferromagnetic doping without an increase of the bulk carrier concentration or the formation of secondary phases in the material. Doping of $Bi_2(Se,Te)_3$ compounds into a ferromagnetic insulating state is challenging. The dopants have a tendency to enter the host both substitutionally and interstitially in the quintuple layers, as has been seen for bulk crystals earlier in the chapter. This leads to a number of possible magnetic ordering and chemical bonding scenarios [20, 121]. In terms of their magnetic behaviour, these systems will exhibit multiple magnetic phases, such as in the case of Mn-doped Bi_2Se_3 of ferromagnetic ordering through Mn substitution on Bi or Se sites, antiferromagnetic ordering of Mn ensembles, and paramagnetic behavior of uncoupled Mn ions. Also, free carriers are introduced as a result of non-isoelectronic substitution on Bi or Se/Te sites [20], arising from hybridisation between the transition metal $3d$ state and the Se/Te p state [122], which open up scattering channels for the TSS electrons.

There is little consensus in the literature regarding the magnetic order in the Mn-doped chalcogenide TIs, despite the fact that a uniform distribution of the magnetic ordering is found by polarised neutron reflectometry [88] and muon spin rotation

(c.f. section 5.1.4). For example, in the case of Mn-doped Bi_2Se_3, a nanoscale surface segregation of Mn was found, leading to surface magnetism with a reported transition temperature on the order of 100 K, while it was 5 K for the bulk of the film [89].

To explore the structural and magnetic properties of Bi_2Se_3 thin films as a function of Mn doping concentration, a series of samples were grown by MBE on *c*-plane sapphire substrates. The films show high structural quality as confirmed by AFM and XRD up to a doping concentration of ∼7.5 atomic percent (at.%) Mn. The magnetic properties were investigated by SQUID magnetometry and XMCD. A low transition temperature of 1.5 K was found for 7.5 at.% Mn doping using XMCD. The magnetic moments, as determined by the bulk-sensitive SQUID magnetometry and surface-sensitive XMCD, disagree considerably; possible origins of this observation are discussed. The work presented in this section has been published as Ref [23].

5.2.2 MBE Growth of Mn-Doped Bi_2Se_3

Thin films of Mn-doped Bi_2Se_3 were grown by MBE using a recipe based on that described in chapter 4. Samples were deposited on solvent-cleaned *c*-plane sapphire in a growth chamber with a base pressure of 1×10^{-10} Torr. The films were grown for a range of nominal doping concentrations from 2.5% up to 25% Mn, measured with an *in-situ* beam flux monitor with respect to the Bi flux. The typical film thickness was ∼25 nm. Standard effusion cells were used for the co-deposition of Bi and Mn; Se was sublimated from a bespoke hot-lip cracker source. All evaporation materials used were of 99.9999% purity and the films were deposited in a Se-rich environment to reduce the formation Bi_{Se} anti-site defects (a swap of Bi and Se atoms on their relevent lattice sites) and Se vacancies. Growing with a Bi:Se flux ratio of 1:10, the deposition rate was Bi-limited at ∼0.4 nm/min. Nominal Mn-doping concentrations were adjusted using the Mn:Bi flux ratio, as measured by the BFM.

Films were deposited at a constant substrate temperature of 200°C, then cooled

under a residual Se background to room temperature (25°C) for the deposition of a Se capping layer to protect the surface against oxidation. The low growth temperature and residual background whilst cooling inhibit defect formation in the film. Please note that in this case a higher temperature anneal step is not used, as it was previously. This is done in an attempt to limit unwanted reaction or diffusion of the Mn dopant.

5.2.3 Structural Characterisation

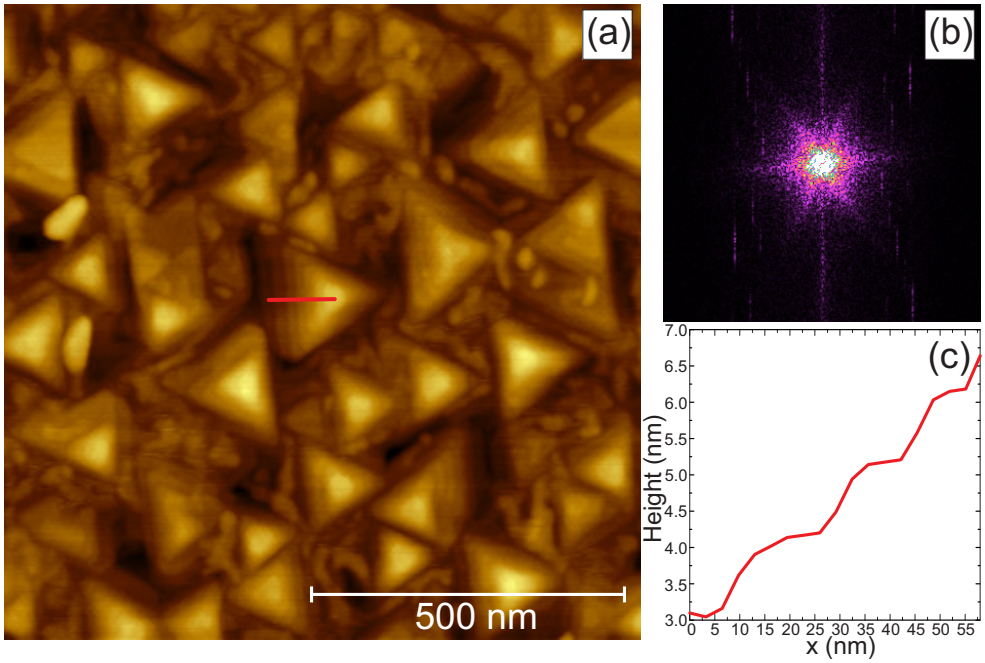

Figure 5.8: (a) AFM of a 29-nm-thick Bi_2Se_3 film with 7.5 at.% Mn doping. The typical triangular growth islands with ∼1 nm high quintuple layer steps, common for undoped Bi_2Se_3, are found. Red line indicates a linescan across the image. (b) Fourier Transform (FFT) of the acquired AFM image demonstrating the 3-fold symmetry (plus twin domains) in the $R\bar{3}m$ space group. (c) Linescan across terraces shown in (a) and demonstrating the quintuple layer steps of ∼1 nm height.

AFM studies were performed using a tapping-mode AFM (Veeco Multimode V). The AFM image [Fig. 5.8 (a)] indicates a growth mode that is characteristic of the Bi_2Se_3 material system, showing spiral growth with terraces of 1 quintuple layer (QL) in height. This morphology is qualitatively similar to that previously observed in

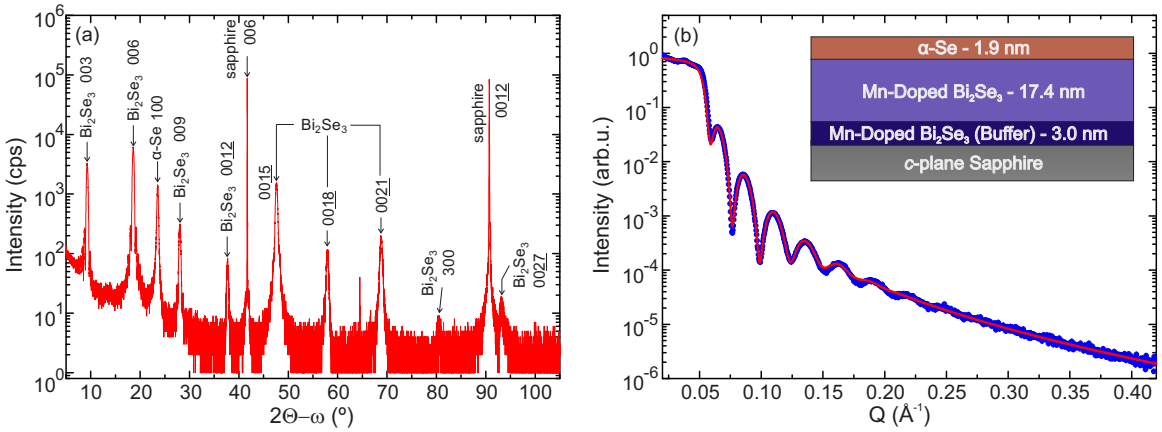

Figure 5.9: X-ray measurements for a 7.5 at.% Mn-doped Bi_2Se_3 thin film sample. (a) XRD shows good out-of-plane order, $(00l)$ parallel to surface normal. By fitting the data the c-axis lattice parameter was found as 28.63±0.01 Å. (b) X-ray reflectivity (XRR) measured (blue dots) with fit performed in GenX (red line) revealing good surface quality of the film. Thickness is found as 20.4 nm with surface roughness of 2.26 nm. Inset shows a schematic of the film structure obtained by the GenX fitting.

undoped thin film samples (c.f. Fig 4.3). Figure 5.8 (b) shows a FFT of the measured data, from which the 3-fold symmetry of the $R\bar{3}m$ crystal class is clearly visible (plus twin domains). The RMS surface roughness is calculated as (1.78 ± 0.24) nm over a 1 μm^2 scan area.

X-ray studies were carried out using a Rigaku SmartLab XRD set with incident Cu-$K\alpha_1$ radiation. Out-of-plane x-ray diffraction [Fig. 5.9 (a)] reveals good crystalline quality with the surface normal aligned on the $(00l)$ diffraction planes. Rietveld refinement of the diffraction pattern is performed in Fullprof. This indicates a lattice parameter $c = (28.63 \pm 0.01)$ Å, in close agreement with the expected parameter of $c = 28.636$ Å (ICSD 617072) and in-keeping with a broadly substitutional doping mode. This slight reduction in c-axis lattice parameter is consistent with substitutional doping on the Bi site due to the smaller ionic radius of either Mn^{2+} or Mn^{3+} compared with Bi^{3+}. An additional α-Se peak is seen in Fig. 5.9 (a) as a result of the surface capping layer, which has no impact on the underlying film.

The XRR, shown in Fig. 5.9 (b), was modeled using GenX to determine film

parameters such as thickness and surface roughness. A schematic of the film structure simulated is shown as an inset to the figure. For the modelling, the Bi_2Se_3 layer is split in two and the density is allowed to vary at the substrate interface to account for possible interfacial effects. It is found that the best fit is obtained by allowing a slight increase in density close to the substrate interface. There is no significant improvement to the model when using more than two layers in the simulation. The model reveals a total Mn-doped Bi_2Se_3 layer thickness of 20.4 nm, consisting of a 3.0 nm thick buffer and 17.4 nm thick functional layer, with a surface roughness of $\sigma = 2.26$ nm, comparable to that found by AFM. The α-Se cap is 1.9 nm in thickness.

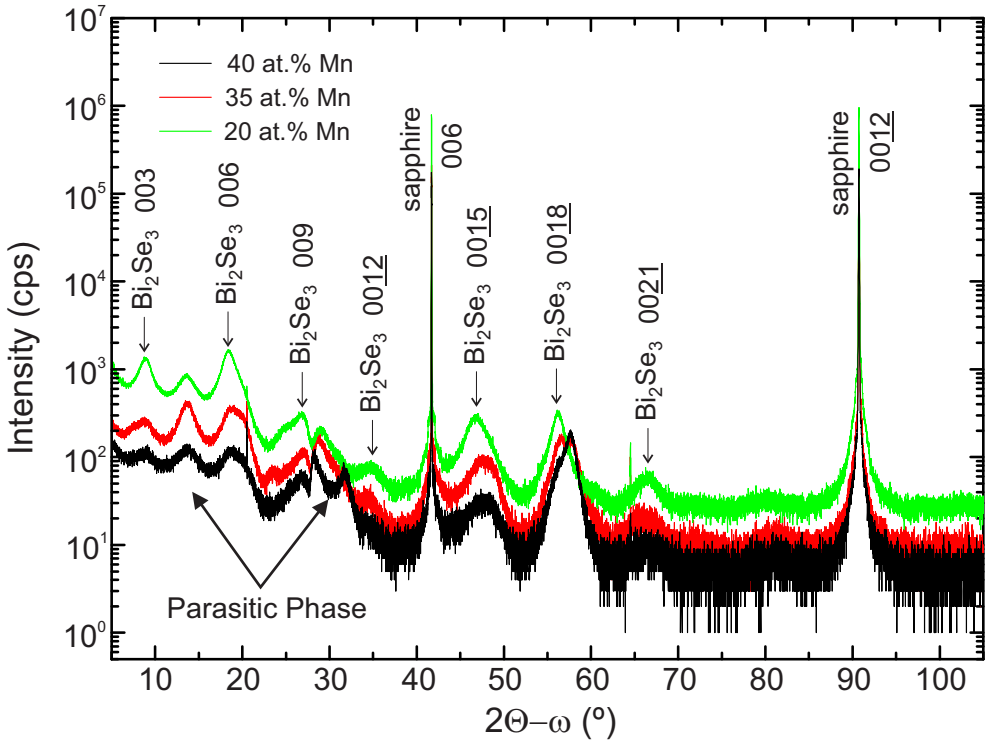

Figure 5.10: XRD of higher doping levels of Mn-doped Bi_2Se_3 thin films. There is significant broadening of the $(00l)$ Bi_2Se_3 peaks as well as peaks developing from a parasitic phase. The observable Bi_2Se_3 peaks have been indexed and the peaks arising from the parasitic phase are highlighted.

Additional samples are also grown to push the limits of doping concentration and

Table 5.1: Possible parasitic phases present in the sample. Data are received from ICSD.

Material	First Peak	Second Peak
Mn-β	(110) - 19.900°	(220) - 40.396°
MnSe	None	(100) - 28.799°
$MnSe_2$	None	(200) - 27.768°

investigate the impact on the crystal structure. The XRD for these over-doped samples are shown in Fig. 5.10. The diffraction spectra indicate a significant degradation to the crystalline order of the (003) family of Bi_2Se_3 diffraction peaks as well as the formation of parasitic phases giving rise to additional diffraction peaks. These additional peaks likely originate from the Mn clusters within the van der Waals gap as well as the formation of Mn containing compounds with Bi and Se. The observed parasitic peaks, labelled in the figure, at ∼14° and ∼30° could arise from a number of sources, summarised in Tab. 5.1. From the limited data it is not possible to conclude the precise nature of the parasitic phase, especially when considering the possibility that lattice constants may be altered through strain. Such strain would not be inconceivable for Mn clusters within the van der Waals gap. The large increase in peak width compared with optimally doped samples indicates a high degree of disorder in the films arising from inhomogeneities across the probe area. This observed disorder along the *c*-axis lattice direction further supports the hypothesis of inhomogeneous clustering of Mn within the van der Waals gap. Due to the significant disorder present in the films, no fit using Fullprof was possible and as such no lattice parameter has been extracted for these films.

The elemental sample composition was determined by RBS measurement, performed by A. Pushp and A. J. Kellock at IBM, Almaden Research Center. It was found that the Mn doping concentrations ranges from 0 at.% up to 20.7 at.%, scal-

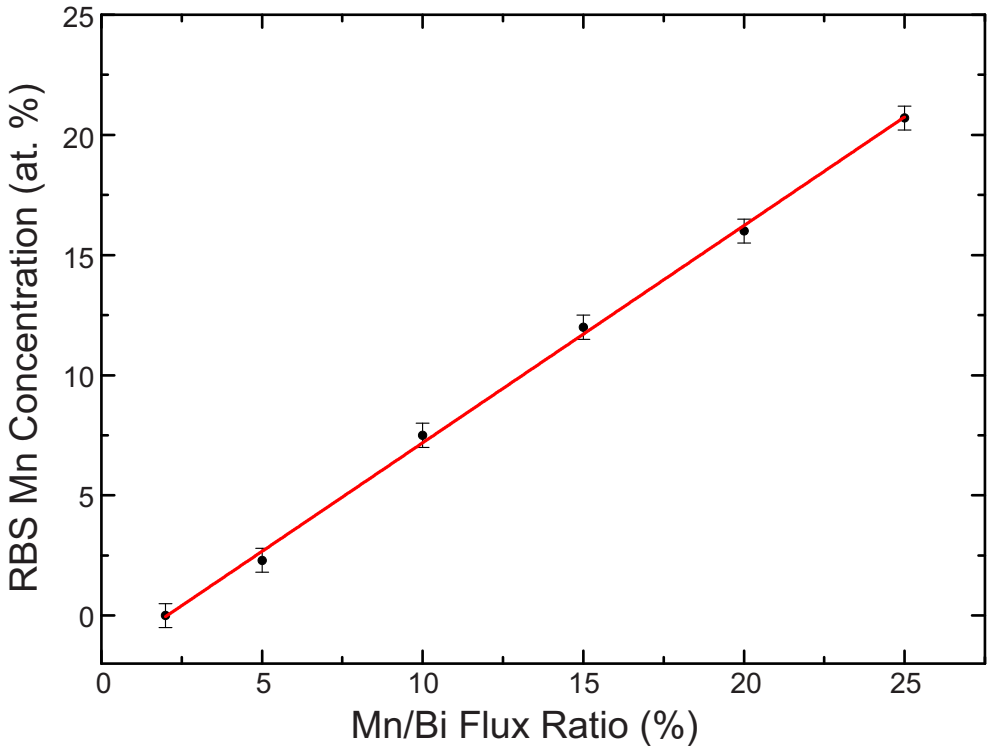

Figure 5.11: Elemental compositions obtained by RBS compared with Mn:Bi flux ratio determined by BFM. The red line is a linear fit to the data, indicating a strong correlation. This correlation allows a straightforward conversion for future samples from beam flux to elemental composition.

Table 5.2: Mn doping percentage obtained from RBS measurements compared with doping percentage determined by Mn:Bi flux ratio (*in-situ*). Uncertainty in RBS measurements is ±0.5 at.%. Both Bi and Se concentrations reduce for increasing Mn doping concentration, indicating a mixed substitutional and interstitial doping scenario.

Nominal Mn doping concentration (%)	RBS doping concentration (in at.%)		
	Mn	Bi	Se
2	0	37.1	62.9
5	2.3	37.8	59.9
10	7.5	34.1	58.4
15	12.0	30.6	57.4
20	16.1	27.0	56.9
25	20.7	23.6	55.7

ing linearly with the nominal concentration obtained from the flux ratio (Fig. 5.11 and Tab. 5.2), with the BFM value systematically predicting a higher concentration than measured by RBS. It was also found that both the measured Se and Bi at.% reduce with increasing Mn doping concentration, indicating a mixed substitutional and intercalated doping scenario. These results indicate an excellent correlation between compositions derived from RBS versus those from BFM. If it is to be assumed that values from RBS are the 'true' atomic compositions, then this relationship allows for a direct conversion from nominal doping (from BFM) to the real elemental stoichiometry.

5.2.4 SQUID Magnetometry

Magnetisation measurements were carried out at 2 K using SQUID (Quantum Design MPMS). The sample was mounted with the field applied in-plane ($\perp c$). The 7.5 at.% Mn-doped sample shows a response typical of a soft ferromagnet at low field (Fig. 5.12), but without discernible coercivity. The sample reaches 80% of the saturation magnetisation at an applied field of 0.2 T. It then exhibits more paramagnetic-

like behaviour, not reaching full saturation until 4 T, consistent with previous studies [123]. This effect is attributed to the continuous reorientation of magnetic domains in the field and is likely linked to structural domains within the crystalline film. A similar effect is also seen in samples doped with Cr (c.f. chapter 6).

The sample is found to have a saturation magnetisation of (5.1 ± 0.5) μ_B/Mn. The moment is calculated using measurements of the sample mass along with values of Mn concentration from RBS; the stated error is dominated by the uncertainty in the determination of composition. The measured saturation moment matches closely with the expected value for Mn^{2+} (5 μ_B), rather than high spin Mn^{3+} (4 μ_B) naively expected for substitutional, isoelectronic doping onto the Bi site. These findings are consistent with the results presented earlier for bulk crystals of Mn-doped Bi_2Te_3.

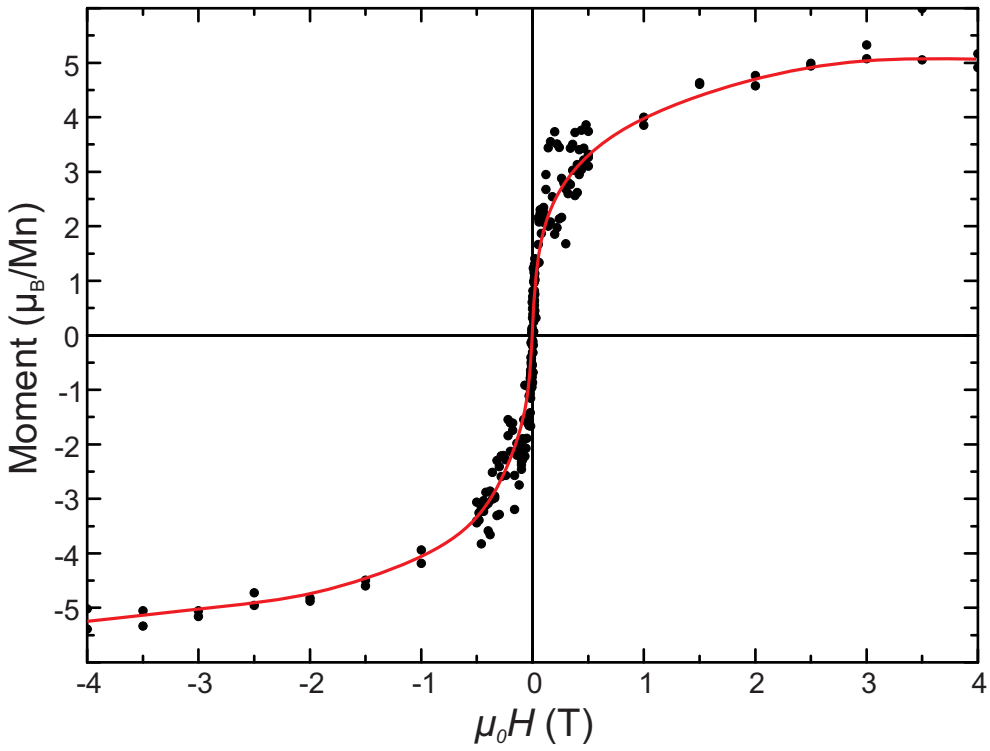

Figure 5.12: Magnetisation curve of 7.5 at.% Mn-doped Bi_2Se_3 thin film measured by SQUID at 2 K with applied field parallel to the *ab*-plane. The sample shows a low-field ferromagnetic response with continuous reorientation at higher fields. The measured saturation magnetisation is (5.1 ± 0.5) μ_B/Mn. The red line is a guide to the eye.

5.2.5 XAS and XMCD

XAS at the Mn $L_{2,3}$ edges was measured in total-electron yield (TEY) detection on beamline I10 (BLADE) at Diamond Light Source. The XMCD spectrum is obtained from the difference between the XAS spectra for x-ray helicity vector anti-parallel and parallel to the applied magnetic field (μ^- and μ^+, respectively). Measurements were taken down to low temperatures ($\sim$2.5 K) in a 14 T superconducting magnet at both normal ($\parallel c$) and grazing ($80°\angle c$) incidence, with the applied field along the incident x-ray beam. The degree of circular polarisation over the energy region of interest is close to 100%. The typical spot size is 20×100 μm^2; much smaller than the sample area. The Mn-doped thin films were introduced into the chamber with an α-Se capping layer, which was removed in-situ by heating to $\sim$420 K for 20 minutes. Its removal was confirmed by a significant enhancement in the edge jump at the Mn $L_{2,3}$ edge. The use of α-Se as a capping layer, combined with the low temperature desorption, limits the out-diffusion of Se from the underlying film.

Figure 5.13 (b) shows the Mn $L_{2,3}$ XAS spectra for the 7.5 at.% Mn-doped Bi_2Se_3 sample measured at normal incidence. The temperature was 2.5 K and a magnetic field of 2 T was applied parallel to the c-axis. The spectrum shows a distinct multiplet structure characteristic of a localised ground state, similar to that seen earlier for uncleaved bulk Mn-doped Bi_2Te_3 crystals (c.f. Fig. 5.6), indicating that some surface modification might have occurred despite the capping layer. The peak shape resembles a Mn ground state of hybridised d^4, d^5, and d^6 character, as it was for bulk samples. The XMCD in Fig. 5.13 (d) was obtained with fixed applied field by reversing the circular polarisation. Qualitatively, the XMCD resembles that obtained previously for cleaved Mn-doped Bi_2Te_3 crystals, indicating that the magnetic order of the underlying material is broadly unaffected by the surface modification.

Quantitative information about the local magnetic moments can be extracted either via the sum rules [58, 124] or by direct comparison of the measured XMCD

with the results of atomic multiplet calculations [109]. The method used here is identical to that of the previous section where x-ray transitions $3d^n \rightarrow 2p^5 3d^{n+1}$ are computed following the methodology of Ref. [57]. Figure 5.13 (a) and (d) show the calculated Mn $L_{2,3}$ XAS and XMCD spectra for a hybridised ground state with 16% d^4, 58% d^5, and 26% d^6 character, which has a spin moment of 4.3 μ_B/Mn and orbital moment of 0.16 μ_B/Mn. Such a ground state is similar to that previously observed in Mn-doped Bi_2Te_3 bulk crystals. The XMCD peak asymmetry, $A = (\mu^- - \mu^+)/(\mu^- + \mu^+)$, is proportional to the ground-state magnetic moment, where the full spin moment (4.3 μ_B) gives $A = -0.58$. The peak asymmetry of the measured Mn-doped thin film [Fig. 5.13 (d)] corresponds to a magnetic moment of 1.6 μ_B/Mn, which is significantly smaller than that obtained from the SQUID results. The TEY detection used here is very surface sensitive (3-5 nm), so that a small amount of non-magnetic or antiferromagnetic Mn at the surface will reduce the overall measured moment. Furthermore, it has been observed for magnetically doped TIs that the surface can have very different properties than the bulk [126]. Fluorescence yield detection is less surface sensitive and therefore better suited for a comparison with the SQUID data. Unfortunately, self-absorption and saturation effects in conjunction with different transition probabilities impede a quantitative determination of the magnetic moment [57].

XMCD measurements were made for a selection of samples with various doping levels, from 0 at.% up to 12.0 at.% Mn as determined by RBS. Figure 5.14 shows the observed dependence of the magnetic moment (measured at $\mu_0 H = 2$ T) at 2.5 K and 10 K, determined from the peak asymmetry in XMCD. It is found that the measured moment per Mn ion increases linearly with increasing dopant level up to an apparent limit at ~7.5 at.% Mn doping. This saturation effect may be ascribed to the solubility limit of the Mn in the Bi_2Se_3 host. Beyond this solubility limit it is likely that Mn incorporates into the crystal structure by forming Mn clusters, e.g., in the van der

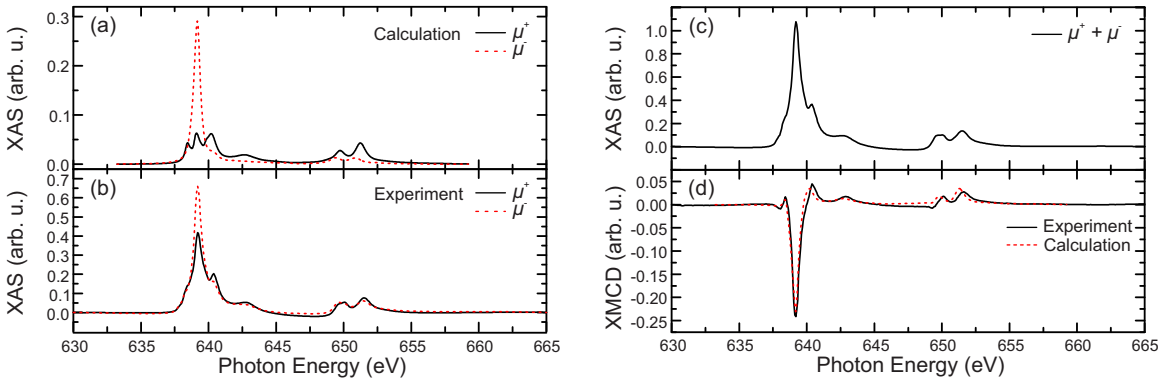

Figure 5.13: (a) Calculated Mn $L_{2,3}$ XAS spectra for left (μ^-) and right (μ^+) circularly polarised x-rays. (b) Measured XAS for left and right circularly polarised x-rays for a 7.5 at.% Mn-doped Bi_2Se_3 sample; obtained at normal incidence, $T = 2.5$ K, and $\mu_0 H = 2$ T. (c) Measured summed XAS ($\mu^- + \mu^+$). (d) Calculated and measured XMCD ($\mu^- - \mu^+$), where the latter is scaled to the calculated peak maximum.

Waals gap, which may order antiferromagnetically. Such a conclusion is supported by XRD studies, which demonstrate the formation of parasitic phases at higher dopings, consistent with clustering in the van der Waals gap. From this result, the sample with 7.5 at.% Mn dopant was selected for detailed investigations, since this sample shows the highest magnetic response without obvious structural degradation. Higher doping levels were also investigated later to understand the effect on the magnetic order of the degradation of crystal quality.

Figure 5.15(a) shows the Mn $L_{2,3}$ XMCD for the 7.5 at.% Mn doped sample, measured at a range of temperatures with out-of-plane applied field of 2 T. Figure 5.15(b) shows the trend in the magnetic moment, extracted using the peak asymmetry, as a function of temperature. An estimation of the Curie temperature may be obtained by plotting the inverse of the magnetic susceptibility (using the moment obtained from XMCD) as a function of temperature [Fig. 5.15 (c)]. This shows the typical linear dependency at higher temperature expected for a paramagnetic system with a deviation at lower temperatures as a ferromagnetic state is formed. Linear extrapolation from higher temperatures leads to an estimated $T_C \approx 1.5$ K, which is

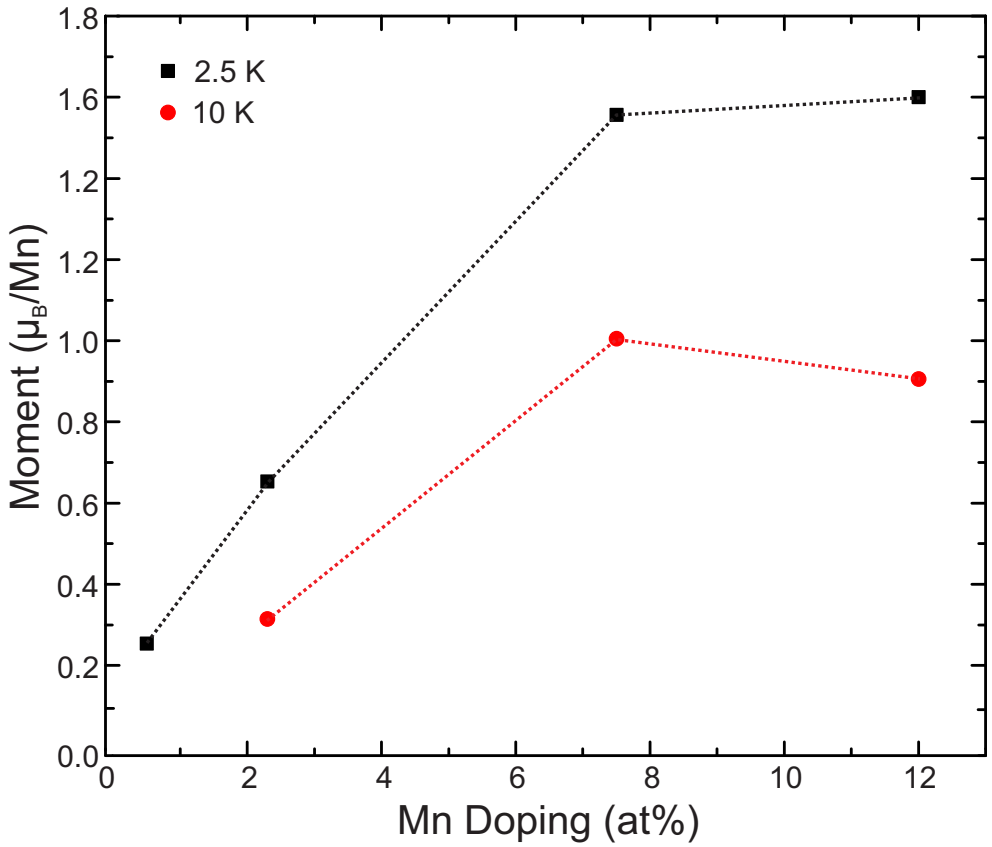

Figure 5.14: Mn magnetic moment determined from Mn L_3 peak asymmetry (at $\mu_0 H = 2$ T) as a function of dopant concentration.

below our lowest reachable measurement temperature.

The XMCD hysteresis is measured at the Mn L_3 edge at normal and 80° grazing incidence [Fig. 5.15 (d)]. The shape of the curves are qualitatively similar to those found by SQUID, with a low-field ferromagnetic-like transition without a discernible open loop, followed by a reorientation at higher fields. It should be noted that the remanence of the 14 T magnet is too high to observe small coercive fields below 50 Oe, which are common for these types of materials. Also, since the measurement temperature of 2.5 K is close to, but above the determined T_C, it is likely that some ferromagnetic domains have formed and are contributing to the overall magnetic order, although the sample has not yet fully reached a ferromagnetic ground state.

XMCD hysteresis measurements were also carried out for samples with higher doping concentrations, where crystallinity has been compromised (c.f. Fig. 5.10). Figure 5.16 shows the XMCD hysteresis measured at normal incidence and $T = 2.5$ K for a 12 at.% Mn-doped thin film. It shows a qualitatively similar response to that of Fig. 5.15 (d), but with a small open loop at low field. This result would indicate that a ferromagnetic coercive field may be introduced by Mn clustering or Mn-based parasitic phases in the film. It is likely, however, that the structural disorder introduced at such doping levels disrupts the TSS [127].

5.2.6 Discussion

From XRD measurements it can be concluded that Bi_2Se_3 can be doped with Mn up to a concentration of roughly 7.5 at.% without loss of structural quality and formation of secondary Mn-containing phases. From RBS measurements of the chemical composition it is clear that dopants are incorporated differently as a function of doping concentration. While the Se concentration is close to 60 at.% for low Mn concentrations, as expected for substitutional doping on Bi sites, it reduces to 55.7 at.%

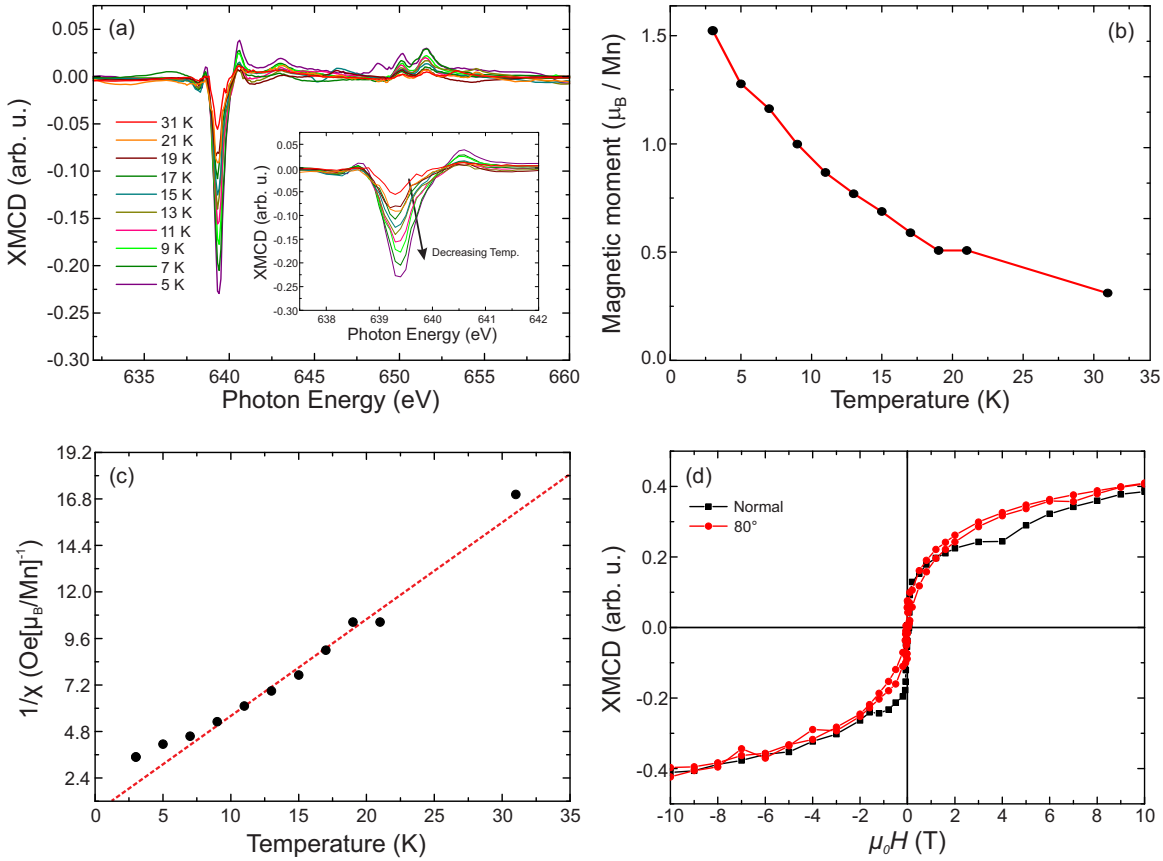

Figure 5.15: XMCD measurements of 7.5 at.% Mn-doped Bi_2Se_3 thin film. (a) Mn L_3 XMCD measured at normal incidence in an applied field of 2 T for a range of temperatures. The inset shows the enlarged peak maxima. (b) Magnetic moment extracted from the XMCD signal measured at the Mn L_3 peak in 2 T field. (c) Inverse susceptibility derived from the XMCD signal. The fit to high temperatures (red line) indicates a transition temperature of $T_C \approx 1.5$ K. (d) XMCD hysteresis at the Mn L_3 edge recorded at 2.5 K with the field applied normal, and at 80°, to the sample surface.

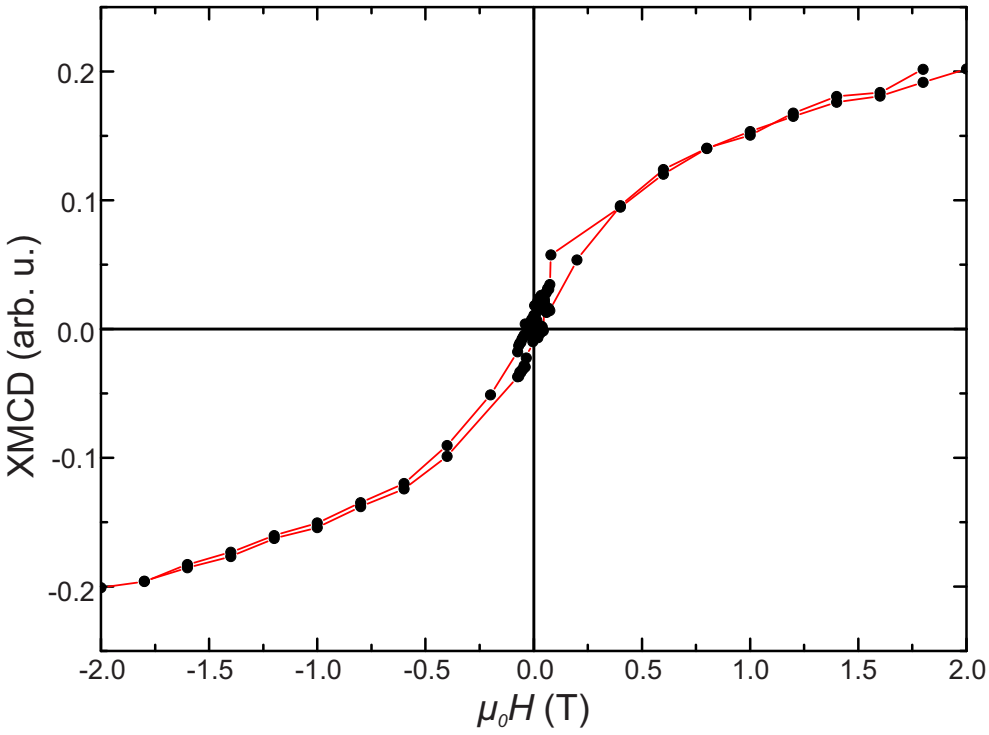

Figure 5.16: XMCD hysteresis at the Mn L_3 edge for a 12 at.% Mn-doped Bi_2Se_3 sample at normal incidence and $T = 2.5$ K.

for a Mn concentration of 20.7 at.%. For this doping concentration the stoichiometry was determined to be $Mn_y(Bi_{1-x}Mn_x)_2Se_3$ with $x = 0.36$ and $y = 0.08$. It may be assumed that Mn_x represents the substitutional doping, Mn_y indicates interstitial incorporation – either within the QL layers or in the van der Waals gap.

Undoped Bi_2Te_3 can either be n-type [36, 128] or p-type [129], depending on whether the growth was under Bi- or Te-rich conditions, as the native point defects, the Bi_{Te1} and Te_{Bi} anti-site defects, are acceptor- and donor-like, respectively [130]. Vacancies, on the other hand, were found to play no role. In Bi_2Se_3, on the other hand, Se vacancies are dominant and lead to n-type doping [131], which is a great disadvantage for thermoelectric applications for which both types of conduction are required [132]. Mn doping has been reported to allow for controlled charge doping with a crossover from n- to p-type above 5% Mn [123]. This behaviour was attributed to the incorporation of divalent Mn which dopes holes into the system to compensate

the electrons resulting from Se vacancies [123]. For Mn-doped Bi_2Se_3, first-principles calculations have shown that the substitutional doping on the Bi site is the energetically most favourable scenario [133], however, leading to metallic, ferromagnetic behaviour. Also, it should be noted that in the calculation, a valence state of 3+ was assumed to keep the doped compound charge neutral, whereas a valence closer to 2+ was calculated [122] and also experimentally observed [123]. The formation energy of Mn_{Bi} was reported to be at least a factor of two lower than the values for Se vacancies, as well as Bi_{Se1} and Se_{Bi} anti-site defects [134]. Also, it should be noted that the incorporation of Mn in the van der Waals gap is low in formation energy and has generally not been accounted for in the theoretical work [135], nor has the interaction of Mn impurities with the native anti-site defects, which are known to be relevant for Mn-doped $Sb_{2-x}Mn_xTe_3$ [136].

A saturation magnetisation of 5.1 μ_B/Mn is obtained from bulk-sensitive SQUID magnetometry, pointing towards Mn being in a 2+ state [high-spin Mn^{2+} d^5 has spin moment 5 μ_B/Mn and a small orbital moment ($\sim$0.1μ_B/Mn)], instead of Mn^{3+} expected for isoelectronic substitution (high-spin Mn^{3+} d^4 has a spin moment of 4 μ_B/Mn). It has to be stressed that unambiguous determination of the Mn valence state, however, is not possible based on SQUID data alone. In general, depending on the details of the Mn incorporation in Bi_2Se_3 such as site distribution and concentration, the system can be either paramagnetic resulting from isolated Mn ions, a spin-glass state resulting from isolated ferromagnetic clusters, or ferromagnetically or antiferromagnetically ordered resulting from exchange coupling. In a recent first-principles calculation study, Vergniory *et al.* [137] have shown that the magnetic long-range interaction is anisotropic. In the plane, the indirect exchange coupling is mediated by free carriers, while the coupling out-of-plane is via the double exchange mechanism through Se. The dominant finding in the literature is that Mn-doped Bi_2Se_3 is either paramagnetic due to uncoupled Mn impurities or exhibits spin-glass

behavior due to isolated ferromagnetic clusters [123, 138, 139].

XMCD reveals the magnetic ground state of the material with a magnetic moment at saturation of 1.6 μ_B/Mn and $T_C \approx 1.5$ K, which is a much smaller moment than measured by bulk-sensitive SQUID magnetometry. Zhang *et al.* [89] and Xu *et al.* [104] found that Mn-doped Bi_2Se_3 films show a low temperature ferromagnetic phase (< 5 K) using bulk techniques, which exhibit surface ferromagnetism up to 100 K, and a reduction of the density of states at the Dirac point, as detected by photoemission and XMCD. The observation of high-temperature surface magnetism was associated with the occurrence of Mn phase segregation in the near-surface regions. However, theoretical work by Rosenberg and Franz [140] suggested that surface magnetism is possible in doped TIs, without the occurrence of an ordered state in the bulk, and that this could be a characteristic of TIs.

A likely scenario that could explain the variation in observed magnetic surface properties are surface and near-surface inhomogeneities. For instance, above room-temperature ferromagnetism has been reported for Mn-doped InAs nanodots [141]. These inhomogeneities will be most likely sparse enough to be undetectable for standard lab-based XRD. One reported inhomogeneity is the Mn nanoislands by Zhang *et al.* [89]. Both in their study, as well as in this work, the as-grown thin film samples were capped by an amorphous Se layer in UHV, before transferring them into another UHV analysis chamber for XMCD or scanning tunneling microscopy studies. This procedure, which involves heating the sample up to a temperature below the growth temperature, will certainly disturb the Mn-doped system as the diffusion rates are known to be high (and highly anisotropic) in Bi_2Se_3, and are even significant at room-temperature [142, 143]. Further, as sample temperatures are rarely calibrated across different growth and analysis systems, the resulting surfaces will be very different and the comparison of results obtained by different studies difficult. It is indeed possible that the decapping process leads to an undesirable alteration

of the near-surface area of the sample, resulting in the observed high-temperature surface magnetism reported by Zhang *et al.* [89], and hence the discrepancy between the measured magnetic moments in the present study. Apart from the formation of Mn islands [89] and antiferromagnetic Mn-Mn coupling, also known from the diluted magnetic semiconductor $Ga_{1-x}Mn_xAs$ [96], the formation of Mn interstitials can lead to an apparent reduction of the magnetic moment per Mn as they are potentially no longer involved in magnetic coupling scenarios.

At this point it is important to mention a recent study by Springholz *et al.* [127], which has cast doubt that magnetic doping is the only mechanism that leads to an experimentally observable band gap in the TSS. Most importantly, impurity scattering is believed to play a more significant role than previously considered, and the band gap may be associated with a topological phase transition from the topological to a non-topological phase [144]. In particular, the band gap observed using angle-resolved photoemission spectroscopy (ARPES) of ∼62 meV (at 45 K) [104] is much larger than the theoretically predicted gap of 16 meV (with a critical temperature of 12 K) [145].

It is clear that the exact nature in which Mn dopants, and other 3*d* impurities, incorporate in the host crystal is complex and still unresolved. X-ray absorption fine structure (XAFS) has previously been used to resolve such questions in Bi_2Se_3 with other 3*d* dopants [20, 121], owing to its ability to study the local environment around impurities in an element-specific way. Such studies are in progress and initially appear to demonstrate an octahedral coordination of the Mn dopant environment (the Bi site), but with some portion of interstitial Mn present at all doping concentrations [146].

5.3 Summary and Conclusions

In summary, the high-quality MBE growth of Mn-doped Bi_2Se_3 thin films has been demonstrated. Structural studies indicate that the samples grow with 3-fold symmetry and with the *c*-axis perpendicular to the surface plane. It is found that Mn dopants may be introduced into the host Bi_2Se_3 without the formation of additional parasitic phases or significant degradation to the host crystal structure up to a doping concentration of ∼7.5 at.% Mn. From the compositional analysis by RBS it is apparent that Mn is incorporated substitutionally for low doping concentrations, before also being incorporated interstitially at higher doping concentrations. A saturation magnetisation of 5.1 μ_B/Mn is obtained from SQUID magnetometry, pointing towards a Mn valency of 2+. The surface sensitive technique of XMCD reveals a measured magnetic saturation moment of 1.6 μ_B/Mn and $T_C \approx 1.5$ K. It is clear that the exact nature in which Mn dopants incorporate in the host crystal is still unresolved. Preliminary EXAFS work [146] indicates that the Mn dopant occupies an octahedral Bi site and that there is relaxation of the corresponding Se bonds due to the reduced ionic radius of the Mn compared with Bi. This result is similar to that shown for Cr in chapter 6, however, even for low dopings of Mn it is seen that the dopant still incorporates into interstitial sites, such as the van der Waals gap.

Chapter 6

Cr-Doped Bi_2Se_3

6.1 Motivation

Recently, the quantum anomalous Hall effect [39] was experimentally observed at zero magnetic field in chromium-doped $(Bi,Sb)_2Te_3$ [12], a magnetic, three-dimensional topological insulator with a Curie temperature of ∼15 K. The quantised Hall resistance h/e^2 is directly given by a topological characteristic of the band structure, namely the first Chern number (a topological invariant of the material). Also, higher Chern number QAH insulators have been proposed with Cr-doped $Bi_2(Se,Te)_3$ being a candidate [147]. To observe the QAH effect it is first necessary to induce broken TRS, by e.g. induction of ferromagnetic order, within a bulk insulating sample [13, 37, 148].

It has been experimentally challenging to achieve long-range ferromagnetic ordering in the bulk of chalcogenide TIs. Earlier work focused on their use as dilute magnetic semiconductors [129]. In the previous chapter ferromagnetic order was demonstrated in Mn-doped TI bulk and thin film samples, albeit with some highlighted material challenges. Others have also demonstrated the successful ferromagnetic doping with Mn [85, 86], as well as Fe [149], in thin film and bulk samples. Cr doping has been predicted to lead to an insulating ferromagnetic ground state in

Bi_2Se_3 [39, 134], as required for the QAH effect, whereas Mn and Fe doping leads to a metallic state [133]. Most importantly, Cr^{3+} is expected to enter the crystal matrix by substituting for isoelectronic Bi^{3+}, thus not adding additional charge carriers to the system. Cr-doped Bi_2Se_3 and Bi_2Te_3 bulk crystals have been successfully grown, and for $x = 0.075$ [in $(Cr_xBi_{1-x})_2Se_3$] anti-ferromagnetic order has been observed with Cr being divalent and having a magnetic moment of 4.9 μ_B [150]. However, in thin films, and for Cr concentrations of $< 5\%$, magnetic long-range order has been reported up to 20 K [151]. For Cr-doped Sb_2Te_3 [152], long-range ordering of the magnetic ions was proposed to be through the local valence electrons (van Vleck mechanism) [39]. However, experimental data obtained for Cr-doped Bi_2Te_3 could not fully support this claim [153].

In this chapter, a structural and magnetic study of Cr-doped, n-type Bi_2Se_3 thin films grown by MBE is presented. These samples were grown in the high doping limit and were investigated by use of XRD, magnetometry and PNR. This section of the work has been published as Ref. [21]. Later in the chapter, XMCD and extended x-ray absorption fine structure (EXAFS) is used to further understand the electronic nature of the magnetic ground state and the manner in which the Cr dopant incorporates within the crystal matrix. XMCD and EXAFS work has been published as Ref. [20] and has been performed in collaboration with Dr. A. I. Figueroa and Prof. G. van der Laan.

6.2 Sample Preparation and Characterisation

6.2.1 Thin Film Growth

MBE was used to prepare $(Cr_xBi_{1-x})_2Se_3$ thin films on c-plane sapphire substrates, typically of 40-100 nm thickness. The MBE chamber has a base pressure of 1×10^{-10} Torr. The substrates were first cleaned using the procedure described in ap-

pendix B before baking overnight in vacuum. Thin films samples were grown by co-deposition, with Cr originating from a high temperature effusion cell provided by Createc GmbH. Samples were grown with a Se overpressure and a corresponding Bi:Se ratio of 1:10. Growth is limited by the Bi flux which was set to a beam equivalent pressure (BEP) of 6×10^{-8} Torr, leading to a growth rate ∼0.9 nm/min. Before growth the sapphire substrates were outgassed in the growth chamber at 450°C for 20 min.

The films were grown via a two-step process involving first the deposition of a 10-nm-thick low-temperature Bi_2Se_3 seed layer at $T_{sub} = 250$°C. Then, the temperature is raised to 300°C for the growth of the Cr-doped material. The sample was then slowly ramped down to room temperature under a residual background of Se, thereby reducing the risk of defect formation. This recipe is built on that used for the successful growth of undoped Bi_2Se_3 films (chapter 4) and the use of a seed layer here helps to establish the correct growth mode and crystal lattice before introducing the dopant.

Reflection high energy electron diffraction images taken during growth show a sharp streaky pattern indicative of 2D growth [Fig. 6.1(a)]. The 3-fold symmetry of the pattern is visible upon rotation. The ratio of spacings between the RHEED images taken with an azimuthal rotation of 30° with respect to each other is $\sqrt{3}$, indicative of the $R\bar{3}m$ space group of the material. AFM imaging shows the usually observed triangular growth domains and an overall flat surface (RMS roughness ∼2.98 nm) with the c-axis out-of-plane [Fig. 6.1(c)].

6.2.2 Structural Characterisation

XRD and rocking curves were obtained on the Bruker D8 x-ray diffractometer with a Cu anode ($\lambda = 1.54$ Å). Incident optics were set with a Ge (220) 2-bounce monochro-

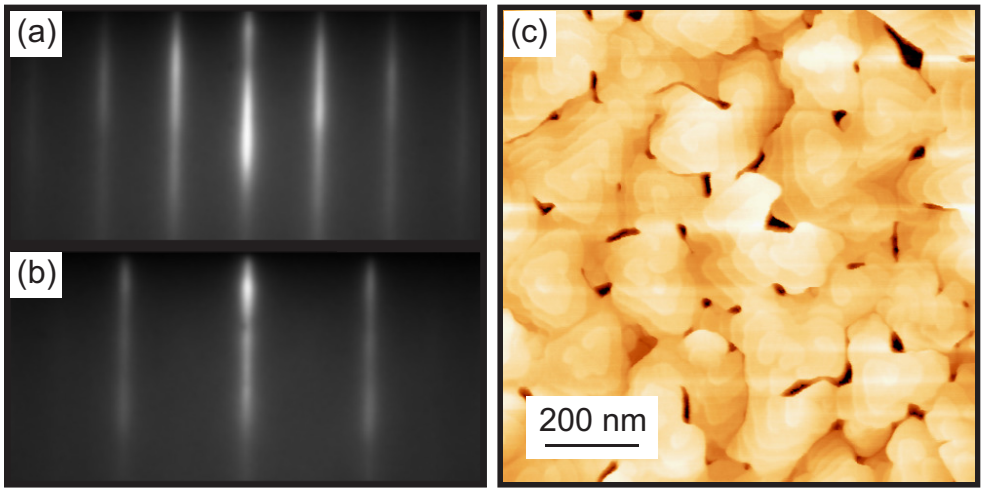

Figure 6.1: (a) RHEED image of a 42-nm-thick $(Cr_{0.12}Bi_{0.88})_2Se_3$ film recorded at the end of growth along the $[10\bar{1}0]$ azimuth of the *c*-plane sapphire substrate. A streaky pattern is visible indicative of 2D growth. (b) RHEED taken along the $[11\bar{2}0]$ azimuth. (c) AFM of grown film showing 3-fold symmetric triangular growth with quintuple layer steps expected from Bi_2Se_3.

mator, 2.5° Soller slits and 1 mm beam mask. The receiving optics used 2.5° Soller slits arriving at either an area detector (XRD) or a scintillator counter (rocking curves). It is found that even with the relatively high doping of $x = 0.12$ used here the crystalline quality remains good, in contrast to that reported in Ref. [151], in which a significant peak broadening at a similar doping level is found. XRD shows peaks of the $(00l)$ family for Bi_2Se_3 with a measured lattice parameter, c, of (28.66 ± 0.01) Å for undoped Bi_2Se_3 and (28.65 ± 0.01) Å for $(Cr_{0.12}Bi_{0.88})_2Se_3$, in close agreement with the expected value of 28.636 Å for Bi_2Se_3 (ICSD 617072) [154]. A variation in *c*-axis lattice constant was not observed for films with $x = 0.12$, which is in contrast to earlier reports of Cr-doped Bi_2Se_3 with similar Cr doping concentrations [151], but is consistent with fully substitutional doping. It is found that with higher percentage doping of Cr ($x > 0.12$) an additional parasitic phase forms, as observed by XRD (see Fig. 6.3). Due to the low intensity of the peaks and their increased width it is difficult to ascertain exactly the form of the parasitic phase, although it seems likely to fit some CrSe compound, summarised in Tab. 6.1. These possible compounds do not fully fit

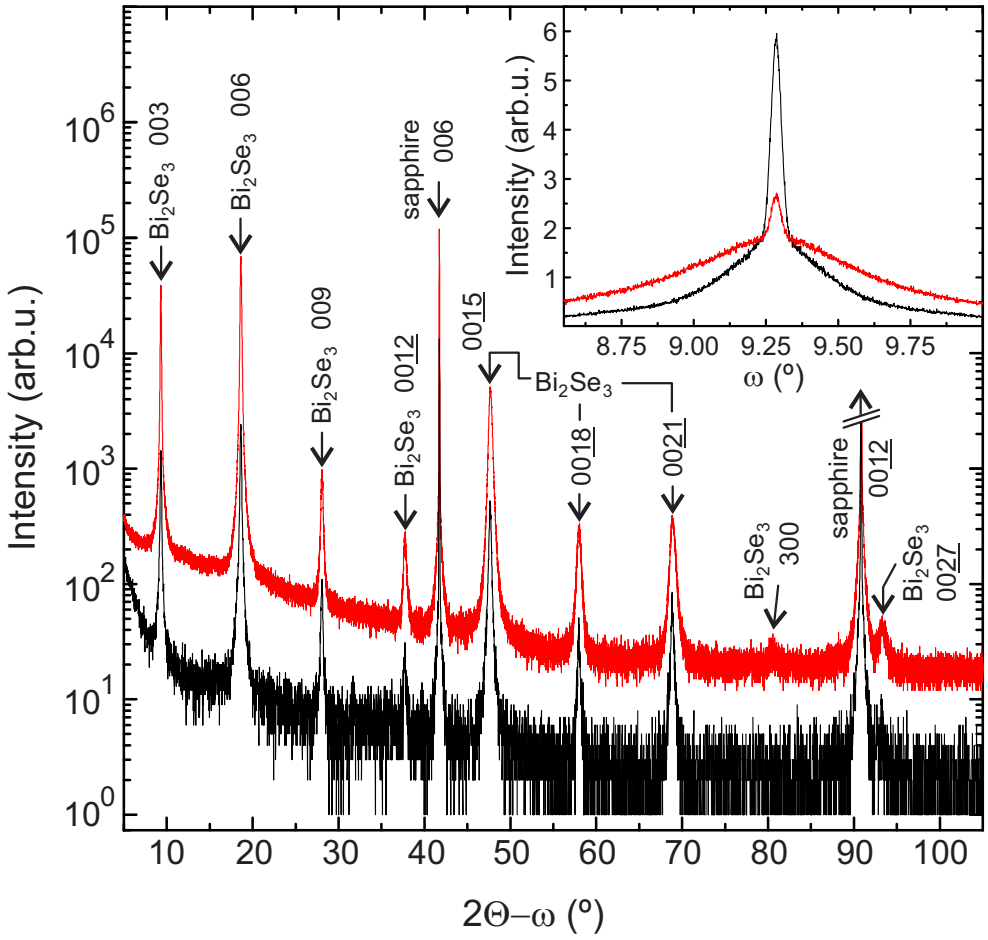

Figure 6.2: X-ray diffraction of a Cr-doped thin film with $x = 0.12$ [$(Cr_xBi_{1-x})_2Se_3$] (red) and a reference Bi_2Se_3 film (black). Inset: rocking curve of (006) peak of Bi_2Se_3.

the peaks observed, however it must be considered that any clusters or crystallites within the sample may well be strained and so have altered lattice parameters.

Rocking curves were measured of the (006) peak of Bi_2Se_3 (Fig. 6.2, inset). The reference Bi_2Se_3 film shows a FWHM of 0.0556°, increasing to 0.0675° for the Cr-doped film with $x = 0.12$. There are clearly two distinct Lorentizan functions in each rocking curve, for this estimation only the intense narrow peak is considered. The broader feature could result from a number of factors, e.g. strain, interfacial disorder or film roughness. It is anticipated that, similar to other dopants into this material

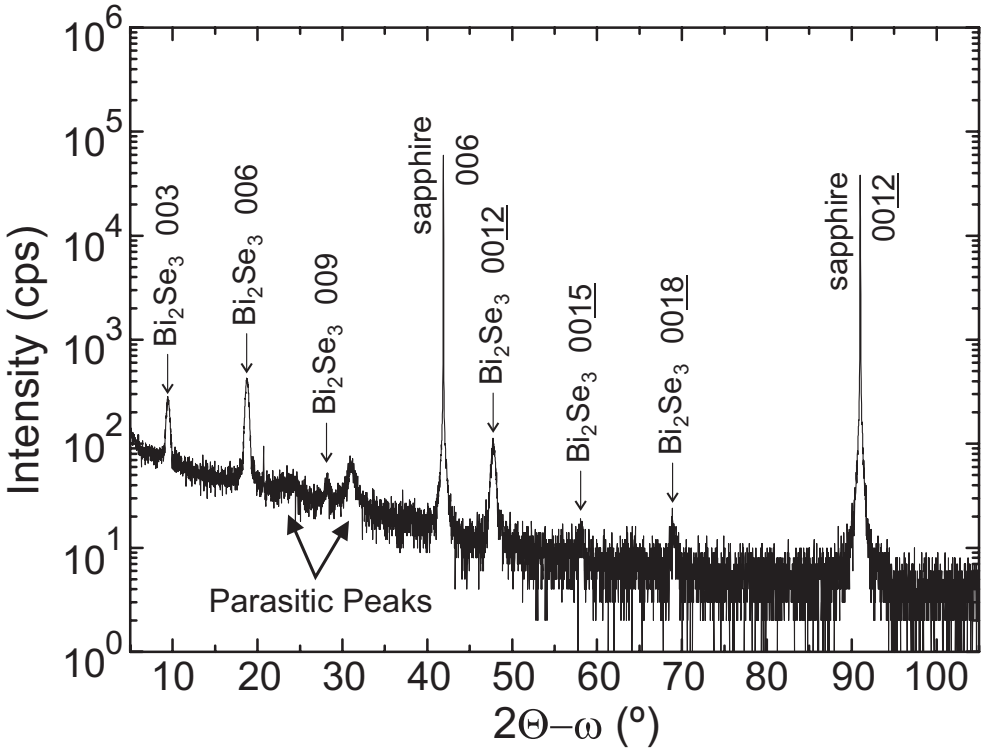

Figure 6.3: X-ray diffraction of a Cr-doped film with $x = 0.30$ $[(Cr_xBi_{1-x})_2Se_3]$. This higher doping shows broadening of the Bi_2Se_3 peaks as well as some unidentified parasitic phase.

system, Cr substitutes on the Bi site, although some may also occur intercalated into the van der Waals gap, increasing the disorder in the c-axis and causing the increase in the measured FWHM. This increase in FWHM is however significantly lower than that seen by others [151]. This, combined with the absence of change in the c lattice parameter, strongly indicates that Cr is incorporated substitutionally on the Bi site, since interstitial defects would generally alter the lattice parameter.

RBS measurements, from A. Pushp at IBM, were used for accurate determination

Table 6.1: Possible parasitic phases present in the sample. Data are received from ICSD.

Material	First Peak	Second Peak
CrSe	(001) - 15.396°	(002) - 31.026°
Cr_2Se_3	(001) - 15.365°	(002) - 30.990°

of film thickness and dopant concentrations. The thickness of the sample used for the neutron experiments is determined to be (103±5) nm. The total peak areas for Cr, Bi and Se are measured as 1.59×10^{16} at/cm^2, 1.47×10^{17} at/cm^2 and 2.46×10^{17} at/cm^2 respectively, from which the concentrations are calculated to (4.6 ± 0.5) at-% for Cr, (35.3 ± 0.5) at-% for Bi, and (60.1 ± 0.5) at-% for Se, resulting in a chemical composition of $(Cr_{0.12}Bi_{0.88})_2Se_3$.

6.2.3 Magnetometry

The magnetic properties of the Cr-doped films were investigated using SQUID magnetometry and polarised neutron reflectometry. Measurements of the magnetic hysteresis, $M(H)$, and the temperature dependence of the magnetisation, $M(T)$, were carried out in a Quantum Design MPMS XL and SQUID VSM, respectively. PNR measurements were performed on the POLREF beamline at the ISIS neutron and muon source of the Rutherford Appleton Laboratory.

Figure 6.4(a) shows the magnetic moment per Cr ion for a 103-nm-thick Cr doped film with $x = 0.12$ measured at T=2 K as a function of applied field perpendicular to the c-axis (i.e., in-plane). The linear diamagnetic contribution of the sapphire substrate has been removed by subtracting a linear fit to the high-field region. An open loop is seen with a coercive field of $H_c \approx 10$ mT, indicative of ferromagnetic ordering. The loop closes at ∼0.1 T, above which a continuous reorientation of the magnetic moments is observed. Saturation is reached at ∼1.0 T. The measured saturation magnetisation of (2.07±0.1) μ_B/Cr is smaller than the moment of 3 μ_B/Cr expected for a free Cr^{3+} ion (with quenched orbital moment). This observation is in close agreement with earlier work by Haazen *et al.* [151], who found a moment of ∼2 μ_B/Cr for concentrations of 5% [in $Cr_x(Bi_2Se_3)_{1-x}$].

Figure 6.4(b) shows the magnetisation measured as a function of temperature upon heating under an applied field of 10 mT from 5-50 K. The sample was cooled

in zero field. The diamagnetic background (taken to be T independent) has been subtracted from the data. T_C is extracted from the data using the first derivative of the smoothed $M(T)$ (see inset). The ferromagnetic to paramagnetic phase transition occurs over a broad temperature range. The Curie temperature is determined to be 8.5 K from the minimum point of the differentiated data (red dashed line).

6.3 Polarised Neutron Results

PNR was used to extract the structural and magnetic depth profile for the $x = 0.12$ sample. A field of 0.7 T was applied in the plane of the sample, parallel to the quantisation axis of the neutron spin. Reflectivity curves for the two neutron spin eigenstates were measured without polarisation analysis. Model fitting was carried out using an optical transfer matrix approach [155] and a differential evolution fitting algorithm using GenX [156]. Measurements were carried out at 5, 15 and 50 K.

The model shows a high-quality structural profile with densities within 6% of the nominal value for the doped layer and fixed to the nominal value for the buffer layer. The Cr concentration was fixed to the value determined by RBS measurements. Interface roughnesses were less than 6 Å for the sapphire and below measurable limit for the surface. The interface between the buffer layer and the doped layer is ill-defined in the fits and transitions gradually over 3.3 nm. The buffer layer thickness was allowed to vary but converged at 17.5 nm, close to the expected value. To allow for variations in the magnetisation depth profile the magnetic layer was split into several layers, two for the final model but more were tried without significantly improving the quality of fit.

The reflectivity data, spin asymmetry and corresponding model for the 5 K measurements are shown in Fig. 6.5(a-c). All fit attempts returned a uniform magnetisa-

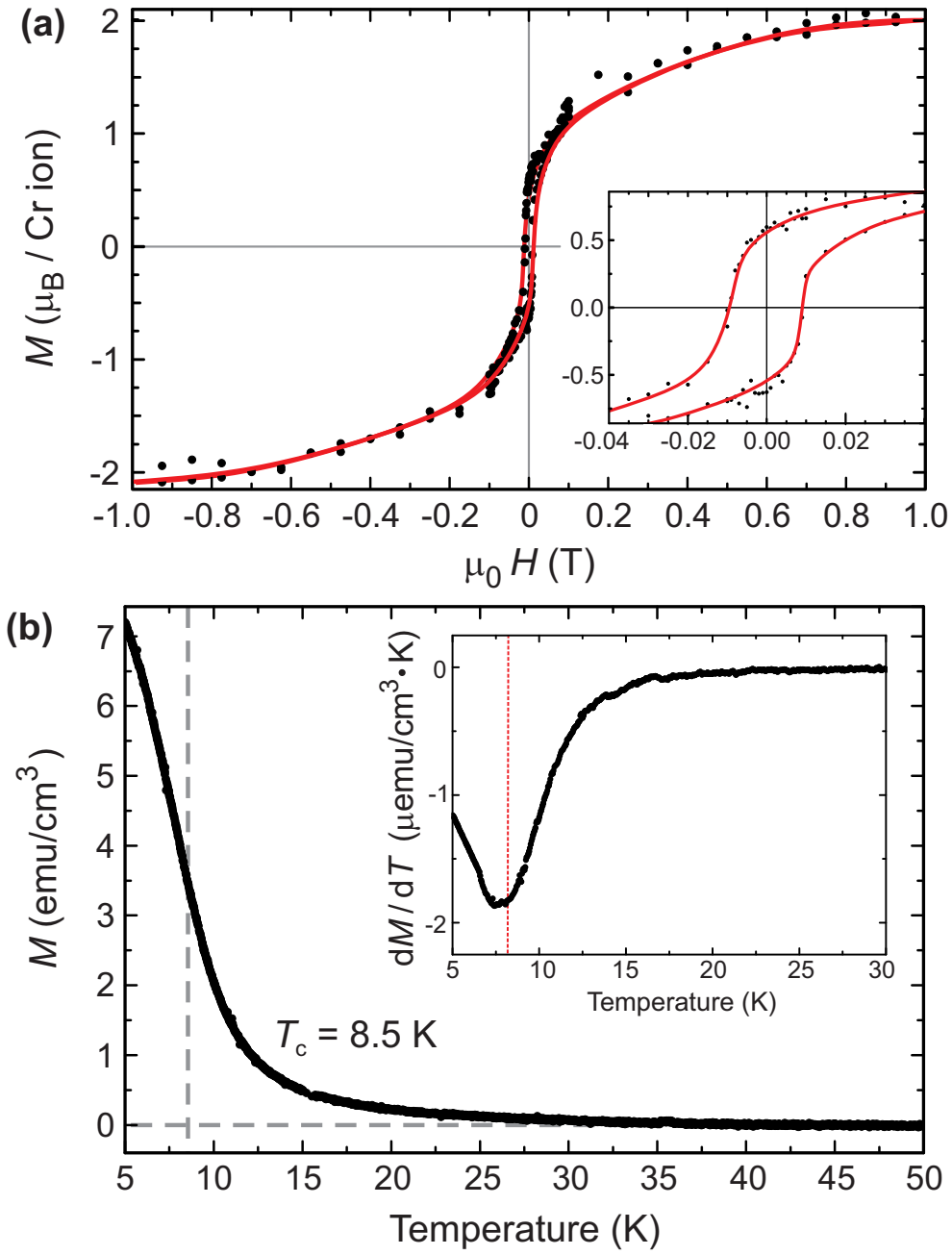

Figure 6.4: (a) Magnetisation curve, $M(H)$, of a $(Cr_{0.12}Bi_{0.88})_2Se_3$ thin film measured at 2 K with the field in-plane. Inset: detail showing an open loop with $H_c \approx 10$ mT. The red lines are a guide for the eye. (b) Temperature dependence of the magnetisation, $M(T)$, measured in an applied in-plane field of 10 mT. Inset: plot of the differentiated $M(T)$ curve, suggesting a T_C of 8.5 K.

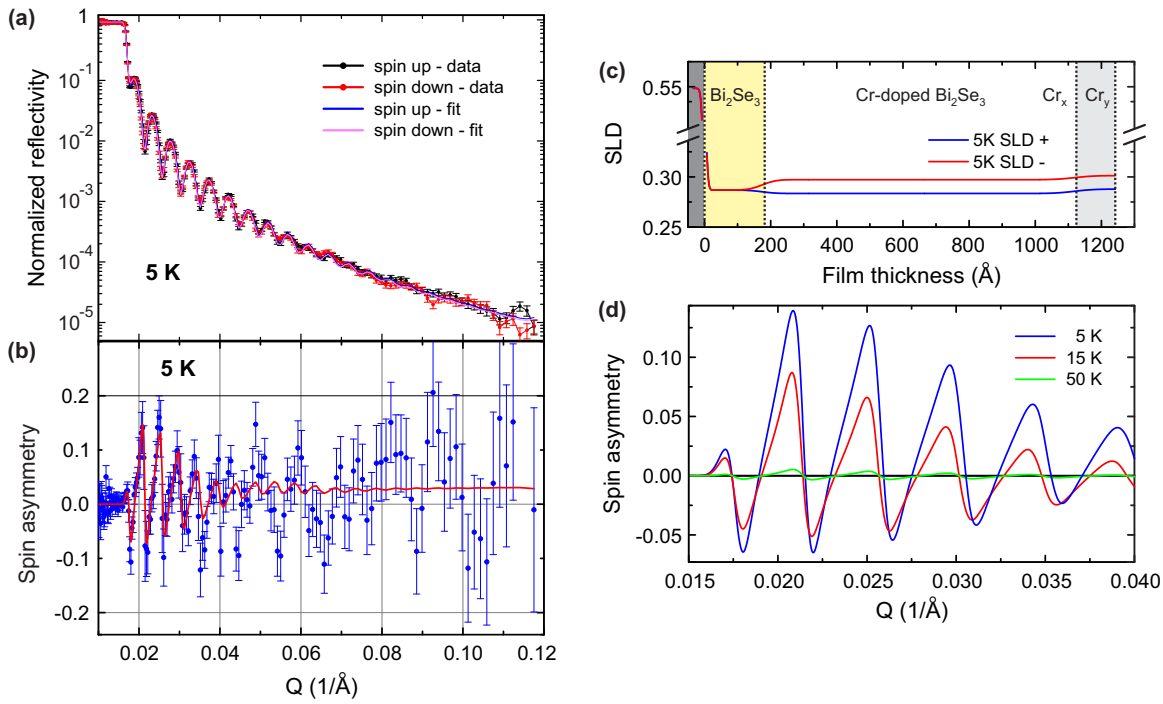

Figure 6.5: Polarised neutron reflectometry obtained in an applied field of $\mu_0 H = 0.7$ T at a temperature of 5 K, showing the normalised reflectometry (a) and spin asymmetry (b) as a function of momentum transfer. The solid line is the best-fit calculation for the model described in the text. (c) Model of the scattering length density (SLD) at 5 K for the layered thin film system, consisting of substrate (dark gray), Bi_2Se_3 buffer layer, and two Cr-doped top layers which have Cr concentrations of x and y, respectively. (d) Plots of the fitted spin asymmetries at 5 K, 15 K and 50 K.

tion profile with a gradual transition between the buffer layer and the doped layer and a homogeneous magnetisation up to the surface. The moment at 5 K was estimated at 1.5 μ_B/Cr, which agrees well with the SQUID results at the same field (0.7 T) and temperature.

No enhancement of the magnetisation in the surface region was found, as had been suggested to occur in these materials [157]. Simulations assuming a thin surface layer with an enhanced magnetisation showed that it manifests itself as a constant splitting of the two reflectivity curves at higher wave vector transfer (Q). The magnitude of the splitting is determined by the magnitude of the magnetisation in the surface layer and the onset of splitting in Q is determined by the thickness of the layer. This data

shows no such splitting even at the highest Q values measured here. From this it may be concluded that there is no surface-enhanced layer within the detection limit of around 5 Å and a magnetisation enhancement from 2 μ_B/Cr to 3 μ_B/Cr, assuming a constant Cr concentration of $x = 0.12$. Transport measurements [151] were able to rule out the possibility of magnetic clusters, but could not inform the discussion on any surface enhancement. These results unambiguously show that a near-surface modification to the magnetic polarisation is not present.

For higher temperature data only the magnetisation was allowed to vary with the structural parameters remaining fixed. At 15 K there is some remaining magnetisation and the model indicates a higher magnetisation in the bulk of the film (about 1 μ_B/Cr) and a region near the surface where the magnetisation is significantly diminished. The best fit values are 13.5 nm for the top layer and 0.2 μ_B/Cr in that region, but the exact extent of this region has a significant error as there is some correlation between the top layer thickness and the size of the magnetic moment. However, the finding of a reduced top layer region appears robust. 15 K is above, but not far away from, the Curie temperature of the sample. The remaining magnetisation at 15 K is most likely induced by the large applied field during the PNR measurement and the proximity to T_C. At 50 K the magnetic order has almost completely vanished. Figure 6.5(d) shows the model spin asymmetries for all three temperatures.

The magnetic moment of Cr in saturation obtained from magnetometry of 2.1 μ_B/Cr (at 2 K, SQUID) is less than the calculated moment of $\sim$3.78 μ_B for Cr substitutional on Bi sites [158], but in good agreement with the moment obtained using polarised neutron reflectometry. For interstitial Cr the moment is $\sim$0.71 μ_B, where both values have been calculated in a surface environment [158]. It is possible that this 'missing moment' could also be due to the presence of Cr that does not contribute to the long-range ferromagnetically ordered phase, but instead an antiferromagnetic or paramagnetic phase with the same crystal structure. Another explanation could be

for Cr being in a different valence state than anticipated for Cr doping onto the Bi site. These open questions regarding the valency of the Cr dopant and the reduced magnetic moment will be the subject of further work using XMCD and EXAFS.

6.4 Synchrotron Studies: Evidence for Divalent Cr

The choice of Cr as a dopant for chalcogenide TIs over the other possible transition metals, for example, Mn and Fe, is determined by its electronic structure. Whereas Mn and Fe lead to a quasi-metallic state [133], Cr should yield a gapped ferromagnetic ground state in Bi_2Se_3. The established opinion in the literature has been that the Cr dopant has a 3+ oxidation state because it substitutionally replaces the Bi^{3+} in Bi_2Se_3, similarly to related compounds [12, 39, 133, 134, 151, 152, 159]. It has been asserted earlier in this chapter that we anticipate a substitutional doping mode of $(Cr_xBi_{1-x})_2Se_3$. Other possible doping modes exist, for instance, with Cr incorporating into the van der Waals gap ($Cr_yBi_2Se_3$), which would give a lower oxidation state and therefore an increased n-type carrier concentration. This manner of doping should be detectable by XRD as an increase in the c-axis lattice constant, which is not found here (c.f. Fig. 6.2). In this section, the element-specific techniques of extended x-ray absorption fine structure (EXAFS), x-ray absorption spectroscopy, and x-ray magnetic circular dichroism will be used to determine the local electronic and magnetic state of the Cr dopants in Bi_2Se_3. Contrary to the prevalent belief it is found that the substitutional Cr is mainly divalent, which is due to the covalent character of the Cr-Se bonds.

The expected oxidation state for transition metal dopants into the chalcogenide TIs has been previously calculated [160], using the local spin-density approximation (LSDA). This work found that, for the first row of transition metals up to Fe, an

oxidation state of 3+ is to be expected. Moving to higher atomic numbers this oxidation state reduces to around 2+ for Co and 1+ for Ni. The authors explained this reduction to be due to hybridisation between the transition metal $3d$ and the Se/Te p orbitals. These results were then later confirmed from first principles calculations by Zhang *et al.*, who found that Cr^{3+} is the most energetically favourable configuration doping substitutionally and isoelectronically onto the Bi^{3+} lattice site [133]. This work would indicate that, for co-doped Cr-Bi_2Se_3 films grown by MBE, one may expect the Cr to dope (as Cr^{3+}) fully substitutionally on the lattice site, as $(Cr_xBi_{1-x})_2Se_3$, up to a certain solubility limit. Previous transport work has indicated that this is the case for Cr-doped Bi_2Se_3 thin films [161]. Cr has also been observed to dope as 3+, replacing Sb in Sb_2Te_3 thin films [118]. For Cr^{3+} there should be essentially no change to the bulk carrier concentration, whereas for Cr^{2+} one would observe n-type carrier doping from the transport properties. This argument assumes only a purely ionic nature of the (Bi,Cr)-Se bond which may, however, also have some covalent character. It should also be anticipated that Cr-Se bond length may be reduced in the case of substituted Cr (compared with the Bi-Se bond length) given the smaller ionic radius of Cr^{3+} (75.5 pm) compared with Bi^{3+} (117 pm) [162].

The results of the SQUID and PNR work presented earlier indicate a magnetic moment at saturation of $\sim 2\mu_B$/Cr, far less than the expected value (from Hund's rules) of $\sim 3\mu_B$/Cr for Cr^{3+} on the Bi site. This magnetisation value could be explained by Cr^{4+} in the low spin state. However, such a configuration would require a crystal field greater than 2.5 eV, which seems unlikely in this case [118]. Additionally, such an oxidation state is not supported by earlier transport studies [161], where no carrier dependence of the doping concentration is found.

6.4.1 XAS and XMCD Studies

As has been seen earlier in this thesis, XAS and XMCD provide a local probe of the electronic nature of the magnetic ground state in an elementally selective way. They are, therefore, an ideal tool to further study the magnetic order of the Cr-doped Bi_2Se_3 presented here as they provide a probe of magnetism that is sensitive to both the lattice site and valence of the element probed. The XAS at the Cr $L_{2,3}$ edges was simultaneously measured in total-electron yield and fluorescence yield detection on beamline I10 at Diamond Light Source, at a temperature of 5 K within a 14 T superconducting magnet. The XMCD is obtained as the difference between the two XAS spectra recorded with the x-ray helicity vector and applied magnetic field anti-parallel and parallel ($\mu^- - \mu^+$). The measurements were performed by reversing the polarisation of the incident x-rays, to avoid switching the high field of the superconducting magnet. The samples were measured both at normal and grazing incidence, with the magnetic field always along the x-ray beam. The degree of circular polarisation in the energy region of interest is close to 100%. The area probed by the beam (20×200 μm^2) is much smaller than the sample size (10×10 mm^2).

As has been mentioned earlier, XAS is a highly surface sensitive technique and therefore can be used to gain information regarding any surface modification (e.g., oxidation) in these samples. While TEY measurement in normal incidence probes only the top 35 nm of the sample, FY (grazing incidence in this case) probes the entire depth of the film, including part of the sapphire substrate. However, different selection rules, self-absorption and saturation effects mean that the FY is not linearly proportional to the x-ray absorption. For instance the L_2/L_3 peak intensity ratio is strongly enhanced in FY compared with TEY [57]. Therefore, FY should only be used in a qualitative manner, and applying the sum rules in this case can give a large error. TEY, on the other hand, is directly proportional to the x-ray absorption, with

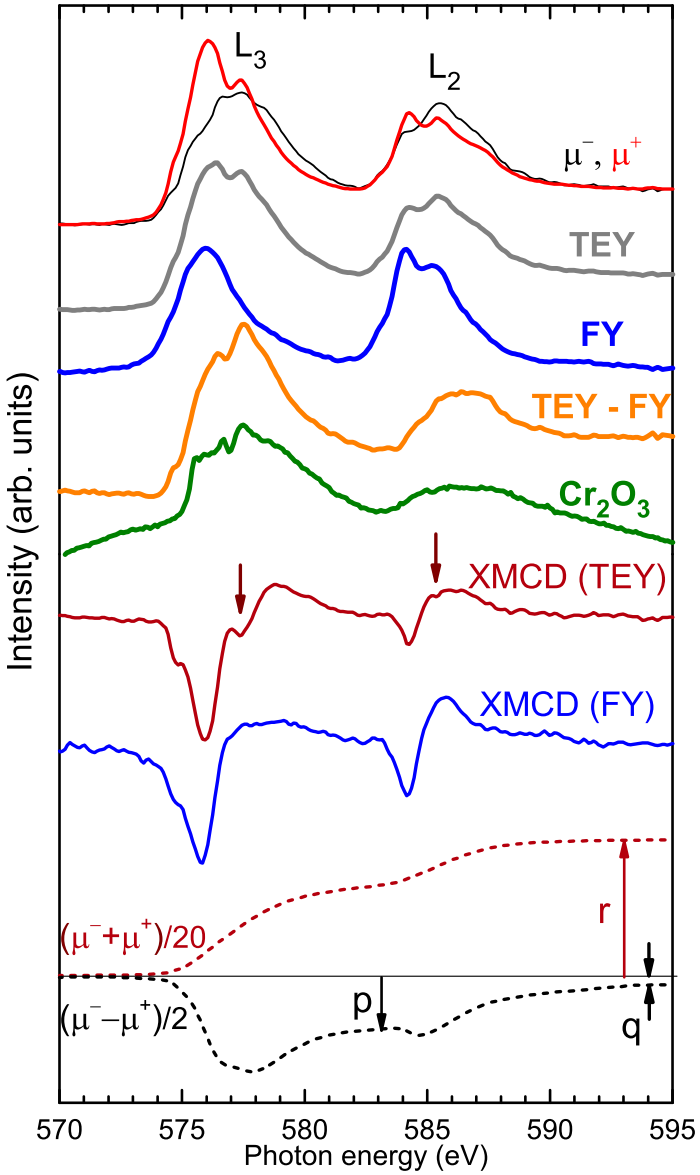

Figure 6.6: Experimental Cr $L_{2,3}$ XAS and XMCD spectra of Cr-doped Bi_2Se_3 and a Cr_2O_3 reference in 7 T field at 5 K. From top to bottom: TEY spectra for opposite circular polarisations (μ^-, μ^+) in normal incidence, XAS averaged over the two polarisations for TEY in normal incidence and for FY in grazing incidence. Difference between the TEY and FY spectra for the Cr-doped Bi_2Se_3 is compared with the Cr_2O_3 reference measured in FY. XMCD spectra measured in TEY and FY. The arrows indicate additional shoulders at each edge in the XMCD (TEY) due to Cr^{3+}. Spectra are vertically offset for clarity. At the bottom, the dashed curves show the integrated intensities of the summed XAS ($\mu^- + \mu^+$) and the XMCD ($\mu^- - \mu^+$) measured in TEY. Values of p, q, and r appearing in the sum rules are indicated. Figure appears in Ref. [20].

negligible saturation effects for the dilute samples presented here.

Figure 6.6 shows the Cr $L_{2,3}$ XAS spectra of Cr-doped Bi_2Se_3 measured in TEY and FY. TEY measurements were obtained in normal incidence and the FY in grazing incidence to reduce saturation effects. The L_3 edge in the TEY spectrum reveals two distinct peaks with a separation of 1.35 eV. This higher energy peak is absent in the FY spectrum, indicating that this peak arises only from the top few nm of the sample. Subtracting the FY spectrum from the TEY spectrum gives some indication of the nature of the surface contribution to the measured XMCD spectrum. For comparison, a Cr_2O_3 reference standard is also measured in FY, as shown in Fig. 6.6. The agreement between the (TEY-FY) difference spectrum and the measured Cr_2O_3 (where Cr is 3+) standard in both spectral shape and energy position of the observed peak confirm that the top layers contain mainly Cr^{3+}. This is further confirmed by comparing the XMCD measured in TEY and FY at 5 K and with a 7 T applied magnetic field. The XMCD for the TEY measurement shows additional shoulders at the energy position of the Cr^{3+} $L_{2,3}$ peaks (indicated by arrows in Fig. 6.6). These shoulders are not similarly observed in the FY XMCD spectrum. It is generally seen in XAS and XMCD measurements that a more electro-positive ion will give a peak at a higher photon energy [163]. This, therefore, implies that the bulk peak (at 576 eV), which is at lower energy than the Cr^{3+} peak, must have more Cr^{2+} character.

The XAS branching ratio B is defined as the fraction of the total XAS intensity at the L_3 edge, i.e., $B = I(L_3)/[I(L_3) + I(L_2)]$, where I represents the peak intensity at the relevant edge. It has been shown that for high-spin states in octahedral crystal-field symmetry the value of B increases with the number of $3d$ electrons [164]. Atomic multiplet calculations, performed by Prof. G. van der Laan, given an octahedral crystal-field symmetry give $B = 0.593$ for Cr^{3+} $3d^3$ and $B = 0.672$ for Cr^{2+} $3d^4$. The measured Cr $L_{2,3}$ XAS in TEY of the Cr-doped Bi_2Se_3 film has a branching ratio of 0.657, which indicates the presence of a large amount of Cr^{2+}. However, the branching

ratio is also sensitive to the hybridisation between orbitals, as suggested earlier to be a possibility, so a quantitative analysis by sum rules would not be reasonable here.

Applying the XMCD sum rules [58] with an appropriate correction factor of $C = 2.0 \pm 0.2$ to the integrated intensities of the TEY spectra in Fig. 6.7 gives the average orbital and spin moments per Cr as $\mu_L = (0.04 \pm 0.1)\ \mu_B/\mathrm{Cr_{av}}$ and $\mu_S = (2.90 \pm 0.3)\ \mu_B/\mathrm{Cr_{av}}$. According to Hund's third rule, for less than a half-filled shell, μ_L should be negative, which is possible within the error bar of these results. Since the orbital contribution is only a few percent, it does not significantly contribute to the total magnetic moment. As was highlighted in chapter 5 it is also possible to extract quantitative information from XMCD spectra by direct comparison with spectra calculated from atomic multiplet theory. Qualitatively speaking, the measured spectra in Fig. 6.7 do not show the distinct multiplet structure as may be expected for ionic Cr^{3+} [165, 166], which suggests the d states are more hybridised than atomic-like. Within the atomic multiplet calculations different, mixed, ground states are used to describe the Cr bulk and surface contributions, denoted as $\mathrm{Cr_{bulk}}$ and $\mathrm{Cr_{surf}}$, which are predominantly divalent and trivalent in character, respectively (see Fig. 6.7). The ground state for $\mathrm{Cr_{bulk}}$ is calculated as 70% d^4 and 30% d^3 in an octahedral crystal-field, which gives a total d electron count of 3.7 and $m_S = 2.89\ \mu_B/\mathrm{Cr_{bulk}}$ ion. The ground state for $\mathrm{Cr_{surf}}$ is calculated as 79% d^3 and 21% d^2, which gives a total d electron count of 2.78 and $m_S = 2.83\ \mu_B/\mathrm{Cr_{bulk}}$ ion. As shown in Fig. 6.7, the experimental XAS spectrum can be fitted by weighting these different contributions as 0.54 $\mathrm{Cr_{bulk}}$ + 0.46 $\mathrm{Cr_{surf}}$. After being normalised to the peak XAS intensity, the measured XMCD spectrum is best fitted with 0.68 $\mathrm{Cr_{bulk}}$ + 0.32 $\mathrm{Cr_{surf}}$, which corresponds to relevant spin moments of 3.64 $\mu_B/\mathrm{Cr_{bulk}}$ and 1.91 $\mu_B/\mathrm{Cr_{surf}}$. As a check, this amounts to the average values for the whole sample of a d electron count of 3.27 and $m_S = 2.84\ \mu_B/\mathrm{Cr_{ave}}$, in good agreement with the sum rule result of $\mu_S = (2.90 \pm 0.3)\ \mu_B/\mathrm{Cr_{av}}$. Therefore, the multiplet analysis shows that the magnetic

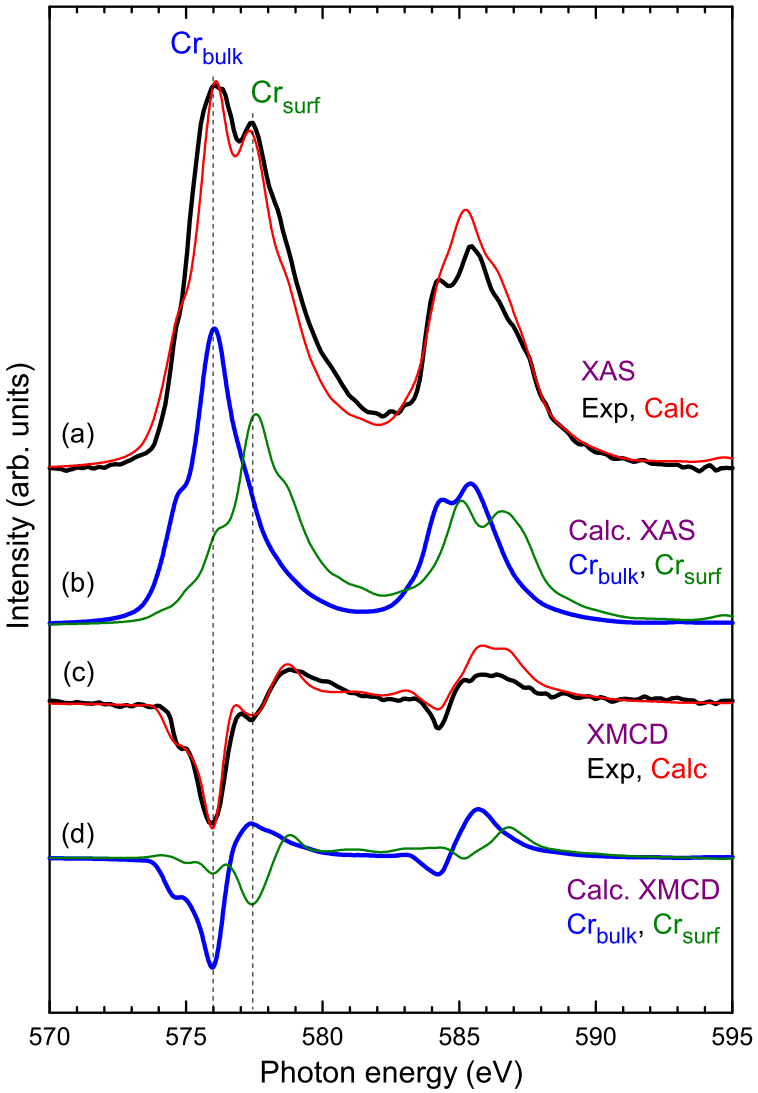

Figure 6.7: Cr $L_{2,3}$ spectra of Cr-doped Bi_2Se_3 in a 7 T applied magnetic field at 5 K in TEY. (a) Comparison between calculated (Calc) and experimental (Exp) XAS spectrum ($\mu^- + \mu^+$). The latter is corrected for background steps at the L_3 and L_2 edges. (b) Separate contributions of Cr_{bulk} and Cr_{surf} to the calculated XAS. (c) Comparison between calculated and experimental XMCD spectrum ($\mu^- - \mu^+$). (d) Separate Cr_{bulk} and Cr_{surf} contributions to the calculated XMCD. Figure appears in Ref. [20].

moment of Cr_{bulk} is almost fully saturated, and also that Cr_{surf} has a substantial magnetic moment. It has been previously observed that the valence states in magnetically doped TIs can have substantially different properties towards the surface region [126]. However, since these samples have been transferred from the MBE growth through to the XMCD experiment in air, it is also possible that this surface modification is the result of oxidation.

XMCD hysteresis curves are acquired by sweeping the applied field at the fixed photon energy of the Cr L_3 peak ($h\nu = 575.5$ eV), which reveals the field-dependent magnetisation of the Cr moments. Figure 6.8(a) shows the surface-sensitive TEY and (b) the bulk-sensitive FY for positive helicity with normal incidence at 5 K. The TEY hysteresis loop shows that the surface Cr moments saturate at the maximum applied field of 7 T. The FY hysteresis loop shows the bulk Cr moments are saturating at ∼3 T. Both hysteresis loops show a ferromagnetic behaviour, although no clear loop opening can be identified. This absence of a loop opening was also observed for Mn in chapter 5 and is due to the coercive field of the sample being lower than the remnant field (∼50 Oe) of the superconducting magnet at I10.

6.4.2 XANES and EXAFS Studies

X-ray absorption near edge structure (XANES) and EXAFS at the Cr K edge ($h\nu = 5989$ eV) were measured at room temperature on beamline B18 at Diamond Light Source to further characterise the electronic and structural environment of the Cr dopant. A nine-element solid-state Ge detector with digital signal processing for fluorescence XAS, high energy resolution and high count rate was used to measure with the beam at 45° incidence with respect to the sample surface. All spectra were acquired in quick-EXAFS mode using the Pt-coated branch of collimating and focusing mirrors, a Si(111) double-crystal monochromator and a pair of harmonic rejection

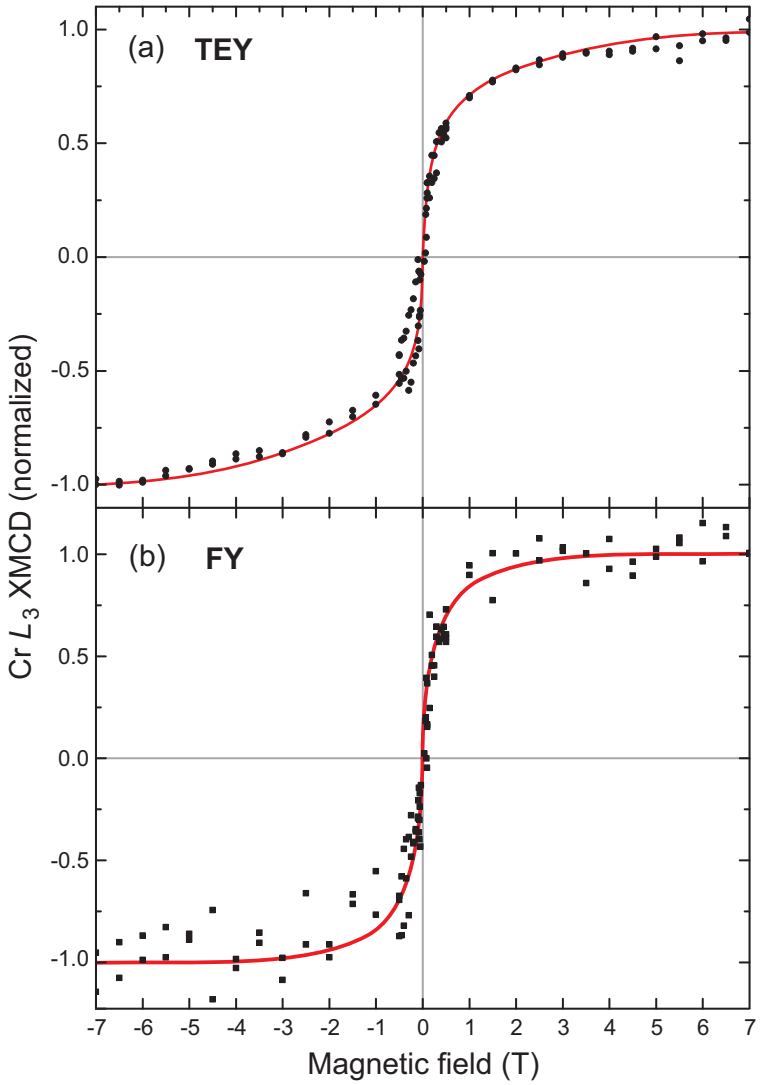

Figure 6.8: XMCD hysteresis at the Cr L_3 edge, measured at 5 K with the field applied normal to the sample surface up to ± 7 T. Measured in (a) TEY and (b) FY. The red lines are guides for the eye. Figure appears in Ref. [20].

mirrors. The energy range for each scan allowed the extraction of information in the extended region up to $k = (12 - 14)$ Å^{-1}. Polycrystalline samples of CrSe, Cr_2O_3, and CrO_3 in powder form, as well as a Cr foil of 5 μm thickness, were measured as references in transmission detection mode. EXAFS spectra were acquired, processed and analysed, by Dr. A. I. Figueroa, using different tools of the IFFEFIT XAS package [167]. EXAFS data analysis and fitting on all references and samples were performed in ARTEMIS [167], making use of models based on crystallographic information found in the ICSD. The atomic clusters used to generate the scattering paths for fitting were generated with ATOMS [168].

The normalised XANES at the Cr K edge of the Cr-doped Bi_2Se_3 thin film together with CrSe, Cr_2O_3, CrO_3 and Cr foil are shown in Fig. 6.9(a). By inspection it can be seen that the jump in absorption intensity seen in the thin film sample, most closely matches the energy position and qualitative lineshape of the CrSe standard. This standard is for Cr with a 2+ oxidation state, supporting the conclusion from XMCD that the Cr dopant is predominantly divalent. Additionally the spectrum of the Cr-doped Bi_2Se_3 film does not show a pre-edge peak similar to that observed in the CrO_3 spectrum. This pre-edge peak is characteristic of a tetrahedral local environment, so it may be concluded that the Cr dopant here is certainly not tetrahedrally coordinated, implying that the dopant is not at an interstitial lattice site.

The Fourier transform of the measured EXAFS signal for the Cr-doped Bi_2Se_3 film is shown in Fig. 6.9(b). This transform is performed over a k range from 3.3 to 12 Å^{-1} using a k^2 weight, a $\Delta k = 1.5$ Å^{-1}, and a Kaiser-Bessel window function. Different models were trialled to fit the measured EXAFS signal at the Cr K edge of the doped film. Fits were performed for R in a range from 1.2 to 3 Å, covering Cr in the first coordination shell [see Fig. 6.9(b) and its backwards Fourier transform in Fig. 6.9(c)]. The parameters fitted were the interatomic distance (R), the Debye-Waller factor (σ^2) for each scattering path and a general shift in the threshold energy (ΔE_0). The

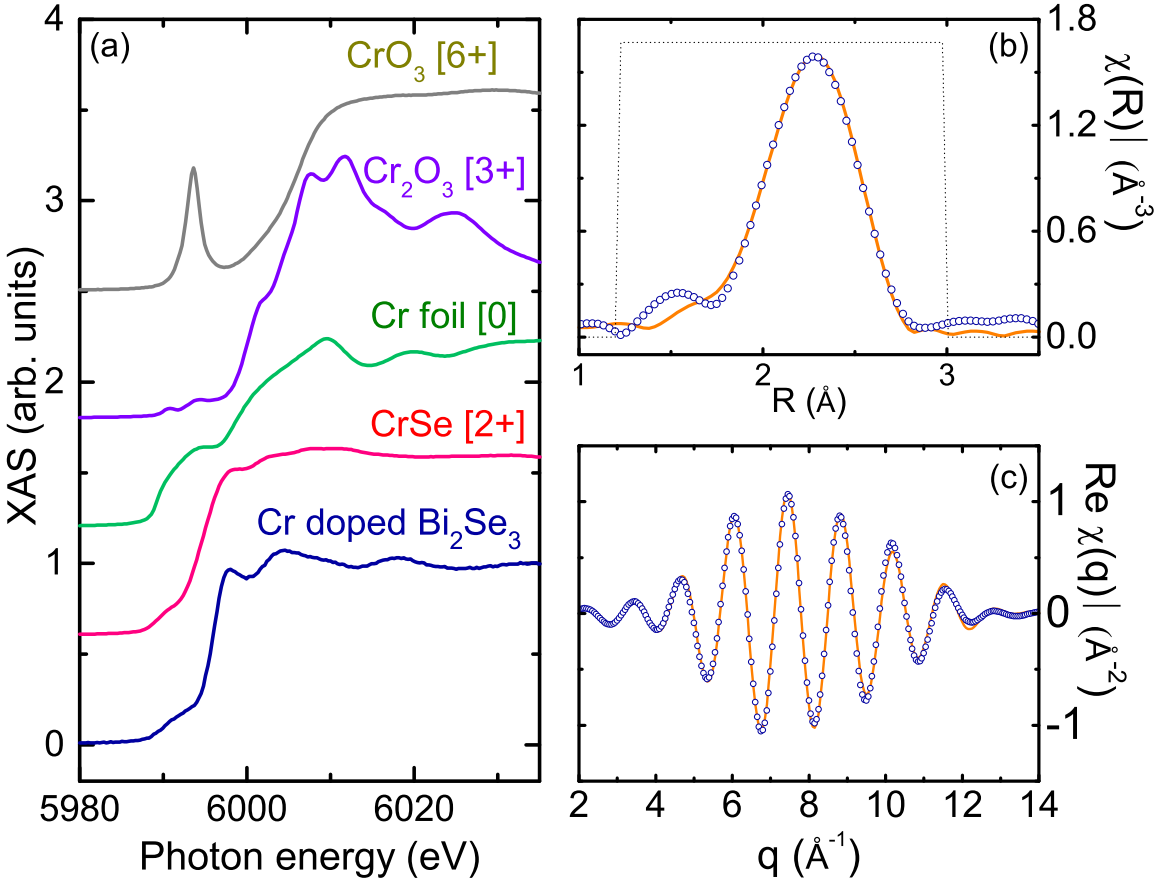

Figure 6.9: (a) Cr K edge XANES for a Cr-doped Bi_2Se_3 thin film and comparison with CrSe, Cr_2O_3, CrO_3, and Cr foil for reference. The Cr oxidation state is indicated in the square brackets. Spectra have been shifted vertically for clarity. (b) Fourier transform of the EXAFS signal at the Cr K edge on the thin film (symbols) together with the best fit to the first coordination shell (solid line). The dotted box gives the Kaiser-Bessel window function. (c) Contribution of the first coordination shell to the EXAFS signal (symbols) together with its best fit (solid line). Data from A. I. Figueroa, figure appears in Ref. [20].

best fits were achieved with Cr in an octahedral environment of Se atoms. The fit with a single CrSe scattering path of Cr in an octahedral symmetry was slightly worse than that performed with two different Cr-Se bonds. Thus the latter was considered the best fit, and the values of the structural parameters obtained from it are listed in Table 6.2. It should be noted that this was one of many attempted fits to the measured data. Other trialled fits continue to indicate no contribution from Cr-Cr scattering paths, confirming the absence of Cr clusters. A representation of the bonding scenario is shown in Fig. 6.10. The XANES and EXAFS results also do not observe any distinct Cr-O scattering path despite evidence for this existing at the surface has been shown by XMCD. This is due to the more penetrating hard x-rays (which are more penetrating) used for XANES compared with soft x-rays for XMCD.

	CrSe*1*	CrSe*2*
N	3	3
R (Å)	2.53 ± 0.01	2.64 ± 0.01
σ^2 (Å^2)	0.003 ± 0.001	0.003 ± 0.001

Table 6.2: Structural parameters obtained from Cr K edge EXAFS fits for the Cr-doped Bi_2Se_3 thin film shown in Fig. 6.9(b). Coordination number, N, interatomic distance, R, and Debye-Waller factor, σ^2, for each path. A value of $E_0 = (1.5 \pm 0.3)$ eV was obtained from the fit.

The EXAFS results obtained indicate that the Cr occupies octahedral sites within the host crystal, as has been previously observed for the dilute magnetic semiconductor, Cr-doped Ga_2Se_3. These results indicate that the Cr atoms in the doped Bi_2Se_3 system are substitutional on the Bi sites, in which case the Se atoms need to contract locally towards the Cr compared to the original Bi-Se bond distance ($\Delta d \approx -0.36$ Å). Previously published GGA calculations [133] predicted that the neighbouring Se atoms around the Cr dopant would contract by $\Delta d = 0.305$ Å and 0.362 Å for Se*1* and Se*2*, respectively. Such a contraction will strengthen the observed hybridisation between the Cr and Se atoms, hence broadening the impurity

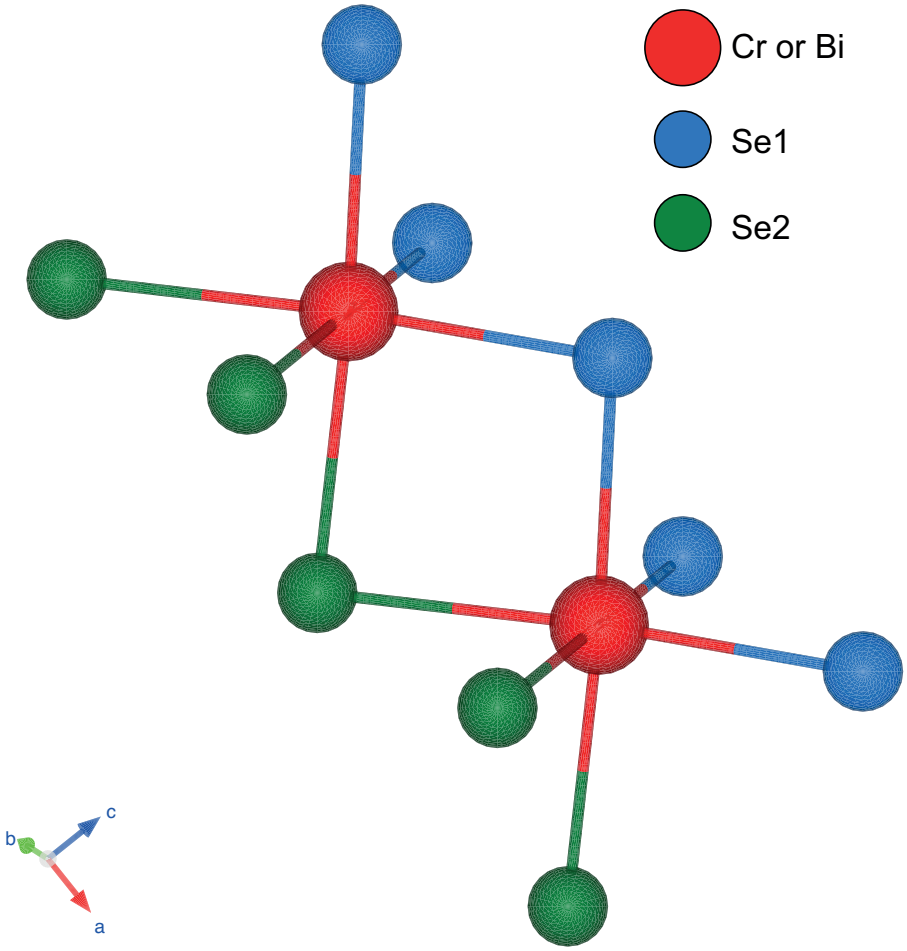

Figure 6.10: Diagram of the relevant bonding scenarious between Bi and/or Cr and the two lattice sites of Se, labelled Se1 and Se2.

bands [169]. These GGA calculations also demonstrated that, without relaxation, Cr-doped Bi_2Se_3 should have a band gap of 0.28 eV. After the predicted structural relaxation has been taken into account this band gap would reduce to 0.01 eV. This simulation work, in combination with our experiments, indicates that doping with Cr may open a band gap in the TSS and that this band gap is significantly influenced by the physical structure of the doped crystal.

6.5 Summary and Conclusions

In summary, it is found that Cr-doping into Bi_2Se_3 thin films is possible up to a Cr concentration of $x = 0.12$ without loss of crystalline quality and formation of secondary phases. At higher doping levels than this a parasitic phase forms, as observed by XRD, that is likely a CrSe compound. The lattice parameters of the $x = 0.12$ films are consistent with substitutional doping of the Cr. A saturation moment of $\sim$2.1 μ_B/Cr was found, which is lower than the expected full, orbitally quenched moment for Cr^{3+}. The magnetisation loop is dominated by a ferromagnetic open loop with a small coercive field of $\sim$10 mT and a T_C of 8.5 K. PNR showed that the ferromagnetism is prevalent throughout the film with no evidence of an enhanced surface magnetic layer. XAS, XMCD and EXAFS studies both indicate that the Cr dopes onto the Bi site as Cr^{2+}, rather than the expected Cr^{3+}. The reduced valency of the dopant is due to hybridisation between the Cr d and the Se p orbitals. This hybridisation is further enhanced through a contraction of the Bi-Se bond length when Bi is replaced with Cr, due to the smaller ionic radius of Cr compared with that of Bi. This covalent character to the bonding in the material allows for the Cr to dope with a 2+ oxidation state, without adding additional charge carriers to the net system. As such, these results to not directly contradict the highlighted earlier transport work that concluded no carrier doping occurred with Cr doping. XMCD is

used to isolate the bulk and surface magnetic properties of the film. Within the bulk, an almost full saturation moment of 3.64 μ_B/Cr is reached. This value is reduced at the surface due to possible oxidation of the top few nm of the sample. These results will encourage a re-evaluation of the assumptions made for the oxidation state of transition metal dopants in topological insulators. The ferromagnetic ground state in these materials indicates that Cr-doped Bi_2Se_3 could also be a candidate material for the observation and manipulation of a QAH state.

Chapter 7

Summary and Outlook

This thesis has been concerned with the fabrication of high quality topological insulator thin films, grown by MBE and doped with transition metal elements. The core aim was to demonstrate the ability to induce a ferromagnetic ground state in a doped topological insulator to break the intrinsic time reversal symmetry of the material. Such a broken symmetry state could then set the stage for the observation of a variety of novel physical effects, e.g., the quantum anomalous Hall effect (QAHE), topological magneto-electric effect, or image magnetic monopoles. Exploitation of such effects, in particular the QAHE, presents a novel way of hosting a spin-encoded state, with particular relevance to applications within quantum computation.

In chapter 4 the successful growth of all chalcogenide TIs was demonstrated on *c*-plane sapphire substrates. The films grown here represent a significant advancement on samples grown by solid state methods (c.f., chapter 5), due to the significantly lower defect densities in films grown by MBE. It is also worth noting that MBE-grown films are particularly applicable towards conventional device applications, for which thin films are needed. Later in the same chapter the growth of Bi_2Se_3 and Bi_2Te_3 on the amorphous substrate material fused silica was presented. It was shown that these prototypical TIs can be grown with a high degree of crystalline order perpendicular

to the sample plane, even on this amorphous material, due to their van der Waals epitaxy growth mode. This study lays the groundwork for further investigation of the thermal properties of TI thin films free from contributions of uniaxial strain imposed by single crystal substrates. It also provides a proof-of-concept that such materials can be grown in a manner useful for particular device applications, e.g., as flexible transparent electrodes.

Chapter 5 demonstrated the formation of a ferromagnetic ground state in both Mn-doped Bi_2Te_3 bulk crystals and Bi_2Se_3 thin films grown by MBE. Bulk samples show an apparent solubility limit for the dopant of $x = 0.11$, above which the Mn is seen to precipitate out from the solid solution. In thin film samples, however, the dopant appears to form a parasitic phase within the host crystal at the limit of higher doping concentrations. Bulk samples show a ferromagnetic state below a measured T_C of $\sim$9.4 K, whilst the thin films samples seem to only be ferromagnetic below $\sim$1.5 K. Though for both bulk and thin film samples the observed T_C is too low for any device applications, it represents a significant step in establishing and understanding the physics required for such uses.

Chapter 6 presented an investigation of Cr-doped Bi_2Se_3 thin films grown by MBE and studied by a large range of structural and magnetic characterisation tools. It was found that Cr can be incorporated into the host Bi_2Se_3 without significant degradation of the crystalline properties and, crucially, without any increase in the c-axis lattice parameter, as may be expected for dopant clustering within the van der Waals gap. SQUID magnetometry studies showed a saturation magnetisation of 2.07 μ_B/Cr, significantly lower than the expected full magnetisation for Cr^{3+} with orbital quenching. The conflicting results of XRD indicating substitutional doping (i.e., Cr^{3+} is expected), and SQUID showing a reduced moment, were resolved by XMCD and EXAFS studies which conclusively demonstrated that the Cr does dope onto the Bi site, but with a reduced 2+ oxidation state. This reduced valency is due

to hybridisation between the Cr d and Se p orbitals, enhanced by relaxation of the bonds, decreasing the Cr-Se bond length. PNR studies demonstrated that there is no surface enhancement of the magnetic order and showed a uniform magnetisation profile throughout the sample bulk. This study makes a significant advance in the understanding of the nature of transition metal dopants in chalcogenide TIs and acts as a stepping stone towards the potential observation of the QAHE in doped Bi_2Se_3.

Overall the doping of TI materials with transition metal elements has shown promising results and may, in the future, be the platform on which new device applications are built or in which new physical phenomena are observed. This thesis has remained focussed on uniform doping with transition metals. However, other possible avenues of research may also lead to useful understanding, e.g., delta-doping of the material, magnetic heterostructures and doping with rare-earth elements. Parallel to this work there has also been a developing field and interest in other novel topological ordered materials, including topological superconductors [170], topological Weyl semi-metals [171], topological Kondo insulators [172, 173] and topological crystalline insulators [174]. These newly emerging fields of investigation into novel topological phases, as well as the magnetic doping of topological insulators, represent a promising new avenue of research in condensed matter that offer the possibility of new physics and unique electronic devices.

Appendix A

Calibration of Effusion Cells

This appendix will provide the relevant technical details regarding the operation of effusion cells present in the MBE system used for this thesis.

A.1 Cell Pressures vs. Temperatures

The partial pressure of each cell is calibrated after any major event (such as a machine opening or changes to the cells) or around once every 3 months otherwise. The cells are calibrated within a specific range of temperatures using an automated script that will record the change in pressure on the BFM for an open and closed cell shutter. This procedure will measure the partial pressure of the cell (directly related to incident flux) whilst removing any background from the rest gas of the chamber. Figure A.1 shows the calibrations for the 4 main cells used for TI growth. Note that all are standard effusion cells, with the exception of Se, which is in a hot-lip cracker cell. The fit parameters for the cells are summarised in Tab. A.1.

Though the 4 primary cells have remained essentially unchanged for the duration of this thesis, the dopant sources have regularly changed to accommodate new materials for different projects. Figure A.2 shows the calibrations for dopants presented

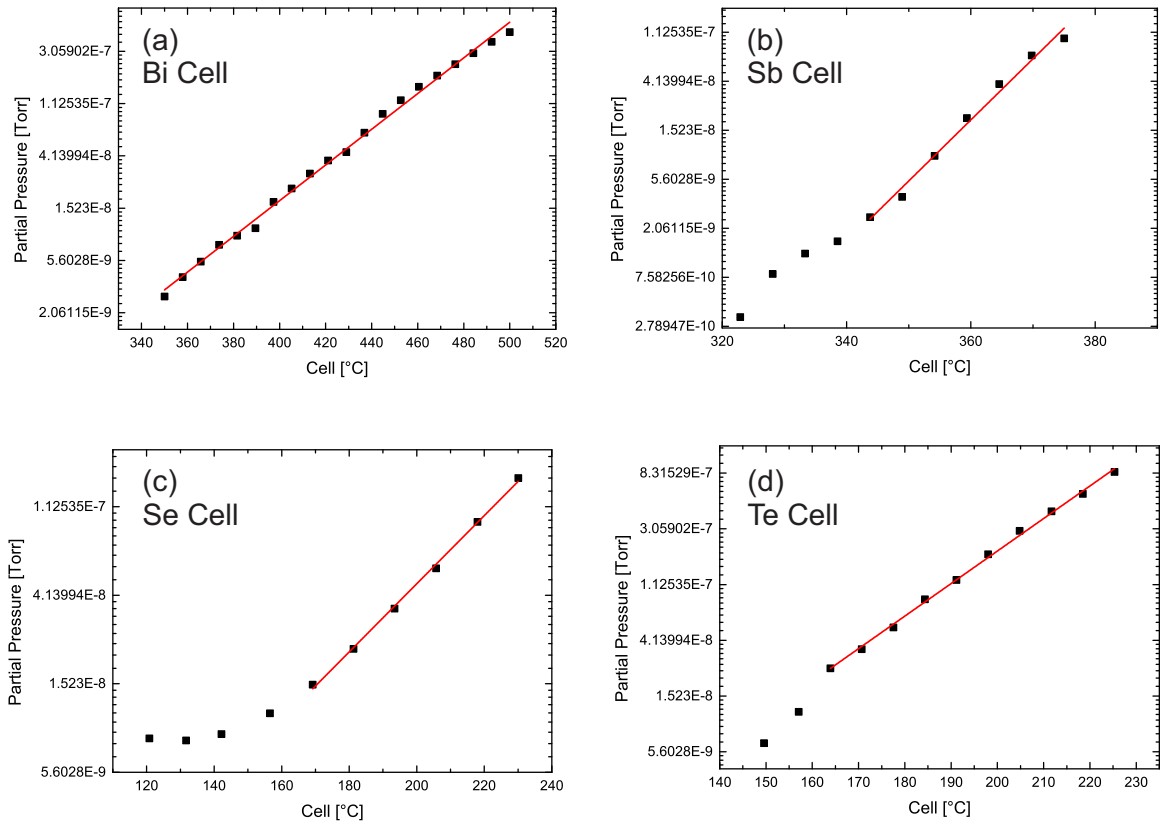

Figure A.1: Calibration curves of the main growth effusion cells. (a) Bi, (b) Sb, (c) Se and (d) Te. The temperature recorded for (c) is of the effusion cell body, the hot lip (see text) is 100°C higher.

Cell	Intercept (c)	Gradient (m)
Bi	-31.5 ± 0.2	0.0341 ± 0.0004
Sb	-62.7 ± 2	0.1247 ± 0.006
Se	-24.6 ± 0.2	0.0385 ± 0.0008
Te	-27.1 ± 0.2	0.0584 ± 0.0009

Table A.1: Calibration parameters for the 4 primary cells used in this system. Linear fits follow the form $\ln(P) = mT + c$, where T is the cell temperature and P the partial pressure.

in this thesis, though these calibrations were taken at different times. A summary of the fitted parameters is given in Tab. A.2.

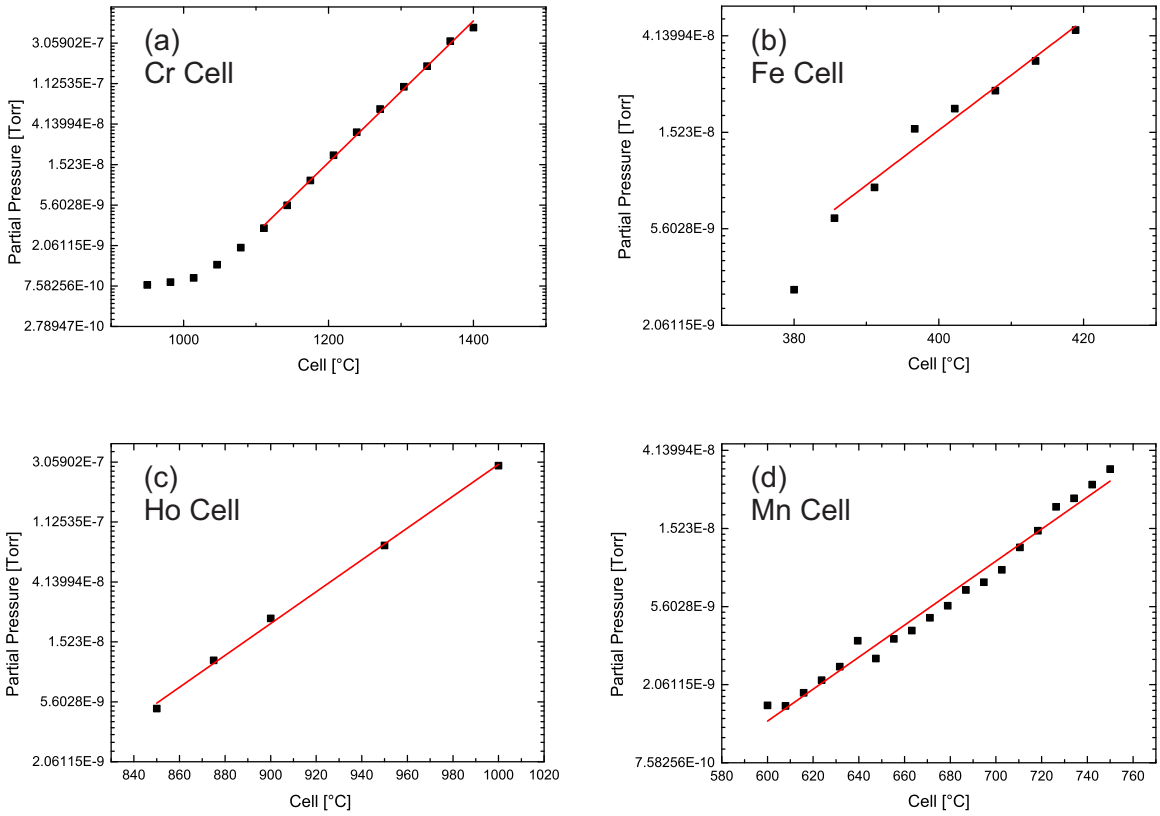

Figure A.2: Calibration curves of the dopant effusion cells. (a) Cr, (b) Fe, (c) Ho and (d) Mn.

Below is an example of the automatic calibration script written to control the cells and write the measured fluxes to a file. The minimum and maximum temperatures,

Cell	Intercept (c)	Gradient (m)
Cr	-38.9 ± 0.4	0.0175 ± 0.0003
Fe	-40.8 ± 2	0.0570 ± 0.004
Ho	-41.6 ± 0.6	0.0266 ± 0.0007
Mn	-32.8 ± 0.4	0.0205 ± 0.0007

Table A.2: Calibration parameters for some dopant sources used a various times in this system. Linear fits follow the form $\ln(P) = mT + c$, where T is the cell temperature and P the partial pressure.

as well as other necessary parameters are set in the code header.

```
main()
{
  float mintemp = 1000; // start temperature
  float maxtemp = 1200; // stop temperature
  float holdtime = 2; // in minutes
  float ramprateup = 0.1; // in degrees per second
  float rampratedown = 0.05; // in degrees per second
  int datapoints = 25; // number of measurement points
  float delta_lim = 4; // tolerance of flux stability condition

  // Set devices to ramp and read
  float acttemp = 0.0; // current target temperature in loop
  float temp_avg = 0.0;
  float temp_scaled = 0.0;
  float basepres_avg = 0.0;
  float basepres_scaled = 0.0;
  float fluxpres_avg = 0.0;
  float fluxpres_scaled = 0.0;
  float partialpres = 0.0;
  float delta = 0.0;
  float average = 0.0;
  int i;
  int j = 0;
  int k = 0;

  echoopen( echo_1.out, "/home/emeralt/calibrations/jan_2015/cell_2.txt", "
      w" );
  echo( echo_1.out, "Cell [C] \tBase Pressure [Torr] \tFlux Pressure [Torr]
       \tPartial Pressure [Torr]\n");

 reach(cell_2.t,mintemp,ramprateup/s);
 [10 m]; // wait to settle temperature

  for(i=0;i<datapoints;i=i+1)
```

```
{
  acttemp = mintemp + i * ((maxtemp - mintemp) / (datapoints - 1));
  echo("Ramping cell to %f", acttemp);
  reach(cell_2.t,acttemp,ramprateup/s);
  [holdtime m];
  temp_avg = 0.0; basepres_avg = 0.0; fluxpres_avg = 0.0; average = 0.0;
  // average

 // Wait for pressure stability with a minimum of 10 iterations.
 while(k==0)
  {
    temp_avg = temp_avg + cell_2.t;
    basepres_avg = basepres_avg + beam_flux.ig;
    if(j>4){
    average = basepres_avg/j;
    delta = (average - beam_flux.ig)/(1e9*average);
    delta = fabs(delta*1e11);
   }
    j = j+1;
    [2 s];
   if(j>300){
       k=1;
    }
    if(j > 10 && delta < delta_lim)
    {
       k = 1;
    }
 }
 basepres_avg = 0.0; temp_avg = 0.0;
 //Count pressure and temperature for averaging
 for(j=0;j<10;j=j+1)
 {
    temp_avg = temp_avg + cell_2.t;
    basepres_avg = basepres_avg + beam_flux.ig;
    [2 s];
 }
 //Open the shutter!
 open(shutter_2.s);
 k = 0;
 j=0;
 [1 m];
 //Do all of the above again
 // Wait for pressure stability with a minimum of 10 iterations.
 while(k==0)
 {
    fluxpres_avg = fluxpres_avg + beam_flux.ig;
    if(j>4){
```

```
      average = fluxpres_avg/j;
      delta = (average - beam_flux.ig)/(1e9*average);
      delta = fabs(delta*1e11);
     };
      j = j+1;
      [2 s];
      if(j>300){
          k=1;
      }
      if(j > 10 && delta < delta_lim)
      {
          k = 1;
      }
    }
    fluxpres_avg = 0.0;
    //Count pressure and temperature for averaging
    for(j=0;j<10;j=j+1)
    {
      fluxpres_avg = fluxpres_avg + beam_flux.ig;
      [2 s];
    }
    shut(shutter_2.s);
    // scale
    temp_scaled = temp_avg / 10.0;
    basepres_scaled = basepres_avg/10.0;
    fluxpres_scaled = fluxpres_avg/10.0;
    partialpres = fluxpres_scaled - basepres_scaled;

    // print to file
    echo( echo_1.out, "%f\t%e\t%e\t%e\n", temp_scaled, basepres_scaled,
        fluxpres_scaled, partialpres );
    echo("Writing data to file.");
    [1 s];
  }
  reach(cell_2.t,300,rampratedown/s);

  echo( echo_1.out, "\n" );
  echoclose( echo_1.out );

}
```

A.2 Tuning of Eurotherm Controllers

All cells used here are controlled using a Eurotherm process controller. This controller utilises a PID control loop to regulate applied current from the power supply in order

to maintain a constant temperature with very high (typically ±0.1°C) precision. PID loops must be tuned to match the specific cell design and material being evaporated. The optimum parameters also change considerably as a function of temperature, so control of high temperature sources will need very different values to that of lower temperature sources. All PID parameters are tuned independently for each source using the procedure below (Ziegler-Nichols method):

- Set the setpoint to desire operation temperature.
- Set both integral and derivative times to 0.
- If output is stable, reduce proportional band until it starts oscillating. If output is already oscillating, increase proportional band until it just stops.
- Make a note of the proportional band value (B) and period of oscillation (T).
- Set the P, I, D parameters according to Tab A.3 depending on type of control wanted.

All cells here make use of all 3 terms for control (P, I, D), though it is possible to use just proportional control or P+I control. Most controllers can also automatically tune, though this is hazardous as it will often induce large oscillations through power cycling that can be damaging to a cell, especially for molten sources.

Type of Control	**Proportional Band (P)**	**Integral Time (I)**	**Derivative Time (D)**
Proportional Only	2 x B	Off	Off
P + I	2.2 x B	0.8 x T	Off
P + I + D	1.7 x B	0.5 x T	0.12 x T

Table A.3: Calibration parameters depending on type of control wanted, following the Ziegler-Nichols method.

This procedure is derived from that described by Eurotherm UK Ltd.

Appendix B

Solvent Preparation of Substrates

Substrates in this thesis were prepared by solvent cleaning to remove any organic residue from manufacture or in transport by following the steps outlined below. Additionally for some samples a protective lacquer is applied by the manufacturer before cutting. For these samples the lacquer is first removed by boiling in acetone for 3 minutes before following these steps.

- Boil in trichloroethylene for 3 minutes
- Cold dip into isopropanol
- Boil in isopropanol for 3 minutes
- Cold dip into methanol
- Boil in methanol for 3 minutes
- Rinse with de-ionised water
- Blow until dry with dry nitrogen gas
- Bake under heat lamp for 30 minutes

Bibliography

[1] C. L. Kane and E. J. Mele. *Phys. Rev. Lett.* **95**, 146802 (2005).

[2] C. L. Kane and E. J. Mele. *Phys. Rev. Lett.* **95**, 226801 (2005).

[3] Y. Zhang, Y.-W. Tan, H. L. Stormer, and P. Kim. *Nature* **438**, 201 (2005).

[4] B. A. Bernevig and S.-C. Zhang. *Phys. Rev. Lett.* **96**, 106802 (2006).

[5] F. D. M. Haldane. *Phys. Rev. Lett.* **61**, 2015 (1988).

[6] S. Mishra, S. Satpathy, and O. Jepsen. *J. Phys.: Condens. Matter* **9**, 461 (1997).

[7] Y. Hor, A. Richardella, P. Roushan, Y. Xia, J. Checkelsky, A. Yazdani, M. Hasan, N. Ong, and R. Cava. *Phys. Rev. B* **79**, 195208 (2009).

[8] Y. Xia, D. Qian, D. Hsieh, L. Wray, A. Pal, H. Lin, A. Bansil, D. Grauer, Y. Hor, and R. Cava. *Nat. Phys.* **5**, 398 (2009).

[9] B. A. Bernevig, T. L. Hughes, and S.-C. Zhang. *Science* **314**, 1757 (2006).

[10] R. Roy. *Phys. Rev. B* **79**, 195322 (2009).

[11] R. B. Laughlin. *Phys. Rev. Lett.* **50**, 1395 (1983).

[12] C.-Z. Chang, J. Zhang, X. Feng, J. Shen, Z. Zhang, M. Guo, K. Li, Y. Ou, P. Wei, and L.-L. Wang. *Science* **340**, 167 (2013).

[13] X.-L. Qi, T. L. Hughes, and S.-C. Zhang. *Phys. Rev. B* **78**, 195424 (2008).

[14] X.-L. Qi, R. Li, J. Zang, and S.-C. Zhang. *Science* **323**, 1184 (2009).

[15] L. Fu and C. L. Kane. *Phys. Rev. Lett.* **102**, 216403 (2009).

[16] L. Fu and C. L. Kane. *Phys. Rev. Lett.* **100**, 096407 (2008).

[17] D. Pesin and A. H. MacDonald. *Nat. Mater.* **11**, 409 (2012).

[18] C. Nayak, S. H. Simon, A. Stern, M. Freedman, and S. D. Sarma. *Rev. Mod. Phys.* **80**, 1083 (2008).

[19] A. Y. Kitaev. *Ann. Phys.* **303**, 2 (2003).

[20] A. I. Figueroa, G. van der Laan, L. J. Collins-McIntyre, S.-L. Zhang, A. A. Baker, S. E. Harrison, P. Schönherr, G. Cibin, and T. Hesjedal. *Phys. Rev. B* **90**, 134402 (2014).

[21] L. J. Collins-McIntyre, S. E. Harrison, P. Schönherr, N.-J. Steinke, C. J. Kinane, T. R. Charlton, D. Alba-Veneroa, A. Pushp, A. J. Kellock, S. S. P. Parkin, J. S. Harris, S. Langridge, G. van der Laan, and T. Hesjedal. *Europhys. Lett.* **107**, 57009 (2014).

[22] M. D. Watson, L. J. Collins-McIntyre, L. R. Shelford, A. I. Coldea, D. Prabhakaran, S. C. Speller, T. Mousavi, C. R. M. Grovenor, Z. Salman, S. R. Giblin, G. van der Laan, and T. Hesjedal. *New J. Phys.* **15**, 103016 (2013).

[23] L. J. Collins-McIntyre, M. D. Watson, A. A. Baker, S. L. Zhang, A. I. Coldea, S. E. Harrison, A. Pushp, A. J. Kellock, S. S. P. Parkin, G. van der Laan, and T. Hesjedal. *AIP Adv.* **4**, 127136 (2014).

[24] S. Li, S. E. Harrison, Y. Huo, A. Pushp, H. T. Yuan, B. Zhou, A. J. Kellock, S. S. P. Parkin, Y.-L. Chen, T. Hesjedal, and J. S. Harris. *Appl. Phys. Lett.* **102**, 242412 (2013).

[25] S. E. Harrison, L. J. Collins-McIntyre, S. Li, A. A. Baker, L. R. Shelford, Y. Huo, A. Pushp, S. S. P. Parkin, J. S. Harris, E. Arenholz, G. van der Laan, and T. Hesjedal. *J. Appl. Phys.* **115**, 023904 (2014).

[26] J. E. Moore. *Nature* **464**, 194 (2010).

[27] K. v. Klitzing. *Physica B+C* **126**, 242 (1984).

[28] J. E. Hirsch. *Phys. Rev. Lett.* **83**, 1834 (1999).

[29] N. Nagaosa, J. Sinova, S. Onoda, A. H. MacDonald, and N. P. Ong. *Rev. Mod. Phys.* **82**, 1539 (2010).

[30] X.-L. Qi and S.-C. Zhang. *Physics Today* **63**, 33 (2010).

[31] M. König, S. Wiedmann, C. Brüne, A. Roth, H. Buhmann, L. W. Molenkamp, X.-L. Qi, and S.-C. Zhang. *Science* **318**, 766 (2007).

[32] H. A. Kramers. *Proc. Amsterdam Acad.* **33**, 959 (1930).

[33] E. Beaurepaire, H. Bulou, L. Joly, and F. Scheurer, editors. *Magnetism and Synchrotron Radiation: Towards the Fourth Generation Light Sources*, volume 151 of *Springer Proceedings in Physics* (Springer, Heidelberg, 2012).

[34] H. Zhang, C.-X. Liu, X.-L. Qi, X. Dai, Z. Fang, and S.-C. Zhang. *Nat. Phys.* **5**, 438 (2009).

[35] Y. Zhang, K. He, C.-Z. Chang, C.-L. Song, L.-L. Wang, X. Chen, J.-F. Jia, Z. Fang, X. Dai, W.-Y. Shan, S.-Q. Shen, Q. Niu, X.-L. Qi, S.-C. Zhang, X.-C. Ma, and Q.-K. Xue. *Nat. Phys.* **6**, 584 (2010).

[36] Y. L. Chen, J. G. Analytis, J.-H. Chu, Z. K. Liu, S.-K. Mo, X. L. Qi, H. J. Zhang, D. H. Lu, X. Dai, Z. Fang, S. C. Zhang, I. R. Fisher, Z. Hussain, and Z.-X. Shen. *Science* **325**, 178 (2009).

[37] Y. Chen, J.-H. Chu, J. Analytis, Z. Liu, K. Igarashi, H.-H. Kuo, X. Qi, S.-K. Mo, R. Moore, and D. Lu. *Science* **329**, 659 (2010).

[38] X.-L. Qi, R. Li, J. Zang, and S.-C. Zhang. *Science* **323**, 1184 (2009).

[39] R. Yu, W. Zhang, H.-J. Zhang, S.-C. Zhang, X. Dai, and Z. Fang. *Science* **329**, 61 (2010).

[40] J. Arthur Jr. *J. Appl. Phys.* **39**, 4032 (1968).

[41] I. V. Markov. *Crystal Growth for Beginners: Fundamentals of Nucleation, Crystal Growth, and Epitaxy* (World Scientific, Singapore, 1995).

[42] M. A. Herman and H. Sitter. *Molecular Beam Epitaxy: Fundamentals and Current Status* (Springer-Verlag, Berlin, 1989).

[43] R. F. C. Farrow. *Molecular Beam Epitaxy: Applications to Key Materials* (Noyes Publications, New Jersey, 1995).

[44] P. Walker and W. H. Tarn. *CRC Handbook of Metal Etchants* (CRC Press, 1990).

[45] A. Ichimiya and P. I. Cohen. *Reflection high-energy electron diffraction* (Cambridge University Press, 2004).

[46] D. S. Sivia. *Elementary scattering theory: For X-ray and neutron users* (Oxford University Press, 2011).

[47] J. Neave, B. Joyce, P. Dobson, and N. Norton. *Appl. Phys. A* **31**, 1 (1983).

[48] M. Bjorck and G. Andersson. *J. of Appl. Crystallogr.* **40**, 1174 (2007).

[49] M. Yasaka. *The Rigaku Journal* **26**, 1 (2010).

[50] D. Nečas and P. Klapetek. *Cent. Eur. J. Phys.* **10**, 181 (2012).

[51] W.-K. Chu. *Backscattering spectrometry* (Elsevier, 2012).

[52] R. Jaklevic, J. Lambe, A. Silver, and J. Mercereau. *Phys. Rev. Lett.* **12**, 159 (1964).

[53] S. Blundell. *Magnetism in Condensed Matter.* Oxford Master Series in Condensed Matter Physics (Oxford University Press, 2001).

[54] G. van der Laan. *J. Phys. Conf. Ser.* **430**, 012127 (2013).

[55] J. Stöhr. *J. Magn. Magn. Mater.* **200**, 470 (1999).

[56] T. Funk, A. Deb, S. J. George, H. Wang, and S. P. Cramer. *Coordin. Chem. Rev.* **249**, 3 (2005).

[57] G. van der Laan and A. I. Figueroa. *Coordin. Chem. Rev.* **277–278**, 95 (2014).

[58] B. Thole, P. Carra, F. Sette, and G. van der Laan. *Phys. Rev. Lett.* **68**, 1943 (1992).

[59] J.-J. Zhu, D.-X. Yao, S.-C. Zhang, and K. Chang. *Phys. Rev. Lett.* **106**, 097201 (2011).

[60] Q. Liu, C.-X. Liu, C. Xu, X.-L. Qi, and S.-C. Zhang. *Phys. Rev. Lett.* **102**, 156603 (2009).

[61] Z. Chen, T. A. Garcia, J. De Jesus, L. Zhao, H. Deng, J. Secor, M. Begliarbekov, L. Krusin-Elbaum, and M. C. Tamargo. *J. Electron. Mater.* **43**, 909 (2014).

[62] M. Eddrief, P. Atkinson, V. Etgens, and B. Jusserand. *Nanotechnology* **25**, 245701 (2014).

[63] Y. Zhao, C.-Z. Chang, Y. Jiang, A. DaSilva, Y. Sun, H. Wang, Y. Xing, Y. Wang, K. He, X. Ma, Q.-K. Xue, and J. Wang. *Sci. Rep.* **3**, 3060 (2013).

[64] S. E. Harrison, S. Li, Y. Huo, B. Zhou, Y. L. Chen, and J. S. Harris. *Appl. Phys. Lett.* **102**, 171906 (2013).

[65] X. Liu, D. J. Smith, H. Cao, Y. P. Chen, J. Fan, Y.-H. Zhang, R. E. Pimpinella, M. Dobrowolska, and J. K. Furdyna. *J. Vac. Sci. Technol. B* **30**, 02B103 (2012).

[66] L. He, F. Xiu, Y. Wang, A. V. Fedorov, G. Huang, X. Kou, M. Lang, W. P. Beyermann, J. Zou, and K. L. Wang. *J. Appl. Phys.* **109**, 103702 (2011).

[67] J. Krumrain, G. Mussler, S. Borisova, T. Stoica, L. Plucinski, C. Schneider, and D. Grützmacher. *J. Cryst. Growth* **324**, 115 (2011).

[68] X. Liu, D. J. Smith, J. Fan, Y.-H. Zhang, H. Cao, Y. P. Chen, J. Leiner, B. J. Kirby, M. Dobrowolska, and J. K. Furdyna. *Appl. Phys. Lett.* **99**, 171903 (2011).

[69] A. Koma. *Thin Solid Films* **216**, 72 (1992).

[70] B. Gardes, G. Brun, and J. C. Tedenac. *Eur. J. Solid Stat. Inorg. Eur. J. Solid Stat. Inorg. Chem.* **26**, 221 (1989).

[71] Y. Liu, M. Weinert, and L. Li. *Phys. Rev. Lett.* **108**, 115501 (2012).

[72] M. Ferhat, J. C. Tedenac, and J. Nagao. *J. Cryst. Growth* **218**, 250 (2000).

[73] H.-J. Kim, H. W. You, W. C. Choi, C. Park, Y.-H. Kim, S. I. Kim, and J.-S. Kim. *AIP Conf. Proc.* **1449**, 401 (2012).

[74] Y. S. Touloukian, editor. *Thermophysical properties of matter* (IFI/Plenum, New York, 1970).

[75] D. Teweldebrhan, V. Goyal, M. Rahman, and A. A. Balandin. *Appl. Phys. Lett.* **96**, 053107 (2010).

[76] S. Jerng, K. Joo, Y. Kim, S. Yoon, J. Lee, M. Kim, J. Kim, E. Yoon, S. Chun, and Y. Kim. *Nanoscale* **5**, 10618 (2013).

[77] N. Bansal, N. Koirala, M. Brahlek, M. Han, Y. Zhu, Y. Cao, J. Waugh, D. Dessau, and S. Oh. *Appl. Phys. Lett.* **104**, 241606 (2014).

[78] L. J. Collins-McIntyre, W. Wang, B. Zhou, S. C. Speller, Y. L. Chen, and T. Hesjedal. *Phys. Stat. Sol. (b)* **Accepted** (2014).

[79] W. M. Haynes, editor. *CRC Handbook of Chemistry and Physics (93rd Edition)* (CRC Press, 2012).

[80] MTI Corporation, Fused Silica Properties Nov. (2014).

[81] S. E. Harrison, B. Zhou, Y. Huo, A. Pushp, A. J. Kellock, S. S. P. Parkin, J. S. Harris, Y. Chen, and T. Hesjedal. *Appl. Phys. Lett.* **105**, 121608 (2014).

[82] S. Schreyeck, N. Tarakina, G. Karczewski, C. Schumacher, T. Borzenko, C. Brüne, H. Buhmann, C. Gould, K. Brunner, and L. Molenkamp. *Appl. Phys. Lett.* **102**, 041914 (2013).

[83] CrysTec GmbH, Ge Datasheet Jan. (2015).

[84] L. Chan, E. Altman, and Y. Liang. *J. Vac. Sci. Technol.* **19**, 976 (2001).

[85] J. Choi, S. Choi, J. Choi, Y. Park, H. Park, H. Lee, B. Woo, and S. Cho. *Phys. Stat. Sol. (b)* **241**, 1541 (2004).

[86] J. W. G. Bos, M. Lee, E. Morosan, H. W. Zandbergen, W. L. Lee, N. P. Ong, and R. J. Cava. *Phys. Rev. B* **74**, 184429 (2006).

[87] Y. S. Hor, P. Roushan, H. Beidenkopf, J. Seo, D. Qu, J. G. Checkelsky, L. A. Wray, D. Hsieh, Y. Xia, S.-Y. Xu, D. Qian, M. Z. Hasan, N. P. Ong, A. Yazdani, and R. J. Cava. *Phys. Rev. B* **81**, 195203 (2010).

[88] H. J. von Bardeleben, J. L. Cantin, D. M. Zhang, A. Richardella, D. W. Rench, N. Samarth, and J. A. Borchers. *Phys. Rev. B* **88**, 075149 (2013).

[89] D. Zhang, A. Richardella, D. W. Rench, S.-Y. Xu, A. Kandala, T. C. Flanagan, H. Beidenkopf, A. L. Yeats, B. B. Buckley, P. V. Klimov, D. D. Awschalom, A. Yazdani, P. Schiffer, M. Z. Hasan, and N. Samarth. *Phys. Rev. B* **86**, 205127 (2012).

[90] J. S. Lee, A. Richardella, D. W. Rench, R. D. Fraleigh, T. C. Flanagan, J. A. Borchers, J. Tao, and N. Samarth. *Phys. Rev. B* **89**, 174425 (2014).

[91] B. Jariwala and D. V. Shah. *J. Cryst. Growth* **318**, 1179 (2011).

[92] H. J. M. Swagten, C. E. P. Gerrits, A. Twardowski, and W. J. M. de Jonge. *Phys. Rev. B* **41**, 7330 (1990).

[93] C. Niu, Y. Dai, M. Guo, W. Wei, Y. Ma, and B. Huang. *Appl. Phys. Lett.* **98**, 252502 (2011).

[94] J. Henk, A. Ernst, S. V. Eremeev, E. V. Chulkov, I. V. Maznichenko, and I. Mertig. *Phys. Rev. Lett.* **108**, 206801 (2012).

[95] A. Arrott. *Phys. Rev.* **108**, 1394 (1957).

[96] T. Jungwirth, K. Wang, J. Masek, K. Edmonds, J. Konig, J. Sinova, M. Polini, N. Goncharuk, A. MacDonald, M. Sawicki, A. Rushforth, R. Campion, L. Zhao, C. Foxon, and B. Gallagher. *Phys. Rev. B* **72**, 165204 (2005).

[97] C. Gould, K. Pappert, G. Schmidt, and L. W. Molenkamp. *Adv. Mater.* **19**, 323 (2007).

[98] S. J. Blundell. *Contemp. Phys.* **40**, 175 (1999).

[99] Z. Salman, E. Pomjakushina, V. Pomjakushin, A. Kanigel, K. Chashka, K. Conder, E. Morenzoni, T. Prokscha, K. Sedlak, and A. Suter. *cond-mat arXiv:1203.4850* (2012).

[100] M. Ye, S. V. Eremeev, K. Kuroda, E. E. Krasovskii, E. V. Chulkov, Y. Takeda, Y. Saitoh, K. Okamoto, S. Y. Zhu, K. Miyamoto, M. Arita, M. Nakatake, T. Okuda, Y. Ueda, K. Shimada, H. Namatame, M. Taniguchi, and A. Kimura. *Phys. Rev. B* **85**, 205317 (2012).

[101] J. Honolka, A. A. Khajetoorians, V. Sessi, T. O. Wehling, S. Stepanow, J.-L. Mi, B. B. Iversen, T. Schlenk, J. Wiebe, N. Brookes, A. I. Lichtenstein, P. Hofmann, K. Kern, and R. Wiesendanger. *Phys. Rev. Lett.* **108**, 256811 (2012).

[102] I. Vobornik, U. Manju, J. Fujii, F. Borgatti, P. Torelli, D. Krizmancic, Y. S. Hor, R. J. Cava, and G. Panaccione. *Nano Lett.* **11**, 4079 (2011).

[103] L. R. Shelford, T. Hesjedal, L. Collins-McIntyre, S. S. Dhesi, F. Maccherozzi, and G. van der Laan. *Phys. Rev. B* **86**, 081304 (2012).

[104] S.-Y. Xu, M. Neupane, C. Liu, D. Zhang, A. Richardella, L. A. Wray, N. Alidoust, M. Leandersson, T. Balasubramanian, J. Sanchez-Barriga, O. Rader, G. Landolt, B. Slomski, J. H. Dil, J. Osterwalder, T.-R. Chang, H.-T. Jeng, H. Lin, A. Bansil, N. Samarth, and M. Z. Hasan. *Nat. Phys.* **8**, 616 (2012).

[105] K. Edmonds, N. Farley, R. Campion, C. Foxon, B. Gallagher, T. Johal, G. van der Laan, M. MacKenzie, J. Chapman, and E. Arenholz. *Appl. Phys. Lett.* **84**, 4065 (2004).

[106] B. T. Thole and G. van der Laan. *Phys. Rev. B* **38**, 3158 (1988).

[107] H. Durr, G. vanderLaan, D. Spanke, F. Hillebrecht, and N. Brookes. *Phys. Rev. B* **56**, 8156 (1997).

[108] G. van der Laan and B. T. Thole. *Phys. Rev. B* **43**, 13401 (1991).

[109] K. W. Edmonds, N. R. S. Farley, T. K. Johal, G. van der Laan, R. P. Campion, B. L. Gallagher, and C. T. Foxon. *Phys. Rev. B* **71**, 064418 (2005).

[110] G. van der Laan. *Lect. Notes Phys.* **697**, 143 (2006).

[111] R. D. Cowan. *J. Opt. Soc. Am.* **58**, 808 (1968).

[112] R. D. Cowan. *The Theory of Atomic Structure* (University of California Press, Berkeley, 1981).

[113] G. van der Laan and B. Thole. *J. Phys.: Condens. Matter* **4**, 4181 (1992).

[114] K. P. Belov. *Magnetic Transitions* (Consultants Bureau Enterprises, New York, 1961).

[115] R. Forrer. *J. Phys.* **1**, 49 (1930).

[116] D. I. Volkov and V. I. Chechernikov. *Izv. Akad. Nauk SSSR (Ser. Fiz.)* **21**, 1111 (1957).

[117] M. Lasia and L. Brey. *Phys. Rev. B* **86**, 045317 (2012).

[118] J. Dyck, v. Drašar, P. Lošták, and C. Uher. *Phys. Rev. B* **71**, 115214 (2005).

[119] M. Z. Hasan and C. L. Kane. *Rev. Mod. Phys.* **81**, 195203 (2010).

[120] H.-Z. Lu, J. Shi, and S.-Q. Shen. *Phys. Rev. Lett.* **107**, 076801 (2011).

[121] Z. Liu, X. Wei, J. Wang, H. Pan, F. Ji, F. Xi, J. Zhang, T. Hu, S. Zhang, Z. Jiang, W. Wen, Y. Huang, M. Ye, Z. Yang, and S. Qiao. *Phys. Rev. B* **90**, 094107 (2014).

[122] P. Larson and W. R. L. Lambrecht. *Phys. Rev. B* **78**, 195207 (2008).

[123] Y. H. Choi, N. H. Jo, K. J. Lee, H. W. Lee, Y. H. Jo, J. Kajino, T. Takabatake, K.-T. Ko, J.-H. Park, and M. H. Jung. *Appl. Phys. Lett.* **101**, 152103 (2012).

[124] P. Carra, B. T. Thole, M. Altarelli, and X. Wang. *Phys. Rev. Lett.* **70**, 694 (1993).

[125] G. van der Laan and B. T. Thole. *Phys. Rev. B* **43**, 13401 (1991).

[126] I. Vobornik, G. Panaccione, J. Fujii, Z.-H. Zhu, F. Offi, B. R. Salles, F. Borgatti, P. Torelli, J. P. Rueff, D. Ceolin, A. Artioli, M. Unnikrishnan, G. Levy, M. Marangolo, M. Eddrief, D. Krizmancic, H. Ji, A. Damascelli, G. van der Laan, R. G. Egdell, and R. J. Cava. *J. Phys. Chem. C* **118**, 12333 (2014).

[127] G. Springholz, J. Sanchez Barriga, H. Steiner, R. Kirchschlager, G. Bauer, A. Varykhalov, O. Rader, E. Schierle, E. Weschke, O. Caha, and V. Holy. In '20th International Conference on Electronic Properties of Two-Dimensional Systems', (2014).

[128] A. Giani, A. Boulouz, F. Pascal-Delannoy, A. Foucaran, E. Charles, and A. Boyer. *Mater. Sci. Eng. B* **64**, 19 (1999).

[129] Y.-J. Chien. *Transition Metal-Doped Sb_2Te_3 and Bi_2Te_3 Diluted Magnetic Semiconductors*. Ph.D. thesis, The University of Michigan (2007).

[130] H. A and C. Elsässer. *Phys. Rev. B* **84**, 144117 (2011).

[131] L. Xue, P. Zhou, C. X. Zhang, C. Y. He, G. L. Hao, L. Z. Sun, and J. X. Zhong. *AIP Adv.* **3**, 052105 (2013).

[132] M. Zeng, W. Huang, and G. Liang. *Nanoscale* **5**, 200 (2013).

[133] J.-M. Zhang, W. Ming, Z. Huang, G.-B. Liu, X. Kou, Y. Fan, K. L. Wang, and Y. Yao. *Phys. Rev. B* **88**, 235131 (2013).

[134] J.-M. Zhang, W. Zhu, Y. Zhang, D. Xiao, and Y. Yao. *Phys. Rev. Lett.* **109**, 266405 (2012).

[135] M. C. Shaughnessy, N. C. Bartelt, J. A. Zimmerman, and J. D. Sugar. *J. Appl. Phys.* **115**, 063705 (2014).

[136] J. Horák, P. Lošťák, C. Drašar, J. S. Dyck, Z. Zhouc, and C. Uher. *J. Solid State Chem.* **178**, 2907 (2005).

[137] M. G. Vergniory, M. M. Otrokov, D. Thonig, M. Hoffmann, I. V. Maznichenko, M. Geilhufe, X. Zubizarreta, S. Ostanin, A. Marmodoro, J. Henk, W. Hergert, I. Mertig, E. V. Chulkov, and A. Ernst. *Phys. Rev. B* **89**, 165202 (2014).

[138] J. Choi, H.-W. Lee, B.-S. Kim, H. Park, S. Choi, S. C. Hong, and S. Cho. *J. Magn. Magn. Mater.* **304**, 164 (2006).

[139] P. Janíček, v. Drašar, P. Lošťák, J. Vejpravová, and V. Sechovský. *Physica B* **403**, 3553 (2008).

[140] G. Rosenberg and M. Franz. *Phys. Rev. B* **85**, 195119 (2012).

[141] H. C. Jeon, Y. S. Jeong, T. W. Kang, T. W. Kim, K. J. Chung, K. J. Chung, W. Jhe, and S. A. Song. *Adv. Mater.* **14**, 1725 (2002).

[142] M. A. Korzhuev and T. E. Svechnikov. *Sov. Phys. Semicond.* **25**, 1288 (1991).

[143] R. O. Carlson. *J. Phys. Chem. Solids* **13**, 65 (1960).

[144] L. Wu, M. Brahlek, R. Valdés Aguilar, A. V. Stier, C. M. Morris, Y. Lubashevsky, L. S. Bilbro, N. Bansal, S. Oh, and N. P. Armitage. *Nat. Phys.* **9**, 410 (2013).

[145] J. Henk, M. Flieger, I. V. Maznichenko, I. Mertig, A. Ernst, S. V. Eremeev, and E. V. Chulkov. *Phys. Rev. Lett.* **109**, 076801 (2012).

[146] A. I. Figueroa, G. van der Laan, L. J. Collins-McIntyre, G. Cibin, A. J. Dent, and T. Hesjedal. *J. Phys. Chem. C* **Submitted** (2014).

[147] J. Wang, B. Lian, H. Zhang, Y. Xu, and S.-C. Zhang. *Phys. Rev. Lett.* **111**, 136801 (2013).

[148] A. L. Wray, S. Y. Xu, Y. Xia, D. Hsieh, A. V. Fedorov, Y. S. Hor, R. J. Cava, A. Bansil, H. Lin, and M. Z. Hasan. *Nat. Phys.* **7**, 32 (2011).

[149] V. Kulbachinskii, A. Kaminskii, K. Kindo, Y. Narumi, K. Suga, P. Lostak, and P. Svanda. *Physica B* **311**, 292 (2002).

[150] Y. Choi, N. Jo, K. Lee, J. Yoon, C. You, and M. Jung. *J. Appl. Phys.* **109**, 07E312 (2011).

[151] P. Haazen, J.-B. Laloë, T. Nummy, H. Swagten, P. Jarillo-Herrero, D. Heiman, and J. Moodera. *Appl. Phys. Lett.* **100**, 082404 (2012).

[152] X. Kou, M. Lang, Y. Fan, Y. Jiang, T. Nie, J. Zhang, W. Jiang, Y. Wang, Y. Yao, L. He, and K. L. Wang. *ACS Nano* **7**, 9205 (2013).

[153] L. Bao, W. Wang, N. Meyer, Y. Liu, C. Zhang, K. Wang, P. Ai, and F. Xiu. *Sci. Rep.* **3**, 2391 (2013).

[154] B. Gardes, G. Brun, and J. C. Tedenac. *Eur. J. Solid Stat. Inorg. Chem.* **26**, 221 (1989).

[155] S. J. Blundell and J. A. C. Bland. *Phys. Rev. B* **46**, 3391 (1992).

[156] M. Björck and G. Andersson. *J. Appl. Cryst.* **40**, 1174 (2007).

[157] J. G. Checkelsky, J. Ye, Y. Onose, Y. Iwasa, and Y. Tokura. *Nat. Phys.* **8**, 729 (2012).

[158] Y. H. Choi, N. H. Jo, K. J. Lee, J. B. Yoon, C. Y. Yo, and M. H. Jung. *Phys. Rev. B* **89**, 075103 (2014).

[159] C.-Z. Chang, P. Tang, Y.-L. Wang, X. Feng, K. Li, Z. Zhang, Y. Wang, L.-L. Wang, X. Chen, C. Liu, W. Duan, K. He, X.-C. Ma, and Q.-K. Xue. *Appl. Phys. Lett.* **112**, 056801 (2014).

[160] P. Larson and W. R. L. Lambrecht. *Phys. Rev. B* **78** (2008).

[161] X. F. Kou, W. J. Jiang, M. R. Lang, F. X. Xiu, L. He, Y. Wang, Y. Wang, X. X. Yu, A. V. Fedorov, P. Zhang, and K. L. Wang. *J. Appl. Phys.* **112**, 063912 (2012).

[162] R. D. Shannon. *Acta Crystallogr. A* **32**, 751 (1976).

[163] G. van der Laan and I. W. Kirkman. *J. Phys.: Condens. Matter* **4**, 4189 (1992).

[164] B. T. Thole and G. van der Laan. *Phys. Rev. B* **38**, 3158 (1988).

[165] M. Mizumaki, A. Agui, Y. Saitoh, M. Nakazawa, and T. Matsushita. *Surf. Rev. Lett.* **9**, 849 (2002).

[166] N. D. Telling, V. S. Coker, R. S. Cutting, G. van der Laan, C. I. Pearce, R. A. D. Pattrick, E. Arenholz, and J. R. Lloyd. *Appl. Phys. Lett.* **95**, 163701 (2009).

[167] B. Ravel and M. Newville. *J. Synchrotron Radiat.* **12**, 537 (2005).

[168] B. Ravel. *J. Synchrotron Radiat.* **8**, 314 (2001).

[169] J.-M. Zhang, W. Zhu, Y. Zhang, D. Xiao, and Y. Yao. *Phys. Rev. Lett.* **109**, 266405 (2012).

[170] X.-L. Qi, T. L. Hughes, S. Raghu, and S.-C. Zhang. *Phys. Rev. Lett.* **102**, 187001 (2009).

[171] A. Burkov and L. Balents. *Phys. Rev. Lett.* **107**, 127205 (2011).

[172] M. Dzero, K. Sun, V. Galitski, and P. Coleman. *Phys. Rev. Lett.* **104**, 106408 (2010).

[173] M. Neupane, N. Alidoust, S.-Y. Xu, T. Kondo, Y. Ishida, D. J. Kim, C. Liu, I. Belopolski, Y. J. Jo, T.-R. Chang, H.-T. Jeng, T. Durakiewicz, L. Balicas, H. Lin, A. Bansil, S. Shin, Z. Fisk, and M. Z. Hasan. *Nat. Comms.* **4**, 2991 (2013).

[174] L. Fu. *Phys. Rev. Lett.* **106**, 106802 (2011).